

DISSERTATION

Numerical Modeling of Quantum Cascade Lasers

ausgeführt zum Zwecke der Erlangung des akademischen Grades
eines Doktors der technischen Wissenschaften

eingereicht an der Technischen Universität Wien
Fakultät für Elektrotechnik und Informationstechnik
von

GORAN MILOVANOVIĆ

Schallergasse 20/10
1120 Wien, Österreich

Matr. Nr. 9925120
geboren am 19. August 1981 in Tulln an der Donau

Wien, im März 2011

Kurzfassung

Ein elektrisch gepumpter Quantenkaskadenlaser (QCL) ist ein unipolarer Halbleiterlaser dessen Funktionsweise auf Intersubbandübergängen und Tunneleffekt beruht. Photonen werden aufgrund von elektronischen Intersubbandübergängen innerhalb des Leitungsbandes emittiert. Die dazugehörige Wellenlänge ist abhängig von der Lage der Energieniveaus und diese von den Breiten der Quantentöpfe und Barrieren in der Heterostruktur. QCLs haben viele Anwendungsmöglichkeiten im mittleren und fernen Infrarot Bereich.

Eine detaillierte Einführung in die Modellierung des Transports in QCLs wird präsentiert. Für die Modellierung des Ladungstransports in QCLs kann ein semi-klassischer Ansatz verwendet werden. Basierend auf der Monte Carlo Methode wurde ein Simulator entwickelt, der eine semi-klassische Transportgleichung löst. Die Zustände der Elektronen werden mittels eines selbstkonsistenten Schrödinger-Poisson Solvers ermittelt. Es werden folgende Streuprozesse berücksichtigt: Elektronstreuung durch polar-optische und akustische Phononen, optische Deformationspotentialstreuung, Zwischentalstreuung, Grenzflächenstreuung, und Legierungsstreuung.

Im Allgemeinen kann der Simulator für die Untersuchung des Ladungstransports und grundsätzlicher Eigenschaften von QCLs verwendet werden. Im Speziellen wird der Einfluss der Γ -X Zwischentalstreuung auf den Ladungstransport eines GaAs/AlGaAs QCL untersucht. Es wird gezeigt, dass die Stromdichte signifikant ansteigt, wenn ein grösserer Überlapp zwischen dem oberen X-Zustand und dem unteren Γ -Zustand benachbarter Stufen erzielt wird. Dies wird mittels einer Modifikation des Al Gehalts und der Breite der Sammelbarriere erreicht. In diesem Zusammenhang wird der dominante Einfluss des Γ -X Zwischentalstreumechanismus identifiziert und die Wichtigkeit des Zwischental-Ladungstransports für Design Überlegungen von QCLs demonstriert. Darüber hinaus wird ein kürzlich entwickelter InGaAs/GaAsSb QCL mithilfe des Simulators untersucht. Ein Vergleich zwischen den ermittelten Simulationsresultaten und Messergebnissen wird präsentiert. Die errechnete Strom-Spannungs Kennlinie ist in guter Übereinstimmung mit den Messwerten und es ist ein dominanter Einfluss seitens der polar-optischen Streuung, sowie der Legierungs- und Grenzflächenstreuung zu beobachten.

Abstract

Quantum Cascade Lasers (QCLs) are electrically pumped unipolar semiconductor lasers based on intersubband transitions and tunneling. Photons are emitted via electronic intersubband transitions that take place within the conduction band, where the wavelength is determined by the separation of the energy levels. These levels are designed by proper engineering of the well and barrier widths in multiple quantum well heterostructures. QCLs have potential for a wide range of applications in the mid- and far-infrared region and these devices are still improving.

A detailed introduction into the theoretical framework relevant to transport modeling in QCLs is presented, including the quantum ballistic transport and the density matrix formulation. In order to model charge transport in QCLs a semi-classical approach can be employed. A simulator has been developed which solves a semi-classical transport equation by means of a Monte Carlo method, while the electron states are evaluated using a selfconsistent Schrödinger-Poisson solver. The following scattering mechanisms are included: electron scattering by polar optical and acoustic phonons, optical deformation potential interaction, inter-valley phonons, interface roughness, and alloy scattering.

The simulator has been applied to investigate charge transport and the performance of QCLs in general. Special focus is laid on the role of Γ -X intervalley scattering as a mechanism for influencing charge transfer in a GaAs/AlGaAs QCL. It is shown that the modification of the Al content and the width of the collector barrier in order to increase the overlap between the upper X-state and the lower Γ -state belonging to two adjacent stages results in a significant increase in current density. In this context, the Γ -X intervalley scattering mechanism is shown to have a dominant impact, and the results demonstrate the importance of intervalley charge transport for QCL design considerations. Furthermore, the simulator has been used to investigate a recently developed InGaAs/GaAsSb QCL. A comparison of simulation results with measurements is presented. The calculated and measured voltage-current characteristics are in good agreement. We have been able to observe the dominant impact of polar optical phonon scattering and also significant effects due to alloy scattering and interface roughness scattering.

Acknowledgment

At first I want to thank my advisor *Prof. Hans Kosina* for giving me the opportunity to join his research group and work in the vast and amazing field of microelectronics. He took care for excellent working conditions, a calm working environment and last but not least encouraged the attendance of several scientific conferences.

Furthermore, I am indebted to *Prof. Siegfried Selberherr* and *Prof. Erasmus Langer*, the head of the Institute, for the reposeful working climate, which serves as a basis for worldclass scientific work.

During my stay at the Institute I had the pleasure to collaborate on different levels with other colleagues I have a high regard for: *Oskar Baumgartner, Zlatan Stanojevic, Thomas Windbacher, Martin Vasicek, Johann Cervenka, Paul-Juergen Wagner, Otmar Ertl, Philipp Hehenberger, Gregor Meller, Karl Rupp, Franz Schanovsky, Stanislav Vitantov, and Viktor Sverdlov* as well as those I apologize not to mention here. I want to express my warmest thanks also to the administration staff, namely *Manfred Katterbauer, Ewald* and *Christoph Haslinger*, and to *Renate Winkler*.

This work was supported in part by the Austrian Science Fund FWF, special research program IR-ON, project F2509.

Last but not least, I want to thank my family. My parents made possible all of my studies by their continuous support.

Contents

Kurzfassung	i
Abstract	ii
Acknowledgment	iii
Contents	iv
List of Symbols	viii
Notation	viii
Physical Quantities	viii
Constants	ix
List of Figures	x
List of Tables	xiv
1 Introduction	1
2 Basics of Quantum Cascade Lasers	3
2.1 Fundamentals	3
2.2 Milestones and State-of-the-art	5
2.3 Applications	8

3	Quantum Ballistic Transport	9
3.1	The Effective Mass Approximation	9
3.2	Schrödinger-Poisson Solver	11
3.3	Boundary Conditions	14
3.3.1	Dirichlet and Neumann Boundary Conditions	14
3.3.2	Open Boundary Conditions	15
3.3.2.1	Asymptotic Behavior	15
3.4	Non-Equilibrium Green's Functions	17
4	Quantum Dissipative Transport	19
4.1	Density Matrix Formulation	19
4.1.1	Density Matrix Equations for Dissipative Systems	21
4.1.1.1	Markov Approximation	22
4.1.1.2	The Relaxation Equation	23
4.1.1.3	From the Liouville-von Neumann Equation to the PME	25
4.2	Semiclassical Transport Description	26
4.2.1	Pauli Master Equation	27
4.2.2	Monte Carlo Method	31
5	Scattering Rates	34
5.1	Phonons	34
5.2	From Fermi's Golden Rule to the Total Scattering Rate	35
5.3	Polar Optical Phonon Scattering	36
5.4	Acoustic Deformation Potential Scattering	37
5.5	Optical Deformation Potential Scattering	39
5.6	Intervalley Scattering	39
5.7	Interface Roughness Scattering	39
5.8	Alloy Scattering	41
6	Simulation Results	42
6.1	Quantum Ballistic Transport Calculations	42

CONTENTS

6.1.1	Tunneling Current Density	42
6.1.1.1	Comparison with the Tsu-Esaki Model	43
6.1.1.2	Comparison with the NEGF Approach	46
6.1.2	Optical Gain	50
6.1.2.1	Calculation Results	51
6.2	Design and Performance Investigations	53
6.2.1	A THz QCL	53
6.2.1.1	Structure	53
6.2.1.2	Results	54
6.2.1.3	Interface Roughness Effects	57
6.2.2	Mid-infrared QCL	61
6.2.2.1	Initial Structure	61
6.2.2.2	Optimization of the Collector Barrier	63
6.2.3	Simulation of an Al-free QCL	66
6.2.3.1	Structure	66
6.2.3.2	Results of the Monte Carlo Simulation	68
6.2.3.3	Inclusion of Alloy Scattering	72
7	Summary and Outlook	75
	Appendix	77
A	Derivation of the Effective Mass Equation	77
B	Derivation of the Scattering Rates	80
B.1	Polar Optical Phonon Scattering	80
B.2	Acoustic Deformation Potential Scattering	81
B.3	Optical Deformation Potential Scattering	82
B.4	Intervalley Scattering	83
B.5	Interface Roughness Scattering	83
B.6	Alloy Scattering	85
	Bibliography	87

CONTENTS

Own Publications	97
Curriculum Vitae	98

List of Symbols

Notation

x ... Scalar
 \mathbf{x} ... Vector

Physical Quantities

Symbol	Unit	Description
τ_i	s	Lifetime of i -th state
τ_{tunnel}	s	Tunneling time
ΔE	eV	Energy separation
Ψ	$\text{m}^{-3/2}$	Wave function in three dimensions
A	m^2	Cross-sectional area of the the quantum well structure
\mathbf{k}_{\parallel}	m^{-1}	In-plane wave vector
$\Phi_{\nu\lambda}^{\eta}$	$\text{m}^{-1/2}$	Electron envelope function of ν -th subband, valley η and stage λ
\hat{H}	eV	Total Hamiltonian of the system
E_{α}	eV	Energy of the α -th state
m^*	kg	Effective electron mass
V_0	eV	Conduction band offset
F	Vm^{-1}	External bias field
φ	V	Electrostatic potential
\mathbf{D}	Cm^{-2}	Electric displacement field
ε_s	$\text{AsV}^{-1}\text{m}^{-1}$	Static dielectric permittivity
n	m^{-3}	Electron concentration
E_F	eV	Quasi Fermi level

LIST OF SYMBOLS

Symbol	Unit	Description
N_s	m^{-2}	Electron sheet density
$E_{\nu\lambda}^\eta$	eV	Energy level of ν -th subband in the valley η and stage λ
T	K	Lattice temperature
R_α	1	Reflexion coefficient of state α
T_α	1	Transmission coefficient of state α
\hat{L}	eV	Liouville operator
$\frac{1}{\tau_\alpha^{\alpha'}}$	s^{-1}	Scattering rate between the states α' and α
J	Am^{-2}	Current density
$F_{\alpha'}^\alpha$	1	Form factor between the states α' and α
$I_\alpha^{\alpha'}$	m^{-1}	Overlap integral between the states α' and α

Constants

h	...	Planck constant	$6.6260755 \times 10^{-34} \text{ Js}$
\hbar	...	Reduced Planck constant	$h/(2\pi)$
k_B	...	Boltzmann constant	$1.380662 \times 10^{-23} \text{ JK}^{-1}$
e	...	Elementary charge	$1.6021892 \times 10^{-19} \text{ C}$
m_0	...	Electron rest mass	$9.1093897 \times 10^{-31} \text{ kg}$
ε_0	...	Vacuum permittivity	$8.8541878 \times 10^{-12} \text{ AsV}^{-1}\text{m}^{-1}$

List of Figures

2.1	A generic conduction band profile in two stages of a QCL under an applied bias. The arrow displays the transition $3 \rightarrow 2$, responsible for the laser action, and the moduli squared of the corresponding wave functions are denoted by solid curves.	4
2.2	Timeline of significant QCL developments.	7
3.1	Flowchart of the selfconsistent Schrödinger-Poisson solver. The initial value for the electrostatic potential is set to zero. In the second step the envelope functions and the eigenenergies are calculated according to the Schrödinger equation. The Poisson equation is solved after the determination of the Fermi level. A check of the electrostatic potential update decides whether the iteration terminates.	13
4.1	Anitcrossing between two single well states.	28
4.2	Difference between the semiclassical and coherent picture of coupled quantum wells.	29
4.3	Schematic of three adjacent stages of a QCL under an applied field. Each time an electron in state $ \mathbf{k}_{\parallel}, \nu\eta\lambda\rangle$ undergoes an interstage scattering to a state $ \mathbf{k}'_{\parallel}, \nu'\eta'(\lambda \pm 1)\rangle$, the electron is reinjected into the central region and the corresponding electron charge contributes to the current.	30
4.4	Flow chart of the ensemble Monte Carlo algorithm. The input is provided by a selfconsistent Schrödinger-Poisson solver.	33
6.1	Band structure of the considered FSL at an applied field of 50 kV/cm. . .	44

LIST OF FIGURES

6.2	Current-density voltage characteristics of a GaAs/Al _{0.3} Ga _{0.7} As Fibonacci superlattice at $T = 200\text{K}$	45
6.3	A schematic diagram of the conduction band profile for one and a half periods of the GaAs/Al _{0.33} Ga _{0.67} As QCL for an electric field of 48 kV/cm.	46
6.4	Comparison of the current-voltage characteristics of a GaAs/ Al _{0.33} Ga _{0.67} As QCL calculated using the Robin boundary condition approach with a nonequilibrium Green's functions simulation [1].	47
6.5	The spatial dependences of the real parts of the envelope functions are plotted for different values of the electric field. The solid lines correspond to the solution of the Dirichlet problem and the dashed lines represent the wavefunctions of the Robin problem.	48
6.6	The spatial dependences of the imaginary parts of the envelope functions belonging to the solution of the Robin Problem at $F = 10^3\text{kV/cm}$ (solid line) and $F = 10^{-6}\text{kV/cm}$ (dashed line).	49
6.7	Optical gain of a THz GaAs/Al _{0.15} Ga _{0.85} As QCL driven at 160 A cm^{-2} . The solid line represents the result calculated using the Robin boundary condition approach and the dashed line corresponds to measured values.	51
6.8	Calculated values of the dipole matrix elements for $F = 10^3\text{ kV/cm}$ and $F = 10^{-6}\text{ kV/cm}$. The solid lines represent the solution of the Dirichlet problem and the dashed lines correspond to the solution of the Robin problem.	52
6.9	Calculated conduction band diagram and squared wave functions for a GaAs/Al _{0.15} Ga _{0.85} As QCL under an applied field of 10 kV/cm.	54
6.10	Calculated LO-phonon scattering rates $4 \rightarrow 4$ and $4 \rightarrow 3$ at an applied bias of 10 kV/cm and an operating temperature of 70 K.	55
6.11	Time evolution of the current density at an electric field of 10 kV/cm, with and without Γ -X intervalley scattering, illustrating the good convergence behavior. The current densities averaged over the time are $3.45 \cdot 10^6\text{ A/m}^2$ by including the X valley, and $3.08 \cdot 10^6\text{ A/m}^2$ for the Γ valley only.	56
6.12	Population of the individual subbands as a function of the kinetic energy.	56
6.13	Current density as a function of the applied electric field with and without X valley transport.	57
6.14	Comparison of the energy distributions of subband 4 for different temperatures. The dashed lines show the results without interface roughness scattering and the solid ones illustrate the results including scattering on rough interfaces.	58

LIST OF FIGURES

6.15	Comparison of the energy distributions of subband 3 for different temperatures. The dashed lines show the results without interface roughness scattering and the solid ones illustrate the results including scattering on rough interfaces.	59
6.16	Current density as a function of the applied electric field with and without interface roughness scattering at 70 K.	60
6.17	Current density as a function of the temperature with and without interface roughness scattering.	61
6.18	Conduction band diagram and squared wave functions for a GaAs/Al _{0.45} Ga _{0.55} As QCL in the MIR region under an applied field of 40 kV/cm [2]. The conduction band discontinuity between GaAs and Al _x Ga _{1-x} As layers is taken to be $\Delta E_c = 1.1x$ eV for $0 \leq x \leq 0.45$, and $\Delta E_c = 0.43 + 0.14x$ eV for $0.45 < x \leq 1$	62
6.19	Overlap between the lower Γ -state of the central stage and the upper X-state of the next stage at an electric field of 40 kV/cm in dependence on the Al content.	63
6.20	Γ -X intervalley scattering between the lower state 2 and the upper state 9' of the next stage at $F = 40$ kV/cm.	64
6.21	Electron population of the Γ and X valleys in dependence on the electric field.	64
6.22	Current density as a function of electric field for structure A and structure B, with and without X-valley transport.	65
6.23	Conduction band diagram for an In _{0.53} Ga _{0.47} As/GaAs _{0.51} Sb _{0.49} QCL under an applied field of 30 kV/cm [3]. The upper and lower laser levels are labelled with 3 and 2, respectively.	67
6.24	Voltage-current characteristics at $T = 78$ K.	68
6.25	Current density versus temperature at 5 V and 13 V with and without interface roughness scattering.	69
6.26	Scattering rate due to LO phonon emission as a function of temperature at several bias points.	70
6.27	Energy distributions of the upper and lower laser level with and without taking into account polar optical phonon scattering.	71
6.28	Voltage-current characteristics at 78 K. Comparison between the measured values and the simulation results with and without alloy scattering.	72
6.29	Current density versus temperature at 5 V and 13 V with and without alloy scattering.	73

LIST OF FIGURES

6.30 Current enhancement due to inclusion of alloy scattering for several temperatures. 74

List of Tables

6.1	A few initial generalized FSLs.	46
6.2	Column one contains the applied electric fields in kV/cm. The next three columns show the corresponding energy levels given in meV. Finally the transmission coefficients are given in the last three columns.	50
6.3	Overview of the material parameters used in the simulation presented in this section, illustrated for the well and barrier material, respectively.	53
6.4	Material parameters for the well and barrier material used in the simulation.	66
6.5	Temperature dependence of band gap energies and conduction band discontinuities [4].	74

Chapter 1

Introduction

In 1970, Esaki and Tsu [5] proposed using heterostructures for applications in optoelectronics. The first suggestion to use intersubband transitions in order to create a laser was made by Kazarinov and Suris [6]. Over the past several years, solid-state lasers based on intersubband transitions in semiconductor heterostructures have proved to be very viable sources of radiation [7]. Designed by means of band structure engineering, a successfully working quantum cascade laser (QCL) has first been reported in 1994 [8]. In the following years many important milestones for semiconductor lasers were demonstrated using the semiconductor system $\text{Al}_{0.48}\text{In}_{0.52}\text{As}/\text{Ga}_{0.47}\text{In}_{0.53}\text{As}/\text{InP}$.

The fundamentals of these devices are not bound to a particular material system. The first demonstration of a QCL in a different material system was achieved in 1998 using $\text{GaAs}/\text{Al}_{0.33}\text{Ga}_{0.67}\text{As}$ [9]. AlGaAs based heterostructures are the most widespread and developed ones among compound semiconductors. Moreover they show some significant advantages for the use of processing techniques, which are more suitable for a GaAs than an InP based device. For instance, the standard dry etching techniques, like reactive ion etching or chemically assisted ion beam etching, become more difficult to use when In compounds are present [10]. QCLs may also allow laser operation in materials traditionally considered to have poor optical properties. Indirect bandgap materials such as silicon have minimum electron and hole energies at different momentum values. For interband optical transitions, carriers change momentum through a slow, intermediate scattering process, dramatically reducing the optical emission intensity. Intersubband optical transitions, however, are independent of the relative momentum of conduction band and valence band minima and theoretical proposals for Si/SiGe quantum cascade emitters have been made [11].

However, the performance of QCLs has remarkably improved and devices have been conceived to work in a wide range of wavelengths and temperatures by considering different designs [12]. The emission wavelength has spanned the mid-infrared (MIR) to far-infrared (FIR) spectral range (3 - 190 μm) and QCLs are rapidly acquiring new applications such as free-space telecommunications [13] or chemical spectroscopy in medical applications [14].

QCLs can also be applied for radio-carbon dating and monitoring atmospheric methane levels. Since the emission frequency of intersubband lasers is determined by the design of the widths of the quantum wells and barrier layers, it can be tailored to the application. However, the commercialization of QCLs is in the early stages. For product specific optimization of emitted wavelengths and output performance, simulations of the physical processes are inevitable.

In this dissertation, we will show how the use of a Monte Carlo (MC) simulation based on a semiclassical transport theory is a very useful approach to investigate the physics of QCL operation. To investigate charge transport and the performance in general, we developed a Monte Carlo simulator which includes the relevant scattering mechanisms such as electron-longitudinal optical phonon, acoustic and optical deformation potential, and intervalley scattering. The electron states are evaluated using a selfconsistent Schrödinger-Poisson solver. The simulator has been used to simulate the output characteristics of GaAs based QCLs in the MIR and THz region, respectively.

In Chapter 2, basic fundamentals of QCLs are described and the most important milestones and achievements are discussed. In Chapter 3, the selfconsistent Schrödinger-Poisson solver is accurately described. Special emphasis is laid on the quantum ballistic transport and the theory of open boundary value problems. Chapter 4 deals with the theoretical framework of the density matrix formulation, and the semiclassical transport model and especially the stationary charge transport governed by the Pauli master equation (PME) is presented. The ensemble Monte Carlo procedure is introduced as an efficient approach for simulating transport in QCL structures according to the given Boltzmann-like kinetic equations. The interaction mechanisms are restricted to three stages. Chapter 5 describes the scattering mechanism considered in the Monte Carlo simulator. Chapter 6 presents the simulation results obtained. In particular, current carrying states are obtained by assuming Robin boundary conditions and the presented numerical simulations show that the stationary charge transport can be well described by incorporating a reasonable concept of non-selfadjoint boundary conditions. The method has been applied to several heterostructure designs and the results obtained have been compared to other simulations and to experimental measurements. Furthermore, the developed Monte Carlo simulator is employed to study the output characteristics and special focus was laid on the study of intervalley scattering effects on the carrier dynamics. The results are analyzed with a view to optimization of QCL structures. Chapter 7 summarizes the research performed within this thesis. Furthermore, a discussion of the obtained results as well as an outlook of envisioned and necessary future work are provided.

Chapter 2

Basics of Quantum Cascade Lasers

2.1 Fundamentals

The QCL is an unipolar device made of a sequence of alternating wide band gap and narrow band gap semiconductor layers with typical thicknesses of a few nanometers. Semiconductor layers of narrow bandgap thinner than the De Broglie wavelength of the carriers form quantum wells with quantized states. This one dimensional potential well of finite depth confines carriers to discrete levels in the direction of growth. Orthogonal to the growth direction the carriers are unbound resulting in an energy dispersion of each subband.

These multi quantum well structures form repeated stages where each stage contains an active region and a carrier injector region. Figure 2.1 illustrates the generic conduction band profile in two adjacent stages of a QCL under an applied electric field. Depending on the barrier thicknesses, the exponential tails of the delocalized wave functions can reach the adjacent wells. Due to the quantum confinement multiple minibands are formed in the injector region, whereas in the active region discrete energy levels arise. Coupling of the wells and carrier transfer is provided by quantum mechanical tunneling. The upper lasing level 3 in the active region is filled by electrons from the injector region, that tunnel through the barriers. Radiative transitions from the upper level to the lower lasing level 2 occur if the population inversion condition is satisfied, i.e. the occupation of the upper state exceeds the number of electrons in the lower state significantly. In other words, the relaxation time τ_{32} from the upper state into the lower state has to be greater than the lifetime of the lower state τ_2 , i.e. $\tau_{32} > \tau_2$. Due to interaction of electrons with longitudinal optical (LO) phonons level 2 gets depopulated fastly to level 1. Subsequently, the electrons escape by means of tunneling into the injector region of the adjacent stage. While an electric current flows through a quantum cascade structure, electrons cascade down an energy staircase emitting a photon at each step in the ideal case. Thus an injected electron can theoretically generate as many photons as stages are present. The

cascade of light generated in this way makes the optical power proportional to the number of stages, which points up the capability of QCLs.

So far, we have described the principle of population inversion between the upper and lower state, which can be achieved by designing properly the layer thicknesses and electric field in the active region, assuming the ideal carrier transport path where sufficiently many electrons are injected into level 3 from the preceding injector region after relaxation from level 2 to 1 via LO phonons. In reality also other scattering paths for the electrons are possible. To minimize these effects of leakage currents is a task of QCL design optimization. To achieve lasing, it is necessary to suppress unwanted escape routes by tunneling from the upper level [15]. In order to ensure highly selective injection, electrons are injected into the upper laser level by a resonant tunneling process. Typical tunneling times are of the order of sub-picoseconds and can be approximated as [16]

$$\tau_{\text{tunnel}} \approx \frac{h}{2\Delta E} \quad (2.1)$$

where ΔE denotes the energy separation of the delocalized wave functions in the coupled well system. At too low bias, conduction is low and only minimal current will flow.

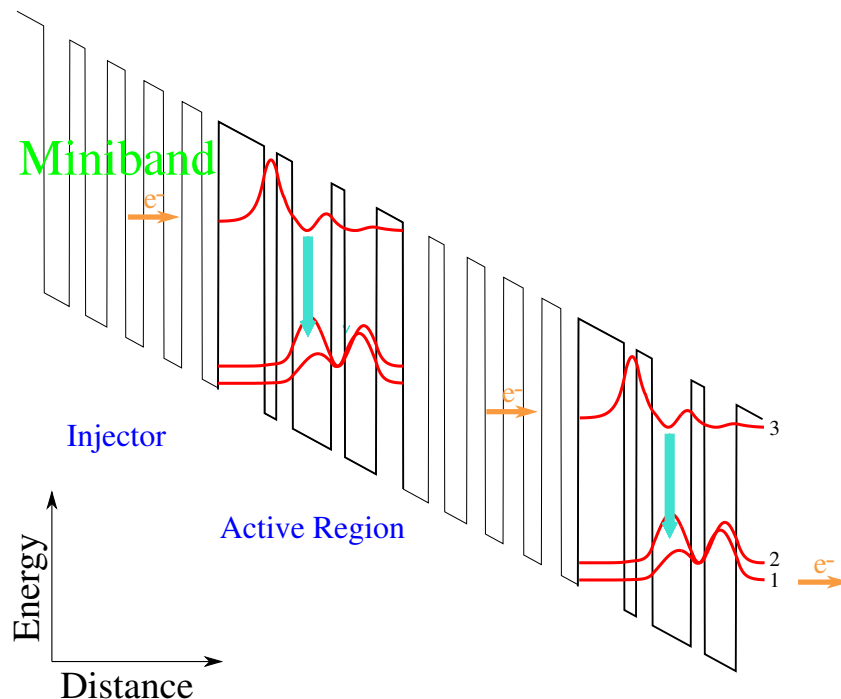


Figure 2.1: A generic conduction band profile in two stages of a QCL under an applied bias. The arrow displays the transition $3 \rightarrow 2$, responsible for the laser action, and the moduli squared of the corresponding wave functions are denoted by solid curves.

When the field increases, the transmission coefficient gets enhanced and the current flow increases. At resonance, where the band edge aligns to a bound state, a local maximum for the transmission coefficient is achieved, leading to a peak in the current flow. Further increase in field results in a sharp decrease in the current flow. Especially in the off-resonance case, scattering mechanisms are capable to route carriers.

Carrier transport can also be affected by thermal effects, like in short-wavelength lasers, where the energetically high upper laser level is located close to the quasi continuum above the barriers. There the electrons may undergo thermal excitation, and thermionic emission from the confined states constitutes. In the continuum, the electric field accelerates the electron freely. Thus they do not partake in the laser action any more.

In general, laser action for a wide range of electric fields can be achieved if a large gain coefficient and a low waveguide loss can be established. The current has to be large enough that the gain compensates the loss. The gain itself mainly depends on the dipole matrix element between the corresponding laser levels and the phenomenological broadening of the transition. It has been shown that a long lifetime for the upper laser level and a short one for the lower level is essential to obtain a high peak gain in QCLs [17], the same criterion as for an efficient population inversion.

Evidently, the understanding of numerous physical processes is essential for the design and optimization of QCLs. Predominantly, suitable waveguiding and population inversion with appropriate radiative transitions must be provided by tailoring the band structure and the lifetimes.

2.2 Milestones and State-of-the-art

Progress advanced quickly after the first demonstration of an intersubband laser in 1994, designed in the Bell Laboratories to emit at $4.2 \mu\text{m}$ wavelength with peak powers in excess of 8 mW in pulsed operation and grown by molecular beam epitaxy [8]. This progress is facilitated basically by the advance in growth techniques and by the improving understanding of bandstructure engineering, resulting in a better control of the electron transport to enable an increase in population inversion and gain. A timeline of the most important achievements is shown in Figure 2.2.

In 1996, MIR QCLs were created that reach a high pulsed power at temperatures up to 320 K and a continuous wave (CW) operation up to 140 K [18]. An active region based on a three-well vertical transition design and a funnel injector were used to optimize the gain. At 300 K a peak pulsed optical power of 200 mW was obtained, where the emission wavelength was about $5.2 \mu\text{m}$. In the same year, long wavelength single-mode QCLs based on an AlInAs/GaInAs heterostructure emitting at $11.2 \mu\text{m}$ were established [19]. Moreover, a continuous wave operation with powers of about 7 mW at a temperature of 10 K was successfully obtained.

One year later, a continuously tunable single-mode laser was provided by a distributed

feedback (DFB) QCL operating above room temperature at 5.4 and 8 μm wavelengths [20]. Due to the alternating refractive index the periodically structured active region acts as a diffraction grating, where the wavelength is determined by the Bragg reflection condition. In the same year, a long wavelength QCL based on a superlattice active region was demonstrated [21]. An intrinsic inversion is achieved by minibands in the active region. Electrons injected by tunneling emit photons corresponding to the energy separation.

The first GaAs/AlGaAs QCL was reported in 1998 [9]. This work demonstrated the validity of QCL principles in a heterostructure material system different from the system InGaAs/AlInAs on InP used before. This QCL structure employed 33 % Al in the barriers and emitted at a wavelength of 9.4 μm under pulse operation up to 140 K. The threshold current density of this device was reduced to an average of 5 kA/cm^2 at 77 K, and a maximum pulsed operation temperature of about 200 K was achieved with a low loss Al-free waveguide [22]. Since the first realization of GaAs/Al_{0.45}Ga_{0.55}As QCLs [23] the device performance has improved significantly. For several active region designs a room temperature pulsed operation has been demonstrated, e.g. a superlattice active region design with an emission wavelength at 12.6 μm [24] and a bound-to-continuum design emitting at 82 μm [25]. Recently, a continuous wave operation with a maximum temperature of 150 K has been achieved due to optimized device processing [26].

The first QCLs with wavelengths larger than 20 μm , in particular at 21.5 and 24 μm , were reported in 2001 [27]. Originating from interminiband transitions in superlattice active regions, laser action is achieved up to 140 K with a peak power of a few mW. The structures were grown by molecular beam epitaxy using an In_{0.53}Ga_{0.47}As/Al_{0.48}In_{0.52}As lattice matched to an InP substrate. Up to this time, these semiconductor lasers had the longest emission wavelength.

One year later, a continuous wave operation of a MIR semiconductor laser above room temperature was demonstrated [28]. At an emission wavelength of 9.1 μm , the optical output power ranged from 17 mW at 292 K to 3 mW at 312 K. In the same year, a prototype of a QCL emitting in the THz region (30 - 300 μm) was reported [29]. Emitting a single mode at 4.4 THz, the device reached an output power of more than 2 mW.

Further notable milestones are the first broadly and continuously tunable external cavity QCL in 2004 [30], and the first high power CW external cavity QCL at room temperature [31].

In 2010, a 100 μm emission of a QCL to a 10° cone was reported [32]. Due to fabricating a metamaterial layer on the output facet, the heavily doped semiconductor acts like a metal at terahertz frequencies.

Nowadays, QCLs operate over a wide wavelength range of 2.9 - 250 μm [33]. Spanning the MIR and THz region, they also operate at room temperature and in continuous wave mode with up to 3 W of optical power.

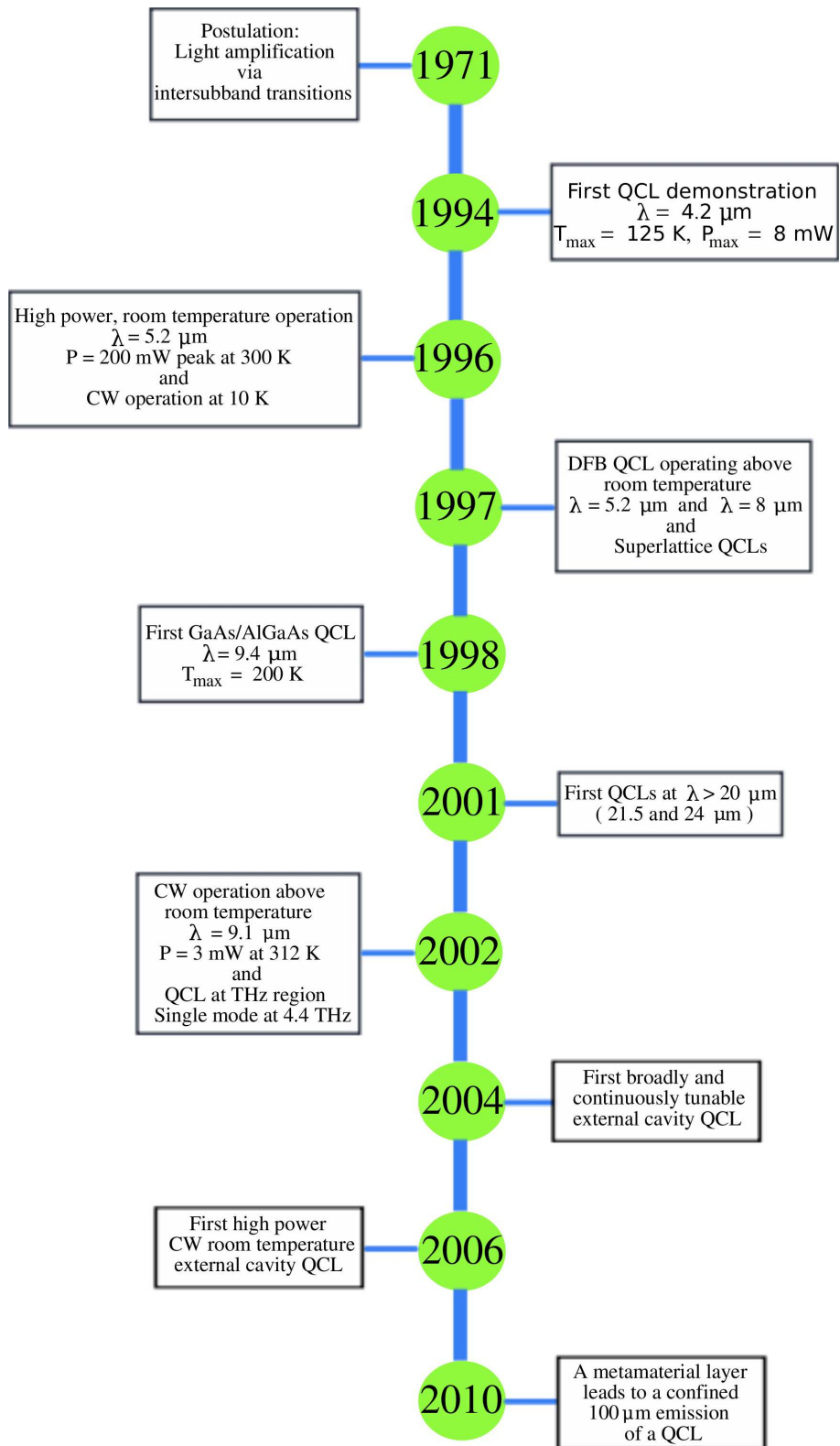


Figure 2.2: Timeline of significant QCL developments.

2.3 Applications

Because of their small size, the possibility to operate at room temperature and high spectral power density, MIR QCLs can find widespread applications in stable process analyzers. For instance, these lasers are able to be used for liquid phase measurements as measuring total petroleum hydrocarbons in water or the determination of glucose and lactate in aqueous solutions [34].

Another important application of QCLs is sensitive nanosecond time-resolved spectroscopy to probe chemical reactions [35]. External Cavity QCLs are a functional infrared source for time-resolved infrared instrumentation and can be used to obtain high sensitive nanosecond spectra in order to detect short lived reaction intermediates and the clarification of reaction mechanisms.

Absorption spectroscopy systems are based on widely tunable QCLs. They are able to detect and measure substances on surfaces, which allows them to identify bulk materials and detect sub-micron films based on their absorption characteristics [36]. This enables to analyze vapors and liquids. Fast analysis, and the ability to work at a distance either through free space or a fiber are key factors for the ability of these systems to analyze trace amounts of explosives.

QCL based optical methods in chemical sensing have many advantages such as high selectivity and real-time detection. This allows the determination of the local concentration of a species with high accuracy and sensitivity. Industrial applications include combustion diagnostics in the power and automobile industries as well as medical diagnostics such as breath analysis for the early detection of ulcer and other diseases, and additionally process control. In the atmospheric science, spectral data are used to determine chemical concentration profiles, which are important for the development of climate models.

Chapter 3

Quantum Ballistic Transport

Under the condition that the size of a device structure is comparable to the De Broglie wavelength of the electron, the transport properties of the device are described by the laws of quantum mechanics. The quantum ballistic regime is valid if the dimension of the structure is reduced below the mean free path of the electron [37]. The basic equations of quantum ballistic device simulations, namely the Poisson equation and the Schrödinger equation, are discussed in this section. Furthermore, we give attention to issues regarding boundary value problems that arise in semiconductor transport theory.

3.1 The Effective Mass Approximation

Primarily, the effective mass approximation was extensively used to describe electronic motion in the presence of slowly varying perturbations [38]. This condition for the validity of the approach is not satisfied, when the differences between the potentials in the well and barrier layers belonging to a quantum well are not small. Thus, the growing interest in quantum well structures led to a remarkable development of the effective mass theory from the regime of weak perturbations to the strong perturbation regime in microstructures [39].

In general, the energy levels and wave functions can be obtained by solving the Schrödinger equation with a proper Hamiltonian. Assuming that the many-body interactions among electrons are negligible, the motion of the electrons can be described by the one-electron Hamiltonian.

We consider electrons in the conduction band of a QCL with an electric field applied in the growth direction of the heterostructure. The total wave function can be written as the product between the periodic Bloch function at the center of the Brillouin zone and an envelope function, which is supposed to vary slowly over one period. When z is the growth direction, the free motion in the in-plane direction can be separated and the wave

function in the quantum well structure is given by [40]

$$\Psi_{\nu\lambda, \mathbf{k}_{\parallel}}^{\eta}(\mathbf{x}) = \frac{1}{\sqrt{A}} e^{i\mathbf{k}_{\parallel} \cdot \mathbf{x}_{\parallel}} \Phi_{\nu\lambda}^{\eta}(z) \quad (3.1)$$

where \mathbf{k}_{\parallel} is the in-plane wave vector, A is the cross-sectional area of the quantum well structure, and $\Phi_{\nu\lambda}^{\eta}(z)$ is the electron envelope function of the ν -th subband in the valley η and stage λ . Under the assumption that the periodic function is the same in all layers and due to equation (3.1) the general form of the Schrödinger equation for the quantum well structure is given by

$$\hat{H}\Phi_{\nu\lambda}^{\eta}(z) = E_{\nu\lambda}^{\eta}\Phi_{\nu\lambda}^{\eta}(z) \quad (3.2)$$

where $E_{\nu\lambda}^{\eta}$ denotes the energy and \hat{H} the total Hamiltonian involving a kinetic and a potential part. Considering a junction at z_0 between the regions of two materials with dissimilar periodic potentials the current conservation is guaranteed by use of the following interface conditions [41]

$$\Phi_{\nu\lambda}^{\eta}(z)|_{z \rightarrow z_0^-} = \Phi_{\nu\lambda}^{\eta}(z)|_{z \rightarrow z_0^+}, \quad \left(\frac{1}{m^*(z)} \frac{d\Phi_{\nu\lambda}^{\eta}(z)}{dz} \right) \Big|_{z \rightarrow z_0^-} = \left(\frac{1}{m^*(z)} \frac{d\Phi_{\nu\lambda}^{\eta}(z)}{dz} \right) \Big|_{z \rightarrow z_0^+} \quad (3.3)$$

where the upscripts "−" and "+" denote the left and right hand sides of the boundary. The condition for matching the derivative includes the effective mass $m^*(z)$. Since the derivative is the momentum operator, the equation (3.3) implies the requirement that the velocity must be the same on both sides to conserve the current. The appropriate hermitian Hamiltonian can be written as

$$\hat{H} = -\frac{\hbar^2}{2} \frac{\partial}{\partial z} \frac{1}{m^*(z)} \frac{\partial}{\partial z} + V(z). \quad (3.4)$$

It is of Sturm-Liouville form, which implies that the eigenvalues are real and the eigenfunctions corresponding to different eigenvalues are orthogonal [42]. The potential applied to the Schrödinger equation takes the form

$$V(z) = V_0(z) - eFz - e\varphi(z). \quad (3.5)$$

Here, V_0 is the conduction band edge, e is the elementary charge, F denotes the external electric field, and φ is the electrostatic potential.

A derivation of the effective mass equation based on the main assumption that the envelope functions are slowly varying on the scale of the lattice period, is provided in Appendix A. In this context, it should be mentioned that there is no possibility of a rigorous derivation. It is about heuristic arguments, which is generally a common practice in quantum mechanics. Nevertheless, for pedagogical purposes it is interesting to gain insight into these details.

3.2 Schrödinger-Poisson Solver

The electronic subbands of the conduction band near the zone center of the Brillouin zone and the corresponding envelope functions are determined by solving the Schrödinger equation selfconsistently with the Poisson equation. Poisson's equation plays a fundamental role in semiconductor device modeling. It is one of the basic equations in electrostatics and can be derived from the Maxwell equation

$$\nabla \cdot \mathbf{D} = \rho \quad (3.6)$$

and the material relation

$$\mathbf{D} = \varepsilon_s \mathbf{F} \quad (3.7)$$

Due to the translational symmetry of QCL structures, the electrostatic potential φ has the same profile in each stage. With $\mathbf{F} = -\nabla\varphi$ it satisfies the Poisson equation [43]

$$\frac{\partial}{\partial z} \left(\varepsilon_s \frac{\partial \varphi}{\partial z} \right) = -\rho(z) \quad (3.8)$$

where ε_s denotes the static dielectric permittivity which is assumed to have an effective constant value within a material segment. The space charge density ρ in stage λ is determined from the carrier and doping concentrations, $n(z)$ and $N_D^+(z)$.

$$\rho(z) = e(N_D^+(z) - n(z)) \quad (3.9)$$

The carrier concentration is related to the wave functions by

$$n(z) = \sum_{\nu, \eta} |\Phi_{\nu\lambda}^\eta(z)|^2 N_s^{\nu\eta} \quad (3.10)$$

where the sum is over the subbands and the valleys, respectively. $N_s^{\nu\eta}$ is the electron sheet density according to [44]

$$N_s^{\nu\eta}(E_F) = \frac{2}{A} \sum_{\mathbf{k}_\parallel} \frac{1}{1 + \exp\left(\frac{E_{\nu\lambda}^\eta(\mathbf{k}_\parallel) - E_F}{k_B T}\right)} \quad (3.11)$$

where the Fermi-Dirac distribution is used for the in-plane electron distribution in each subband, and assuming charge conservation in each stage, a position independent quasi Fermi level E_F can be defined [45]. The presented scheme for the Schrödinger-Poisson solver considers a subproblem not coupled to the transport equation [46]. In the parabolic band approximation the electronic dispersion relation $E_{\nu\lambda}^\eta(\mathbf{k}_\parallel)$ is given by

$$E_{\nu\lambda}^\eta(\mathbf{k}_\parallel) = E_{\nu\lambda}^\eta + \frac{\hbar^2 \mathbf{k}_\parallel^2}{2m_{\nu\lambda}^{\eta*}} \quad (3.12)$$

By means of the "sum-to-integral" rule [47]

$$\frac{1}{A} \sum_{\mathbf{k}_\parallel} = \frac{1}{(2\pi)^2} \int d^2 \mathbf{k}_\parallel = \frac{1}{2\pi} \int_0^\infty k_\parallel dk_\parallel \quad (3.13)$$

and the intergral identity

$$\int \frac{dx}{1+e^x} = \int \frac{e^{-x}}{1+e^{-x}} dx = -\ln(1+e^{-x}) \quad (3.14)$$

the electron sheet density reads

$$N_s^{\nu\eta}(E_F) = \frac{k_B T m_{\nu\lambda}^{\eta*}}{\pi \hbar^2} \ln \left[1 + \exp \left(\frac{E_F - E_{\nu\lambda}^{\eta}}{k_B T} \right) \right] \quad (3.15)$$

The total electron sheet density N_s is determined by the sum of $N_s^{\nu\eta}$ in one stage

$$N_s = \sum_{\nu,\eta} N_s^{\nu\eta}(E_F) \quad (3.16)$$

For a given N_s , the quasi Fermi level E_F is obtained iteratively by solving equation (3.16). Both, the Schrödinger and the Poisson equations are discretized using the finite difference method. The procedures for the selfconsistent calculations are illustrated in Figure 3.1.

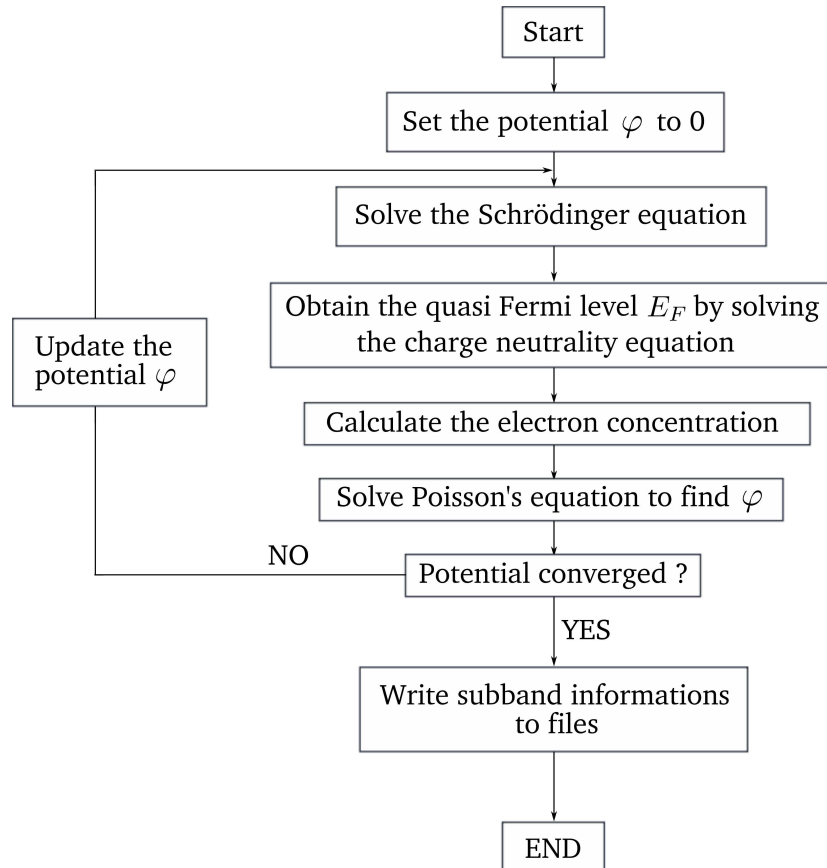


Figure 3.1: Flowchart of the selfconsistent Schrödinger-Poisson solver. The initial value for the electrostatic potential is set to zero. In the second step the envelope functions and the eigenenergies are calculated according to the Schrödinger equation. The Poisson equation is solved after the determination of the Fermi level. A check of the electrostatic potential update decides whether the iteration terminates.

3.3 Boundary Conditions

Stationary transport of charge carriers in semiconductor devices is modeled by means of boundary value problems. In order to investigate systems with net current flows and to obtain current-voltage characteristics of a quantum device, one has to impose boundary conditions which allow current carrying states ¹.

Homogeneous Neumann or Dirichlet boundary conditions yield a self-adjoint Hamiltonian matrix and cannot be used for open systems, since there is no interaction with the environment and the current density is identical zero [48]. A popular approach is to assume periodic boundary conditions which ensure the continuity of the current density, but in fact closes the system and makes the investigation of open system aspects impossible. The simulation domain is usually taken to be finite and the boundaries are physically given by electrical contacts. This leads to the necessity to consider open quantum systems with non-selfadjoint boundary conditions.

In the following chapters, the focus is on boundary conditions which yield current carrying states as solutions of the Schrödinger equation. The theoretical development is based on a Robin boundary condition approach when a solution with the Dirichlet boundary condition is available [49]. A transformation converts a wave function satisfying a Dirichlet boundary condition to a wave function satisfying a Robin boundary condition, enabling particle exchange across the boundary. We also prove that the solution of the Robin problem converges to the solution of the Dirichlet problem, as the energy tends to infinity [50].

3.3.1 Dirichlet and Neumann Boundary Conditions

If Ω is the domain of the device and $\partial\Omega$ denotes the corresponding boundary, it is standard to define self-adjoint realizations of the Hamiltonian by imposing Dirichlet boundary conditions

$$\Phi|_{\partial\Omega} = 0 \tag{3.17}$$

or Neumann boundary conditions

$$\mathbf{n} \cdot \nabla\Phi|_{\partial\Omega} = 0 \tag{3.18}$$

where \mathbf{n} is the outward normal vector of the boundary. The physical meaning of the Neumann boundary condition, which fixes the normal derivative of the field at the boundary, is the constant flux in and out of the simulation domain.

¹This statement is valid for ballistic transport.

3.3.2 Open Boundary Conditions

Let $\Omega = [0, L]$ be the domain of the QCL perpendicular to quantum well layers. Assuming an incoming wave from $-\infty$ with amplitude 1 and no wave incident from $+\infty$, the Schrödinger equation can be solved explicitly outside the domain Ω

$$\Phi_\alpha(z) = \begin{cases} e^{\frac{i}{\hbar}z\sqrt{2m^*E_\alpha}} + R_\alpha e^{-\frac{i}{\hbar}z\sqrt{2m^*E_\alpha}}, & z < 0 \\ T_\alpha e^{\frac{i}{\hbar}z\sqrt{2m^*(E_\alpha-V)}}, & z > L \end{cases}$$

where $V(z) = 0$ on $(-\infty, 0)$ and $V(z) = V(L) = V_L < 0$ for $z > L$. We can deduce a boundary condition at $\partial\Omega \in \{0, L\}$ that does not involve reflection and transmission coefficients [51]

$$\hbar\Phi'_\alpha(0) + i\sqrt{2m^*E_\alpha}\Phi_\alpha(0) = 2i\sqrt{2m^*E_\alpha} \quad (3.19)$$

$$\hbar\Phi'_\alpha(L) - i\sqrt{2m^*(E_\alpha - V)}\Phi_\alpha(L) = 0 \quad (3.20)$$

In order to construct a solution to the Schrödinger equation with Robin boundary conditions when a solution to the same equation with Dirichlet boundary conditions is available, we make use of a Dirichlet-to-Robin transform [49]. If $\Phi^R(z)$ satisfies the Robin boundary condition at $\partial\Omega$

$$\frac{\partial}{\partial z}\Phi^R(z)|_{\partial\Omega} - i\kappa\Phi^R(z)|_{\partial\Omega} = 0 \quad (3.21)$$

the function

$$\Phi^D(z) \equiv \frac{\partial}{\partial z}\Phi^R(z) - i\kappa\Phi^R(z) \quad (3.22)$$

corresponds to the solution of the Dirichlet problem, $\Phi^D(z)|_{\partial\Omega} = 0$. For a given function $\Phi^D(z)$, the general solution to the differential equation (3.22) can be written as

$$\Phi^R(z) = e^{i\kappa z} \int_0^z e^{-i\kappa z'} \Phi^D(z') dz' + C e^{i\kappa z} \quad (3.23)$$

The boundary condition (3.20) gives $\kappa = \sqrt{2m^*(E - V)}/\hbar$. The constant C is evaluated by the requirement that $\Phi^R(z)$ must satisfy the boundary condition (3.19) at $z = 0$, which gives

$$C = 2 \frac{\tilde{\kappa}}{\tilde{\kappa} + \kappa} \quad (3.24)$$

where $\tilde{\kappa} = \sqrt{2m^*E}/\hbar$.

3.3.2.1 Asymptotic Behavior

Including a source term Q , we consider the most general effective mass Schrödinger equation in $\tilde{\Omega} := \Omega \setminus \partial\Omega$

$$\left[-\frac{\hbar^2}{2} \frac{\partial}{\partial z} \frac{1}{m^*(z)} \frac{\partial}{\partial z} + V(z) - E_\alpha \right] \Phi_\alpha(z) = Q_\alpha(z) \quad (3.25)$$

where Ω is the bounded domain with the boundary $\partial\Omega$. The corresponding Green's function is given by [52]

$$G_{\alpha\alpha'}(z, z') = -\frac{2}{c} [\Phi_\alpha(z)\Phi_{\alpha'}^*(z')\Theta(z - z') + \Phi_{\alpha'}(z)\Phi_\alpha^*(z')\Theta(z' - z)] \quad (3.26)$$

where Θ is the Heaviside function and c is a constant. Considering the Dirichlet boundary value problem

$$\Phi^D|_{\partial\Omega} = 0 \quad (3.27)$$

the solution for the effective mass Schrödinger equation at energy $E_\alpha \in \mathbb{R}$ can be written in terms of the Green's function as follows

$$\Phi_\alpha^D(x) = \int_{\tilde{\Omega}} G_{\alpha\alpha'}(z, z') Q_{\alpha'}(z') dz' + \int_{\partial\Omega} G_{\alpha\alpha'}(z, z') \Phi_{\alpha'}^D(z') dz' \quad (3.28)$$

The solution of the Robin boundary value problem

$$\frac{\partial}{\partial N} \Phi^R|_{\partial\Omega} - i\kappa \Phi^R|_{\partial\Omega} = 0 \quad (3.29)$$

converges to Φ^D as $E \rightarrow \infty$.

Proof. Let

$$\tilde{\Phi}_\alpha(z) := \int_{\tilde{\Omega}} G_{\alpha\alpha'}(z, z') Q_{\alpha'}(z') dz' \quad (3.30)$$

Then $\Phi_\alpha^R(z) = \tilde{\Phi}_\alpha(z) + \Phi_\alpha^T(z)$, where $\Phi_\alpha^T(z)$ satisfies

$$\hat{H}\Phi_\alpha^T(z) = 0 \quad \text{in } \tilde{\Omega} \quad (3.31)$$

Due to the boundary condition (3.29) the following relation holds at the boundary

$$\left(\frac{\partial}{\partial N} \Phi_\alpha^T - i\kappa \Phi_\alpha^T \right) \Big|_{\partial\Omega} = - \left(\frac{\partial}{\partial N} \tilde{\Phi}_\alpha - i\kappa \tilde{\Phi}_\alpha \right) \Big|_{\partial\Omega} \quad (3.32)$$

In general, Φ_α^T can be written in the form

$$\Phi_\alpha^T(z) = \int_{\partial\Omega} G_{\alpha\alpha'}(z, z') \varphi_{\alpha'}(z') dz' \quad (3.33)$$

where φ can be determined by inserting equation (3.33) into the condition (3.32), which yields the following equation

$$\lim_{z \rightarrow \partial\Omega} \left(\int_{\partial\Omega} \left(\frac{\partial}{\partial N} G_{\alpha\alpha'}(z, z') \right) \varphi_{\alpha'}(z') dz' - i\kappa \int_{\partial\Omega} G_{\alpha\alpha'}(z, z') \varphi_{\alpha'}(z') dz' \right) = \lim_{z \rightarrow \partial\Omega} \left(-\frac{\partial}{\partial N} \tilde{\Phi}_\alpha(z) + i\kappa \tilde{\Phi}_\alpha(z) \right)$$

Since $\kappa = O(\sqrt{E_\alpha})$, we get

$$\lim_{z \rightarrow \partial\Omega} \int_{\partial\Omega} G_{\alpha\alpha'}(z, z') \varphi_{\alpha'}(z') dz' = \lim_{z \rightarrow \partial\Omega} \left(-\tilde{\Phi}_\alpha(z) + O\left(\frac{1}{\sqrt{E_\alpha}}\right) \right) \quad (3.34)$$

Inserting the equations (3.27) and (3.28) yields

$$T_{\alpha\alpha'} \varphi_{\alpha'} = T_{\alpha\alpha'} \Phi_{\alpha'}^D + O\left(\frac{1}{\sqrt{E_\alpha}}\right) \quad (3.35)$$

where the operator T is defined as follows

$$T_{\alpha\alpha'} \Phi_{\alpha'}(z') = \int_{\partial\Omega} G_{\alpha\alpha'}(\partial\Omega, z') \Phi_{\alpha'}(z') dz' \quad (3.36)$$

Thus,

$$\begin{aligned} \Phi_\alpha^R(z) &= \tilde{\Phi}_\alpha(z) + \int_{\partial\Omega} G_{\alpha\alpha'}(z, z') \Phi_{\alpha'}^D(z') dz' + O\left(\frac{1}{\sqrt{E_\alpha}}\right) \\ &= \Phi_\alpha^D(z) + O\left(\frac{1}{\sqrt{E_\alpha}}\right) \end{aligned} \quad (3.37)$$

completing the proof. \square

3.4 Non-Equilibrium Green's Functions

The NEGF formalism provides a generalized microscopic theory for quantum transport. It addresses the problem of dissipative transport and describes open systems fully quantum mechanically. The theory behind it is deeply rooted in the many-body theory [53].

The information of the many-particle system is put into self energies, which are part of the equations of motion for the Green's functions. The Green's functions can be calculated from perturbation theory and describe the correlation between two operators at times t and t' . A detailed description and justification of the Green's functions and self energies can be found for instance in the work of Datta [54]. Here, I will only summarize the most important definitions and provide a physical interpretation.

The Hamiltonian of an open system coupled to a reservoir can be written as [55]

$$\hat{H} = \begin{pmatrix} \hat{H}_D & \sigma \\ \sigma^\dagger & \hat{H}_R \end{pmatrix}$$

\hat{H}_D and \hat{H}_R denote the Hamilton operators of the device and reservoir, respectively, and σ is the coupling matrix. The corresponding Schrödinger equation of the channel-reservoir

system can be expressed as [56]

$$E \begin{pmatrix} \psi_D \\ \psi_R \end{pmatrix} = \begin{pmatrix} \hat{H}_D & \sigma \\ \sigma^\dagger & \hat{H}_R \end{pmatrix} \begin{pmatrix} \psi_D \\ \psi_R \end{pmatrix}$$

ψ_D and ψ_R denote the wave functions of the channel and the reservoir. The steady state equation for the Green's function is defined as

$$(\mathbb{1}E - \hat{H})G = \mathbb{1} \quad (3.38)$$

Thus, the corresponding Green's function to the device-reservoir system can be written as

$$\begin{pmatrix} G & G_{DR} \\ G_{RD} & G_R \end{pmatrix} = \begin{pmatrix} \mathbb{1}E - \hat{H}_D & -\sigma \\ -\sigma^\dagger & \mathbb{1}E - \hat{H}_R \end{pmatrix}^{-1}$$

The coupling between the device and the reservoir is described by G_{DR} and G_{RD} . The retarded Green's function G reads

$$G = (\mathbb{1}E - \hat{H}_D - \Sigma(E))^{-1} \quad (3.39)$$

and includes the self energy which describes the interaction between the device and the reservoir [57]. The inclusion of the self energy reduces the Green's function of the reservoir to the dimension of the Hamiltonian of the device. The self energy is determined iteratively and satisfies

$$\Sigma = \sigma G \sigma^\dagger \quad (3.40)$$

The matrix form of the density of states is the spectral function A_s which is given by

$$A_s(E) = i(G(E) - G^\dagger(E)) \quad (3.41)$$

The electron density is provided by the density matrix

$$n = \frac{1}{2\pi} \int_0^\infty f_E(E - E_F) A(E) dE \quad (3.42)$$

where f_E is the Fermi-Dirac distribution function and E_F denotes the Fermi energy.

Chapter 4

Quantum Dissipative Transport

Charge transport simulations according to the non-equilibrium Green's function (NEGF) method need enormous computation time and have to be carefully customized for each particular structure. Since recent theoretical studies showed that the steady state transport in QCLs is incoherent and the semiclassical description found to be satisfactory [58], a simpler approach than NEGF can be used. Although coherent oscillations of the population inversion were observed, the resulting steady state transport is incoherent as the oscillations are damped to the sub-picosecond timescale which is considerable shorter than the average transit time across one stage. Here, we present a rigorous Monte Carlo method based on a semiclassical transport description which takes much less computational time than simulations based on the NEGF formalism.

4.1 Density Matrix Formulation

The density matrix formalism describes the statistical distribution of quantum states in a system [59]. This method allows to treat an ensemble of particles statistically.

Pure States:

The quantum subsystem is described in a Hilbert space of basis functions $\{\Phi_1, \Phi_2, \dots\}$ and a wave function Ψ represents a generic particle from the ensemble according to

$$|\Psi\rangle = \sum_i c_i |\Phi_i\rangle \quad (4.1)$$

In the linear combination, the coefficients c_i are time dependent and describe the time propagation of the quantum subsystem [60], and

$$c_i = \langle \Phi_i | \Psi \rangle \quad (4.2)$$

The density operator describes the probability distribution in a system. It takes the form of a projection operator and is defined by

$$\hat{\rho}(t) = |\Psi(t)\rangle\langle\Psi(t)| \quad (4.3)$$

The probability of finding a system in state $|\Phi_i\rangle$ is described by the diagonal elements ρ_{ii} . The degree of coherence is described by the polarization between states $|\Phi_i\rangle$ and $|\Phi_j\rangle$, which is included in the off-diagonal elements ρ_{ij} . The total population density is conserved, which implies

$$\text{Tr}(\hat{\rho}) = \sum_i \rho_{ii} = 1 \quad (4.4)$$

The expression for the expectation value of an operator can be written as

$$\begin{aligned} \langle\Psi|\hat{O}|\Psi\rangle &= \sum_i \sum_j c_i^* c_j \langle\Phi_i|\hat{O}|\Phi_j\rangle = \sum_i \sum_j c_i^* c_j \hat{O}_{ij} \\ &= \sum_i \sum_j \rho_{ji}^* \hat{O}_{ij} = \sum_i \sum_j \rho_{ij} \hat{O}_{ij} \\ &= \text{Tr}[\hat{\rho}\hat{O}] \end{aligned} \quad (4.5)$$

Mixed States:

A mixed state is an incoherent mixture of pure states $|\Psi^{(j)}\rangle$, ($j = 1, 2, \dots, N$) with statistical weights p_j which obey [61]

$$\sum_{j=1}^N p_j = 1$$

The average value of \hat{O} in the mixed state is given by

$$\langle\hat{O}\rangle = \sum_{j=1}^N p_j \langle\Psi^{(j)}|\hat{O}|\Psi^{(j)}\rangle \quad (4.6)$$

The density matrix depends on the pure states involved in the mixed state and their statistical weights according to

$$\hat{\rho} = \sum_{j=1}^N p_j |\Psi^{(j)}\rangle\langle\Psi^{(j)}| \quad (4.7)$$

The time evolution of the density matrix is obtained by taking the time derivative of the density operator

$$i\hbar \frac{\partial \hat{\rho}}{\partial t} = [\hat{\rho}, \hat{H}] \quad (4.8)$$

with $\hat{H} = \hat{H}_0 + \hat{H}'$, and \hat{H}' represents a perturbation. This equation of motion is known as the quantum Liouville equation. Due to the linear transformation of the density operator on the r.h.s in equation (4.8), it is possible to define a linear operator \hat{L} which yields

$$\frac{\partial \hat{\rho}}{\partial t} = -\frac{i}{\hbar} \hat{L} \hat{\rho} \quad (4.9)$$

where \hat{L} denotes the so called Liouville operator

$$\hat{L}_{ij,mn} = \hat{H}_{im}\delta_{jn} - \hat{H}_{jn}^*\delta_{im}$$

If N is the number of states in the system, the superoperator \hat{L} is a $N^2 \times N^2$ matrix and ρ is a N^2 dimensional vector. Thus, systems with many states may give rise to insuperable computational challenges.

4.1.1 Density Matrix Equations for Dissipative Systems

We consider a system which is open and in permanent contact with its environment. Under certain conditions the system which is initially in a non-equilibrium state will go over into an equilibrium state after some time. This relaxation process is irreversible.

Let S denote an open quantum system which is coupled to another quantum system R , the environment. The density matrix characterizing the total system is denoted by $\rho(t)$ and the total Hamiltonian by $\hat{H} = \hat{H}_S + \hat{H}_R + \hat{H}'$. In the Schrödinger picture, the equation of motion for the density matrix is given by the Liouville-von Neumann equation

$$\frac{\partial \rho(t)}{\partial t} = -\frac{i}{\hbar}[\hat{H}_0, \rho(t)] - \frac{i}{\hbar}[\hat{H}', \rho(t)] \quad (4.10)$$

where $\hat{H}_0 = \hat{H}_S + \hat{H}_R$. Within the interaction picture, the time evolution of the density matrix is controlled only by the interaction Hamiltonian according to

$$\frac{\partial \rho_I(t)}{\partial t} = -\frac{i}{\hbar}[\hat{H}'(t), \rho_I(t)] \quad (4.11)$$

Inserting the formal integration

$$\rho_I(t) = \rho_I(0) - \frac{i}{\hbar} \int_0^t dt' [\hat{H}'(t'), \rho_I(t')]$$

into the r.h.s of equation (4.11), the equation of motion for ρ_I can be expressed as

$$\frac{\partial \rho_I(t)}{\partial t} = -\frac{i}{\hbar}[\hat{H}(t), \rho_I(0)] + \frac{1}{\hbar^2} \int_0^t dt' [\hat{H}'(t), [\hat{H}'(t'), \rho_I(t')]] \quad (4.12)$$

The reduced density matrix ρ_I^S which describes the system S is obtained by taking the trace over all variables of system R according to [62]

$$\rho_I^S(t) = \text{Tr}_R(\rho_I(t)) \quad (4.13)$$

It is assumed that the interaction starts at $t = 0$ and that the two systems are uncorrelated prior to this time. Thus

$$\rho_I(0) = \rho^S(0)\rho^R(0) \quad (4.14)$$

In order to have an irreversible process, it is assumed that R has so many degrees of freedom that it is described by a thermal equilibrium distribution, independent on the amount of energy transferred to it from the system S [63]. Hence

$$\rho_I(t) = \rho_I^S(t)\rho^R(0) \quad (4.15)$$

This is the fundamental condition for irreversibility. Using these approximations, the equation of motion for the reduced density matrix can be written as

$$\frac{\partial \rho_I^S(t)}{\partial t} = -\frac{i}{\hbar} \text{Tr}_R[\hat{H}'(t), \rho^S(0)\rho^R(0)] - \frac{1}{\hbar^2} \int_0^t dt' \text{Tr}_R[\hat{H}'(t), [\hat{H}'(t'), \rho_I^S(t')\rho^R(0)]] \quad (4.16)$$

According to this equation, the behavior of the system depends on the past events in the time interval $[0, t]$, since the integral contains $\rho_I^S(t')$. However, the system S is coupled to the reservoir which causes a damping that destroys the "knowledge" of the past behavior. These considerations lead to the assumption that the system loses all memory of the past. Thus, the substitution

$$\rho_I^S(t') \rightarrow \rho_I^S(t) \quad (4.17)$$

is necessary, which is known as the Markov approximation.

4.1.1.1 Markov Approximation

In general, the interaction operator can be expressed as

$$\hat{H}' = \sum_i \hat{Q}_i^S \hat{Q}_i^R \quad (4.18)$$

where \hat{Q}^S and \hat{Q}^R denote the operators of the dynamic system and the reservoir, respectively. In the interaction picture we have

$$\hat{Q}_i^S(t) = e^{i\hat{H}_S t/\hbar} \hat{Q}_i^S e^{-i\hat{H}_S t/\hbar} \quad (4.19)$$

and

$$\hat{Q}_i^R(t) = e^{i\hat{H}_R t/\hbar} \hat{Q}_i^R e^{-i\hat{H}_R t/\hbar} \quad (4.20)$$

Inserting the interaction operator of this form and the substitution (4.17) into the equation (4.16) and taking into account that the operators \hat{Q}_i^S and \hat{Q}_i^R commute, yields

$$\begin{aligned} \frac{\partial \rho_I^S(t)}{\partial t} = & -\frac{i}{\hbar} \sum_i \left[\hat{Q}_i^S(t) \rho_I^S(0) \text{Tr}_R(\hat{Q}_i^R(t) \rho^R(0)) - \rho_I^S(0) \hat{Q}_i^S(t) \text{Tr}_R(\hat{Q}_i^R(t) \rho^R(0)) \right] \\ & - \frac{1}{\hbar^2} \sum_{ij} \int_0^t dt' \left[(\hat{Q}_i^S(t) \hat{Q}_j^S(t') \rho_I^S(t) - \hat{Q}_j^S(t') \rho_I^S(t) \hat{Q}_i^S(t)) \text{Tr}_R(\hat{Q}_i^R(t) \hat{Q}_j^R(t') \rho^R(0)) \right. \\ & \left. - (\hat{Q}_i^S(t) \rho_I^S(t) \hat{Q}_j^S(t') - \rho_I^S(t) \hat{Q}_j^S(t') \hat{Q}_i^S(t)) \text{Tr}_R(\hat{Q}_j^R(t') \hat{Q}_i^R(t) \rho^R(0)) \right] \quad (4.21) \end{aligned}$$

Let $|r\rangle$ denote the eigenstates of \hat{H}_R . Then, the expectation values appearing in the first term in equation (4.21) can be written as

$$\begin{aligned}\langle \hat{Q}_i^R(t) \rangle &= \text{Tr}_R(\hat{Q}_i^R(t)\rho^R(0)) \\ &= \sum_r \langle r | \hat{Q}_i^R(t)\rho^R(0) | r \rangle\end{aligned}$$

Under the assumption that the interaction operators don't have diagonal elements in this representation (no average energy shifts), the first term in equation (4.21) vanishes, since $\langle \hat{Q}_i^R(t) \rangle = 0$ [64]. The time correlation functions

$$\langle \hat{Q}_i^R(t)\hat{Q}_j^R(t') \rangle = \text{Tr}_R(\hat{Q}_i^R(t)\hat{Q}_j^R(t')\rho^R(0))$$

describe the average correlation between interactions occurring at times t and t' . The reservoir dissipates quickly the effects of its interaction with the system S . Thus

$$\langle \hat{Q}_i^R(t)\hat{Q}_j^R(t') \rangle \neq 0, \quad \text{for } t - t' \lesssim \tau_R$$

where τ_R denotes the correlation time of the reservoir. For $t - t' > \tau_R$, interactions become less correlated and the correlation functions satisfy

$$\langle \hat{Q}_i^R(t)\hat{Q}_j^R(t') \rangle \approx 0$$

On the basis of the last considerations we will discuss the Markov approximation. It follows that the integral in equation (4.16) is nonzero only for t' in the time interval $[t - \tau_R, t]$. Outside this interval, the values of $\rho_I^S(t')$ have negligible influence on the time derivative of $\rho_I^S(t)$. The Markov approximation holds if τ_R is much smaller than a characteristic time that is required for $\rho_I^S(t)$ to change considerably on a macroscopic scale [65].

4.1.1.2 The Relaxation Equation

Since the correlation functions are stationary and depend only on the time difference $t'' = t - t'$

$$\langle \hat{Q}_i^R(t)\hat{Q}_j^R(t') \rangle = \langle \hat{Q}_i^R(t - t')\hat{Q}_j^R \rangle$$

the equation of motion of the reduced density matrix can be written as

$$\begin{aligned}\frac{\partial \rho_I^S(t)}{\partial t} = & - \frac{1}{\hbar^2} \sum_{ij} \int_0^\infty dt'' \left([\hat{Q}_i^S(t), \hat{Q}_j^S(t - t'')\rho_I^S(t)] \langle \hat{Q}_i^R(t'')\hat{Q}_j^R \rangle \right. \\ & \left. - [\hat{Q}_i^S(t), \rho_I^S(t)\hat{Q}_j^S(t - t'')] \langle \hat{Q}_j^R\hat{Q}_i^R(t'') \rangle \right)\end{aligned}\quad (4.22)$$

where the upper integration limit is extended to infinity with negligible error under the Markov approximation. Let $\{|\beta\rangle, |\beta'\rangle, \dots\}$ denote the eigenstates of \hat{H}_S , where $|\beta\rangle =$

$|\lambda, \eta, \nu, \mathbf{k}_{\parallel}\rangle$. Here, η is the subband index, ν denotes the valley index, λ is the index of the stage, and \mathbf{k}_{\parallel} is the in-plane wave vector. Then

$$\langle \beta' | \hat{Q}_i^S(t) | \beta \rangle = e^{i\omega_{\beta'\beta}t} \langle \beta' | \hat{Q}_i^S | \beta \rangle, \quad \omega_{\beta'\beta} = (E_{\beta'} - E_{\beta})/\hbar$$

one obtains after some algebra

$$\langle \beta' | \frac{\partial \rho_I^S(t)}{\partial t} | \beta \rangle = \sum_{\gamma'\gamma} \langle \gamma' | \rho_I^S(t) | \gamma \rangle R_{\beta'\beta}^{\gamma'\gamma} e^{i(E_{\beta'} - E_{\beta} - E_{\gamma'} + E_{\gamma})t/\hbar} \quad (4.23)$$

where the following abbreviations are used

$$\begin{aligned} R_{\beta'\beta}^{\gamma'\gamma} &= \left(- \sum_{\mu} \delta_{\gamma\beta} \Gamma_{\gamma'\mu\mu\beta'}^+ + \Gamma_{\beta\gamma\gamma'\beta'}^+ + \Gamma_{\beta\gamma\gamma'\beta'}^- - \sum_{\mu} \delta_{\gamma'\beta'} \Gamma_{\beta\mu\mu\gamma}^- \right) e^{i(\omega_{\gamma'\beta'} + \omega_{\gamma\beta})t} \\ \Gamma_{\zeta\mu\gamma\beta}^+ &= \frac{1}{\hbar^2} \sum_{ij} \langle \zeta | \hat{Q}_i^S | \mu \rangle \langle \gamma | \hat{Q}_j^S | \beta \rangle \int_0^{\infty} dt'' e^{-i\omega_{\gamma\beta}t''} \langle \hat{Q}_i^R(t'') \hat{Q}_j^R \rangle \\ \Gamma_{\zeta\mu\gamma\beta}^- &= \frac{1}{\hbar^2} \sum_{ij} \langle \zeta | \hat{Q}_j^S | \mu \rangle \langle \gamma | \hat{Q}_i^S | \beta \rangle \int_0^{\infty} dt'' e^{-i\omega_{\zeta\mu}t''} \langle \hat{Q}_j^R \hat{Q}_i^R(t'') \rangle \end{aligned}$$

Considering the case of energy conservation, the time dependent exponential vanishes. It can be shown that after transformation into the Schrödinger picture the equations of motion of the reduced density matrices can be written as [66]

$$\langle \beta' | \frac{\partial \rho^S(t)}{\partial t} | \beta \rangle = -\frac{i}{\hbar} \langle \beta' | [\hat{H}_S, \rho^S(t)] | \beta \rangle + \delta_{\beta\beta'} \sum_{\gamma} \langle \gamma | \rho^S(t) | \gamma \rangle S_{\beta\gamma} - \chi_{\beta'\beta} \langle \beta' | \rho^S(t) | \beta \rangle \quad (4.24)$$

where

$$S_{\gamma\beta} = \Gamma_{\beta\gamma\gamma\beta}^+ + \Gamma_{\beta\gamma\gamma\beta}^- \quad (4.25)$$

and

$$\chi_{\beta'\beta} = \sum_{\mu} (\Gamma_{\beta'\mu\mu\beta'}^+ + \Gamma_{\beta\mu\mu\beta}^-) - \Gamma_{\beta\beta\beta'\beta'}^+ - \Gamma_{\beta\beta\beta'\beta'}^- \quad (4.26)$$

Equation (4.24) is called the generalized Master equation and describes the irreversible behavior of a system. In order to get an interpretation of the occurring parameters, we take a look at the rate of change of the diagonal elements of the density matrix. For the diagonal elements, the Schrödinger picture is equivalent to the interaction picture. From the results determined above, it is straightforward to obtain

$$\frac{d}{dt} \rho_{\beta\beta}(t) = \sum_{\gamma \neq \beta} \rho_{\gamma\gamma}(t) S_{\beta\gamma} - \rho_{\beta\beta}(t) \sum_{\gamma \neq \beta} S_{\gamma\beta} \quad (4.27)$$

This equation is called the Pauli Master equation which plays a fundamental role in modern statistics and can be used in many problems in physics and chemical kinetics

[67]. The diagonal elements of the density matrix give the probability of finding the corresponding level occupied at time t . Since the probability increases due to transitions from $|\gamma\rangle$ to $|\beta\rangle$, and decreases as a result of transitions from $|\beta\rangle$ to other states $|\gamma\rangle$, the parameters $S_{\beta\gamma}$ describe the probability per unit time for the transitions $|\gamma\rangle \rightarrow |\beta\rangle$.

Now we take a more detailed look at the transitions rates. Making use of equation (4.20), the transition rate can be written as

$$\begin{aligned}
 S_{\gamma\beta} &= \Gamma_{\beta\gamma\gamma\beta}^+ + \Gamma_{\beta\gamma\gamma\beta}^- \\
 &= \frac{1}{\hbar^2} \sum_{ij} \sum_{rr'} \langle r | \hat{Q}_i^S | \gamma \rangle \langle \gamma | \hat{Q}_j^S | r \rangle \langle r' | \hat{Q}_i^R | r \rangle \langle r | \hat{Q}_j^R | r' \rangle \langle r' | \rho^R | r' \rangle \int_0^\infty dt'' e^{i(E_{r'} - E_r - \hbar\omega_{\gamma\beta})t''/\hbar} \\
 &\quad + \frac{1}{\hbar^2} \sum_{rr'} \langle r | \hat{Q}_j^S | \gamma \rangle \langle \gamma | \hat{Q}_i^S | r \rangle \langle r' | \hat{Q}_j^R | r \rangle \langle r | \hat{Q}_i^R | r' \rangle \langle r' | \rho^R(0) | r' \rangle \int_0^\infty dt'' e^{i(E_{r'} - E_r - \hbar\omega_{\beta\gamma})t''/\hbar} \\
 &= \frac{2\pi}{\hbar} \sum_{rr'} |\langle \gamma, r | \hat{H}' | \beta, r' \rangle|^2 \langle r' | \rho^R(0) | r' \rangle \delta(E_{r'} - E_r - \hbar\omega_{\gamma\beta})
 \end{aligned} \tag{4.28}$$

This is the "Golden Rule" for a transition from level $|\beta\rangle$ to level $|\gamma\rangle$. In order to ensure the energy conservation

$$E_r - E_{r'} = E_\beta - E_\gamma$$

the reservoir undergoes simultaneously a transition from a state $|r'\rangle$ to $|r\rangle$. The diagonal elements $\langle r' | \rho^R(0) | r' \rangle$ describe the probability of finding the reservoir in a state with energy E_r . Reservoirs are in thermal equilibrium. Hence, such a system is represented by an incoherent sum of energy eigenstates with statistical weights¹. Equation (4.27) holds for closed systems. For open systems, a term describing the interaction with the electrical borders has to be added.

$$\frac{d}{dt} \rho_{\beta\beta}(t) = \sum_{\gamma \neq \beta} \rho_{\gamma\gamma}(t) S_{\beta\gamma} - \rho_{\beta\beta}(t) \sum_{\gamma \neq \beta} S_{\gamma\beta} + \left(\frac{\partial \rho_{\beta\beta}}{\partial t} \right)_{\text{res}} \tag{4.29}$$

4.1.1.3 From the Liouville-von Neumann Equation to the PME

The derivation of the Pauli Master equation can be simplified, if the interaction term in equation 4.10 is approximated by a relaxation term

$$\frac{d\rho}{dt} = \frac{i}{\hbar} [\rho, \hat{H}] + \left(\frac{\partial \rho}{\partial t} \right)_{\text{res}} - \frac{\rho - \rho^{\text{eq}}}{\tau_s} \tag{4.30}$$

The last term on the r.h.s expresses the weak interaction with the surroundings. The limit $\tau_s \rightarrow \infty$ will be taken in the end. Considering the matrix element of the above equation

¹In the case of interaction with phonons, one has to consider the Bose-Einstein statistics.

over the eigenstates $|\alpha\rangle$ of the unperturbed Hamiltonian \hat{H}_0 , one gets

$$\begin{aligned} \frac{d\rho_{\beta\beta'}}{dt} = & \frac{i}{\hbar}\rho_{\beta\beta'}(E_\beta - E_{\beta'} + i\hbar/\tau_s) + \frac{i}{\hbar} \sum_{\beta'' \neq \beta, \beta'} [\rho_{\beta\beta''} \langle \beta'' | \hat{H}_{\text{int}} | \beta \rangle - \langle \beta' | \hat{H}_{\text{int}} | \beta'' \rangle \rho_{\beta''\beta'}] \\ & + \frac{i}{\hbar} \langle \beta | \hat{H}_{\text{int}} | \beta' \rangle (\rho_{\beta\beta} - \rho_{\beta'\beta'}) + \frac{i}{\hbar} \rho_{\beta\beta'} [\langle \beta | \hat{H}_{\text{int}} | \beta \rangle - \langle \beta' | \hat{H}_{\text{int}} | \beta' \rangle] + \left(\frac{\partial \rho}{\partial t} \right)_{\text{res}} \end{aligned}$$

Introducing renormalized energies $E_\beta \rightarrow E_\beta + \langle \beta | \hat{H}_{\text{int}} | \beta \rangle$, the time evolution of the diagonal elements of the density matrix can be written as

$$\frac{d\rho_{\beta\beta}}{dt} = \frac{i}{\hbar} \sum_{\beta' \neq \beta} [\rho_{\beta\beta'} \langle \beta' | \hat{H}_{\text{int}} | \beta \rangle - \langle \beta | \hat{H}_{\text{int}} | \beta' \rangle \rho_{\beta'\beta}] + \left(\frac{\partial \rho}{\partial t} \right)_{\text{res}} \quad (4.31)$$

$(\partial\rho/\partial t)_{\text{res}}$ is assumed to be of order $O(\alpha_c^0)$, where α_c denotes the strength of the interaction Hamiltonian. Equation (4.31) implies that the off diagonal elements of the density matrix are of order $O(\alpha_c^{-1})$. To the lowest order, $O(\alpha_c^{-1})$, one can obtain

$$0 = \frac{i}{\hbar} \rho_{\beta\beta'} (E_{\beta'} - E_\beta + i\hbar/\tau_s) + \frac{i}{\hbar} \langle \beta | \hat{H}_{\text{int}} | \beta' \rangle (\rho_{\beta\beta} - \rho_{\beta'\beta'})$$

which implies that $\rho_{\beta\beta}$ is of the order $O(\alpha_c^{-2})$. Rewriting the last equation as

$$\rho_{\beta\beta'} = \frac{\langle \beta | \hat{H}_{\text{int}} | \beta' \rangle}{E_\beta - E_{\beta'} - i\hbar/\tau_s} (\rho_{\beta\beta} - \rho_{\beta'\beta'})$$

and inserting into equation (4.31), yields

$$\frac{\partial \rho_{\beta\beta}}{\partial t} = \frac{i}{\hbar} \sum_{\beta' \neq \beta} |\langle \beta | \hat{H}_{\text{int}} | \beta' \rangle|^2 (\rho_{\beta\beta} - \rho_{\beta'\beta'}) \left(\frac{1}{E_\beta - E_{\beta'} - i\hbar/\tau_s} - \frac{1}{E_\beta - E_{\beta'} + i\hbar/\tau_s} \right) + \left(\frac{\partial \rho_{\beta\beta}}{\partial t} \right)_{\text{res}} \quad (4.32)$$

Making use of

$$\lim_{\zeta \rightarrow 0} \frac{1}{x - i\zeta} = \frac{1}{x} + i\pi\delta(x)$$

one gets for $\tau_s \rightarrow \infty$

$$\frac{d\rho_{\beta\beta}}{dt} = -\frac{2\pi}{\hbar} \sum_{\beta' \neq \beta} |\langle \beta | \hat{H}_{\text{int}} | \beta' \rangle|^2 (\rho_{\beta\beta} - \rho_{\beta'\beta'}) \delta(E_\beta - E_{\beta'}) + \left(\frac{\partial \rho_{\beta\beta}}{\partial t} \right)_{\text{res}} \quad (4.33)$$

which is formally identical to equation 4.29.

4.2 Semiclassical Transport Description

In semiclassical transport theory, electron transport in semiconductor devices is described by the Boltzmann equation given as [68]

$$\frac{\partial f_\nu}{\partial t} + \mathbf{v} \cdot \nabla_{\mathbf{x}} f_\nu + \frac{d\mathbf{p}}{dt} \cdot \nabla_{\mathbf{p}} f_\nu = \sum_{\mathbf{k}'\nu'} \{ S_{\nu'}^\nu(\mathbf{k}', \mathbf{k}) f_{\nu'}(\mathbf{k}') [1 - f_\nu(\mathbf{k})] - S_\nu^{\nu'}(\mathbf{k}, \mathbf{k}') f_\nu(\mathbf{k}) [1 - f_{\nu'}(\mathbf{k}')] \} \quad (4.34)$$

where ν is the subband index. The electron distribution is denoted by the function $f(\mathbf{x}, \mathbf{p}, t)$ from which the macroscopic quantities of interest can be evaluated. The last two terms on the left hand side (l.h.s) of equation (4.34) describe the net-in flow of electrons to an elementary volume centered at \mathbf{x} in position space and at \mathbf{p} in momentum space, respectively. The right hand side (r.h.s) represents the collision integral, where the transition rate $S(\mathbf{k}, \mathbf{k}')$ from an initial state $|\mathbf{k}\rangle$ to a final state $|\mathbf{k}'\rangle$ can be calculated according to the Fermis's Golden Rule [69]

$$S(\mathbf{k}, \mathbf{k}') = \frac{2\pi}{\hbar} |\langle \mathbf{k}' | H_{\text{int}} | \mathbf{k} \rangle|^2 \left(N_q + \frac{1}{2} \pm \frac{1}{2} \right) \delta(E(\mathbf{k}') - E(\mathbf{k}) \mp \hbar\omega) \quad (4.35)$$

where H_{int} denotes the interaction Hamiltonian. In principle, this is the same equation as (4.28) when considering the substitution $|\alpha, r\rangle \rightarrow |\mathbf{k}\rangle$. Due to the classical treatment of particles in the l.h.s of the BTE (4.34) and the quantum mechanical one on the r.h.s, the BTE constitutes a semiclassical description. Basically, the semiclassical characterization is based on the assumption that the de Broglie wavelength is significantly smaller than the spatial variation of the external potential. Furthermore, the time between collisions, which is in the range of sub-picoseconds, must be smaller than the time. The collisions are mutually independent and change the electron momentum instantaneously.

In the semiclassical model the transport is described via in- and out-scattering from stationary states that are solutions of the Schrödinger equation. Since the well and barrier structure are included in the Hamiltonian, tunneling is already considered through the eigenstates, and transport occurs via scattering between these states.

Figure 4.1 illustrates how tunneling between two quantum well states $|L\rangle$ and $|R\rangle$ is described by solving the coupled well system and obtaining a new set of delocalized states. The anticrossing gap Δ_0 is the minimum separation between the symmetric and anti-symmetric states. Using such delocalized states as basis functions, there is no interwell tunneling time, and intersubband scattering into and out of $|A\rangle$ and $|S\rangle$ from other subbands govern the transport through the barrier. It is shown that this picture is accurate for strong coupling, i.e. large Δ_0 [70].

Figure 4.2 shows the difference between the semiclassical and coherent picture of coupled quantum wells. In the semiclassical picture, the wave functions are delocalized at resonance and transport through the barrier happens when electrons enter the levels $|S\rangle$ or $|A\rangle$. In the coherent picture, the electrons are transported through the barrier with Rabi oscillations at frequency Ω .

4.2.1 Pauli Master Equation

When the electron dephasing length in the contacts $\lambda_\phi \sim \hbar v_{th} / \delta E_{th}$ is larger than the length of the device L , the electrons are considered to be "larger" than the device. Here, v_{th} and δE_{th} denote the thermal velocity of the wave packet and the energetic broadening, respectively. In this case, the contacts inject only diagonal elements of the density matrix

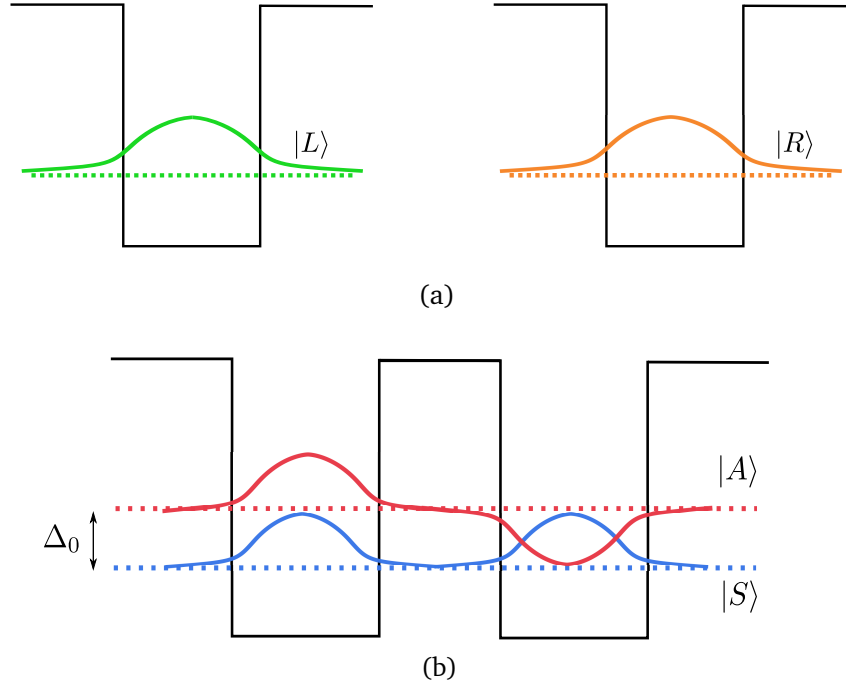


Figure 4.1: Anitcrossing between two single well states.

ρ . Following Van Hove's observation, the time needed to build the off-diagonal elements of ρ is much longer than the relaxation and transit times [71]. Off-diagonal terms in ρ are built up long after the electron has gone through the device. Thus, a master equation considering only diagonal elements of the density matrix is sufficient to describe electron transport in devices of size $L < \lambda_\phi$ [72]. In principle, this picture is equivalent to the Boltzmann description.

In open systems, the equation describing transport and relaxation phenomena can be written as [73]

$$\frac{d}{dt} f_{\mathbf{k}_{\parallel}\alpha} = \left(\frac{d}{dt} f_{\mathbf{k}_{\parallel}\alpha} \right)_{\text{scat}} + \left(\frac{d}{dt} f_{\mathbf{k}_{\parallel}\alpha} \right)_{\text{res}} \quad (4.36)$$

Here, $f_{\mathbf{k}_{\parallel}\alpha} = \rho_{\beta\beta}$, where \mathbf{k}_{\parallel} is the in-plane wave vector and $\alpha \equiv (\lambda, \nu, \eta)$ denotes the generic electron state in the multi quantum well structure, i.e. λ is the stage, ν represents the subband index and η stands for the valley index. Due to the smallness of the device and the assumption that the electrons are injected as delocalized objects, this approach is practically identical to the approach considered by Fischetti [74]. The second term on the r.h.s of equation (4.36) describes the open boundary conditions of the system. It accounts for the injection and loss contributions from and to external carrier reservoirs treated via a relaxation-time-like term of the form

$$\left(\frac{d}{dt} f_{\mathbf{k}_{\parallel}\alpha} \right)_{\text{res}} = \gamma_{\mathbf{k}_{\parallel}\alpha} (f_{\mathbf{k}_{\parallel}\alpha}^0 - f_{\mathbf{k}_{\parallel}\alpha}) \quad (4.37)$$

where $\gamma_{\mathbf{k}_{\parallel}\alpha}^{-1}$ is the device transit time of an electron and $f_{\mathbf{k}_{\parallel}\alpha}^0$ is assumed to be the quasi-equilibrium carrier distribution in the external reservoirs. This assumption is mainly

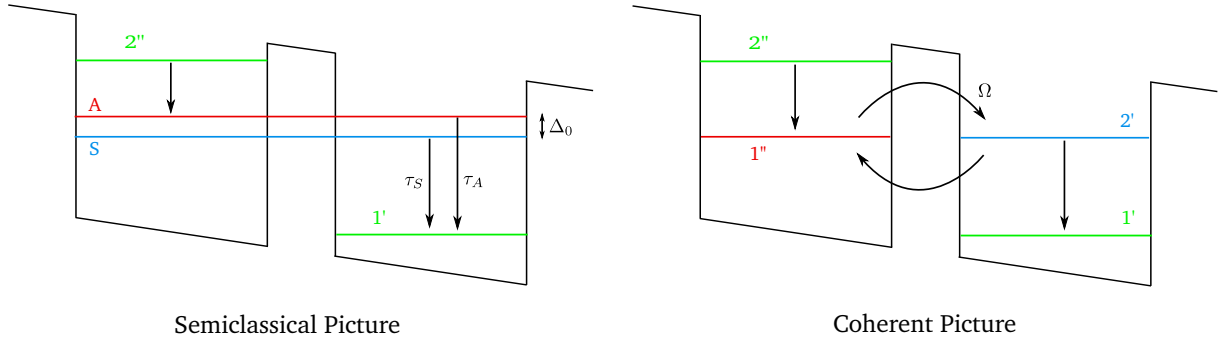


Figure 4.2: Difference between the semiclassical and coherent picture of coupled quantum wells.

based on the idea that the overall occupations of the "large" reservoirs of electrons are essentially unchanged by the addition or subtraction of a few electrons to or from the device region.

However, the reservoirs must inject and extract electrons [75]. In the course of solving the Schrödinger equation, a wave incident from outside the device is assumed which is partially reflected and transmitted. It is assumed that outside the device domain a wave is coming from $-\infty$ and is either transmitted to $+\infty$ or it is reflected by the potential and travels back to $-\infty$. The assumption that the wave function is continuous allows to specify the boundary conditions at the contacts. Introducing a reflexion coefficient R_α and transmission coefficient T_α , the total current flowing from the s th contact into other contacts can be written as [74]

$$J = \sum_{\alpha} \left[\gamma_{\mathbf{k}_{\parallel}\alpha}^{(s)} (f_{\mathbf{k}_{\parallel}\alpha}^{0,(s)} - R_{\alpha}^{(s)} f_{\mathbf{k}_{\parallel}\alpha}^{(s)}) - \sum_{r \neq s} \gamma_{\mathbf{k}_{\parallel}\alpha}^{(r)} T_{\alpha}^{(r)} f_{\mathbf{k}_{\parallel}\alpha}^{(r)} \right] \quad (4.38)$$

The first term on the r.h.s of equation (4.36) describes the scattering dynamics and is usually treated via collision operators. The master equation can be derived from the Liouville-von Neumann equation using a representation of eigenstates which diagonalize the external potential. The Markov approximation, which ensures the loss of memory effects [76], is the main assumption for the derivation. Fischetti uses additionally the Van Hove limit, which states that $\alpha_c^2 t$ is constant as $\alpha_c^2 \rightarrow 0$ and the time t tends to infinity, in order to derive the irreversible Pauli master equation and to ensure that the off-diagonal terms of the density matrix remain negligible.

Iotti and coworkers present a somewhat different derivation of the same master equation, calling it Boltzmann-like equation [77]. They also start from the Liouville-von Neumann equation approach and propose the Markov approximation within a fully non-diagonal density matrix treatment. By introducing a so-called diagonal approximation, the off-diagonal elements of the density matrix are neglected arriving finally at the Boltzmann-

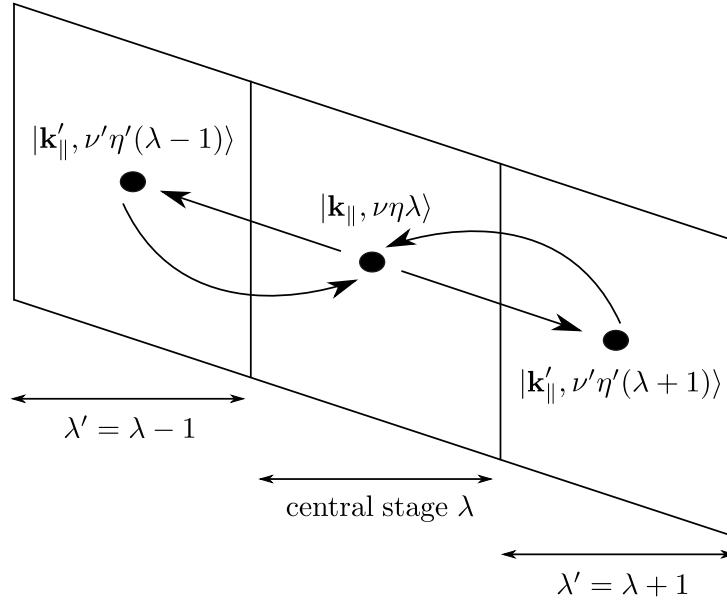


Figure 4.3: Schematic of three adjacent stages of a QCL under an applied field. Each time an electron in state $|\mathbf{k}_{\parallel}, \nu\eta\lambda\rangle$ undergoes an interstage scattering to a state $|\mathbf{k}'_{\parallel}, \nu'\eta'(\lambda \pm 1)\rangle$, the electron is reinjected into the central region and the corresponding electron charge contributes to the current.

like or Pauli Master equation

$$\frac{d}{dt}f_{\mathbf{k}_{\parallel}\alpha}(t) = \sum_{\mathbf{k}'_{\parallel}\alpha'} \{S_{\alpha'}^{\alpha}(\mathbf{k}'_{\parallel}, \mathbf{k}_{\parallel})f_{\mathbf{k}'_{\parallel}\alpha'}(t) - S_{\alpha}^{\alpha'}(\mathbf{k}_{\parallel}, \mathbf{k}'_{\parallel})f_{\mathbf{k}_{\parallel}\alpha}(t)\} \quad (4.39)$$

Due to the incoherent nature of the stationary charge transport in QCL heterostructures, the time evolution of the carrier distribution function is governed by the PME (4.39) [78]. Since no electric field is applied in the in-plane direction, the equation (4.39) does not have the in-plane drift and diffusion terms on the l.h.s like in the BTE (4.34). The electrons are not explicitly accelerated along the growth direction, rather the electronic states are affected through the change in the band profile which modifies the electron distribution. Due to scattering the electrons are hopping among the subbands.

Since the QCL structure is translationally invariant, the electron transport can be simulated over a generic central stage only. Due to the small wave function overlap between the central stage and the spatially remote stages, it can be assumed that the interstage scattering is limited only to the nearest neighbor. The electron states corresponding to a single QCL stage are evaluated within a selfconsistent Schrödinger-Poisson solver. Given such carrier states, we consider the multi quantum well structure as a repetition of this periodicity region, which ensures the validity of charge conservation.

The carrier transport is simulated over the central stage and every time a carrier proceeds an interstage scattering process, the electron is reinjected into the central region and the

corresponding electron charge contributes to the current. The current density across the device is given in terms of the net electron flux through the interface between the stages

$$J \propto \sum_{\mathbf{k}_{\parallel}\nu\eta} \sum_{\mathbf{k}'_{\parallel}\nu'\eta'} [S_{\lambda\nu\eta}^{(\lambda+1)\nu'\eta'}(\mathbf{k}_{\parallel}, \mathbf{k}'_{\parallel}) f_{\lambda\nu\eta}(\mathbf{k}_{\parallel}) - S_{\lambda\nu\eta}^{(\lambda-1)\nu'\eta'}(\mathbf{k}_{\parallel}, \mathbf{k}'_{\parallel}) f_{\lambda\nu\eta}(\mathbf{k}_{\parallel})] \quad (4.40)$$

In the Monte Carlo simulation, J is obtained by simply counting the interstage scattering events.

4.2.2 Monte Carlo Method

The ensemble Monte Carlo method is an efficient approach for solving the PME (4.39) and simulating electron transport in semiconductor devices in general [79]. It is based on calculating the motion of an ensemble of particles during a short time dt , where electrons are assumed to occupy a known energy state. Electrons can be subject to multiple scattering mechanisms such as electron-longitudinal optical (LO) phonon, acoustic, and optical deformation potential, and intervalley scattering. These scattering mechanisms are considered to be instantaneous and to satisfy transverse momentum conservation and total energy conservation.

Between two consecutive scattering events, which are chosen randomly under consideration of the probability of each scattering mechanism, the electron flies force-free in the in-plane direction and remains in a given subband.

At the end of each free flight a scattering mechanism is selected, where each electron has its own probability of scattering due to its energy and momentum. A scattering mechanism is selected by means of the function Λ_n defined as

$$\Lambda_n(\mathbf{k}_{\parallel}) = \frac{1}{\Gamma} \sum_{i=1}^n \frac{1}{\tau_i(\mathbf{k}_{\parallel})} \quad (4.41)$$

which are the successive summations of the scattering rates normalized with the total scattering rate Γ . By generating a random number r uniformly distributed in the range $[0, 1]$, the n -th scattering mechanism is chosen according to [80]

$$\Lambda_{n-1}(\mathbf{k}_{\parallel}) < r \leq \Lambda_n(\mathbf{k}_{\parallel}) \quad (4.42)$$

The input for the Monte Carlo transport kernel is provided by a selfconsistent Schrödinger-Poisson solver.

The calculation of the various scattering rates and the algorithm for the determination of the time evolution of the simulated particles are the two major parts of the Monte Carlo simulation. The electrons belonging to one stage are tracked during the simulation. After obtaining the wave functions belonging to the central stage and its neighboring stages, the scattering parameters are calculated. Reinjection of the electrons that scatter out of the central stage ensures the current continuity. Figure 4.4 illustrates the flow

chart of the Monte Carlo transport kernel, whose input is provided by the selfconsistent Schrödinger-Poisson solver.

The duration of the free flight τ is determined by random numbers, and the time interval dt is typically chosen to be a few femtoseconds. The number of simulated electrons N and the simulation time t_{total} are chosen to allow for reasonable and accurate calculation results, where $N = 10000$ and $t_{\text{total}} = 10\text{ps}$ are usually sufficient to obtain satisfactory results. Each particle is characterized by a subband index and its in-plane momentum, which are used to determine the available scattering processes. The electron distributions are initialized by randomly assigning the particles to the subbands.

In order to calculate the time evolution of the ensemble of particles, all particles are time-evolved in sequence. Due to the electron dynamics the time interval is chosen small enough (few femtoseconds). During every time step, the initial and the final subbands of the scattered particles are tracked. The current density is obtained from the recorded electron flux due to scattering from the central stage into the next stage or into the previous stage, counting the electrons scattering back as negative. The corresponding charge is weighted by the number of simulated particles. Each simulated particle represents an effective charge

$$q = e \frac{V}{N} \sum_i N_{D,i} \cdot d_i \quad (4.43)$$

where V is the volume of the device, and $N_{D,i}$ represents the donor concentration, and d_i is the thickness of the i -th layer.

In general, the ensemble average over the N electrons of the system defines the average value of a quantity \tilde{X} according to [81]

$$\langle \tilde{X} \rangle = \frac{1}{N} \sum_i \tilde{X}_i \quad (4.44)$$

This average value is compared to previous ones to determine convergence. The number of time steps needed to reach a steady state solution depends on the simulated structure. Usually, the required simulation time accounts for several picoseconds.

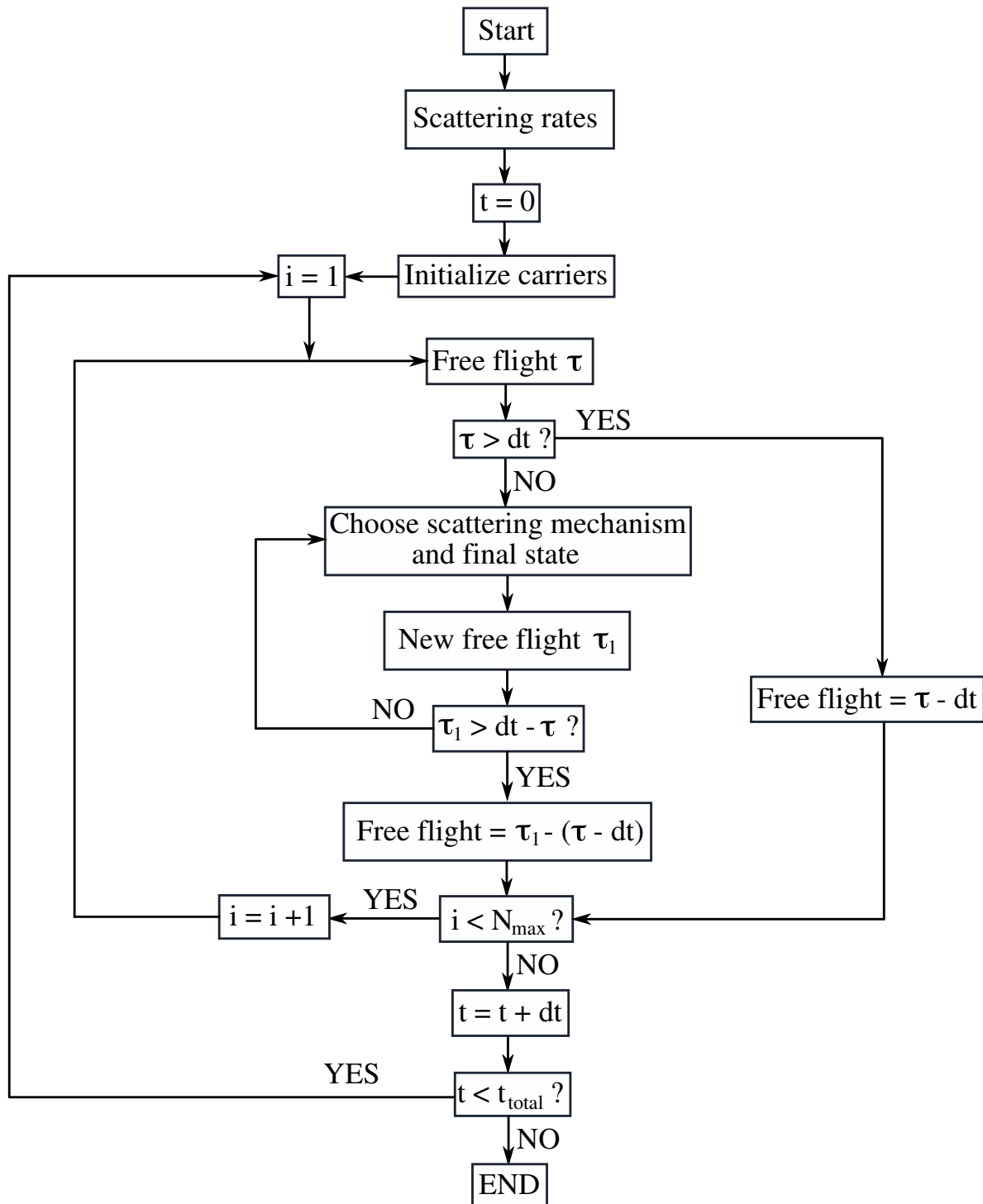


Figure 4.4: Flow chart of the ensemble Monte Carlo algorithm. The input is provided by a selfconsistent Schrödinger-Poisson solver.

Chapter 5

Scattering Rates

In order to provide population inversion in QCLs, the scattering rates have to be engineered properly by designing the energy levels and wave functions. The scattering events interrupt the kinetics of electrons. Between the scattering events the acceleration is governed by the external fields. Due to scattering, electrons dissipate their momentum and energy and can change the subband. Scattering processes are determined in terms of transition probabilities $S_{\alpha\alpha'}$ between an initial state $|\alpha\rangle$ and a final state $|\alpha'\rangle$ per unit time. Various scattering mechanisms exist. In this chapter we will consider and discuss scattering due to lattice vibrations as well as interface roughness. More detailed derivations can be found in Appendix B.

5.1 Phonons

In second quantization, the vibrations are treated as quasi particles which are the phonons with an energy $E = \hbar\omega_q$ and a momentum $\mathbf{p} = \hbar\mathbf{q}$. In the course of an interaction between an electron with energy E and a phonon with energy $\hbar\omega_q$, the electron either emits or absorbs a phonon and the final electron energy is given by $E' = E \pm \hbar\omega_q$. In heterostructures the two dimensional wave vectors are conserved according to

$$\mathbf{k}'_{\parallel} = \mathbf{k}_{\parallel} + \mathbf{q}_{\parallel}$$

where \mathbf{k}_{\parallel} and \mathbf{k}'_{\parallel} are the in-plane wave vectors of the electron before and after the electron-phonon collision. The energy and momentum conservation reveals the particle nature of the phonons.

A distinction is drawn between acoustic and optical phonons. Acoustic phonons correspond to sound waves in a crystal lattice. Here, all atoms belonging to a basis system move in phase and the acoustic phonons have frequencies that become small at the long wavelengths [82]. In the case of optical phonons, the atoms belonging to a basis system

move out of phase and the oscillation frequencies are in the range of infrared and the visible spectrum. Optical phonons always have some minimum frequency of vibration, independent from the largeness of the wavelength.

In thermal equilibrium, the average number of phonons N_q is given by the Bose-Einstein distribution

$$N_q = \frac{1}{\exp\left(\frac{\hbar\omega_q}{k_B T}\right) - 1} \quad (5.1)$$

5.2 From Fermi's Golden Rule to the Total Scattering Rate

Fermi's Golden Rule is a method to calculate the transition rate from an initial state $|\alpha, \mathbf{k}_{\parallel}\rangle$ to a final state $|\alpha', \mathbf{k}'_{\parallel}\rangle$ due to a perturbation. As described in the section 4.1.1.2, the general form of the transition probability is given by

$$S_{\alpha}^{\alpha'}(\mathbf{k}_{\parallel}, \mathbf{k}'_{\parallel}) = \frac{2\pi}{\hbar} \sum_{\mathbf{q}} |\langle \alpha', \mathbf{k}'_{\parallel} | \langle n'_{\mathbf{q}} | \hat{H}_{\text{int}} | n_{\mathbf{q}} \rangle | \alpha, \mathbf{k}_{\parallel} \rangle|^2 \delta(E_{\alpha}(\mathbf{k}_{\parallel}) - E_{\alpha'}(\mathbf{k}'_{\parallel}) \pm \hbar\omega) \quad (5.2)$$

The energy exchange between the electrons and the lattice occurs via phonons and the Delta distribution ensures energy conservation. Here, $\hbar\omega$ is the energy of the absorbed or emitted phonons. For the phonon interaction, the perturbation potential can be written in the following form

$$\hat{H}_{\text{int}} = \hat{U}_{\mathbf{q}} e^{i(\mathbf{q}\cdot\mathbf{x} - \omega_{\mathbf{q}}t)} \quad (5.3)$$

Inserting the wave function (3.1) into the matrix element appearing in Fermi's Golden Rule, gives

$$\begin{aligned} |\langle \alpha', \mathbf{k}'_{\parallel} | \hat{H}_{\text{int}} | \alpha, \mathbf{k}_{\parallel} \rangle| &= \int_V \frac{1}{A} \Phi_{\alpha'}^*(z) |\langle n'_{\mathbf{q}} | \hat{H}_{\text{int}} | n_{\mathbf{q}} \rangle| \Phi_{\alpha}(z) e^{i(\mathbf{k}_{\parallel} - \mathbf{k}'_{\parallel})\cdot\mathbf{x}} d\mathbf{x} \\ &= \int dz \int d\mathbf{x}_{\parallel} \Phi_{\alpha'}^*(z) \Phi_{\alpha}(z) e^{iq_z z} |U_{\mathbf{q}}| \frac{1}{A} e^{i(\mathbf{k}_{\parallel} - \mathbf{k}'_{\parallel} + \mathbf{q}_{\parallel})\cdot\mathbf{x}} \\ &= |U_{\mathbf{q}}| F_{\alpha'}^{\alpha}(q_z) \delta_{\mathbf{k}_{\parallel} + \mathbf{q}_{\parallel}, \mathbf{k}'_{\parallel}} \end{aligned} \quad (5.4)$$

where $U_{\mathbf{q}} = \langle n'_{\mathbf{q}} | \hat{U}_{\mathbf{q}} | n_{\mathbf{q}} \rangle$ and the form factor is given by

$$F_{\alpha'}^{\alpha}(q_z) = \int \Phi_{\alpha'}^*(z) \Phi_{\alpha}(z) e^{iq_z z} dz \quad (5.5)$$

In equation (5.2), the summation over \mathbf{q} can be split into a sum over q_z and another sum over \mathbf{q}_{\parallel} . Due to the momentum conservation, the sum over \mathbf{q}_{\parallel} gives only one term for $\mathbf{q}_{\parallel} = \mathbf{k}'_{\parallel} - \mathbf{k}_{\parallel}$. The remaining summation in the z direction can be transformed to an integration over q_z according to

$$\sum_{q_z} \rightarrow \frac{L_z}{2\pi} \int dq_z$$

Thus, Fermi's Golden Rule can be written as

$$S_{\alpha}^{\alpha'}(\mathbf{k}_{\parallel}, \mathbf{k}'_{\parallel}) = \frac{L_z}{\hbar} \int |U_{\mathbf{k}'_{\parallel} - \mathbf{k}_{\parallel}, q_z}|^2 |F_{\alpha'}^{\alpha}(q_z)|^2 \delta(E_{\alpha}(\mathbf{k}_{\parallel}) - E_{\alpha'}(\mathbf{k}'_{\parallel}) \pm \hbar\omega) dq_z \quad (5.6)$$

Finally, the total scattering rate can be calculated as follows

$$\begin{aligned} \frac{1}{\tau_{\alpha}^{\alpha'}(\mathbf{k}_{\parallel})} &= \frac{A}{(2\pi)^2} \int S_{\alpha}^{\alpha'}(\mathbf{k}_{\parallel}, \mathbf{k}'_{\parallel}) d\mathbf{k}'_{\parallel} \\ &= \frac{V}{(2\pi)^2 \hbar} \int d\mathbf{k}'_{\parallel} \int dq_z |U_{\mathbf{k}'_{\parallel} - \mathbf{k}_{\parallel}, q_z}|^2 |F_{\alpha'}^{\alpha}(q_z)|^2 \delta(E_{\alpha}(\mathbf{k}_{\parallel}) - E_{\alpha'}(\mathbf{k}'_{\parallel}) \pm \hbar\omega) \end{aligned} \quad (5.7)$$

5.3 Polar Optical Phonon Scattering

In polar semiconductors the electron-longitudinal optical (LO) phonon scattering is the dominant intersubband scattering mechanism for separations of the subbands less than the LO phonon energy [83]. Due to the polarization in polar semiconductor crystals induced by the optical vibration mode, the electrons are scattered through the interaction of the Coulomb field of the lattice polarization waves.

In optical vibrations the atoms in a lattice vibrate against each other, which can produce polarization effects. For longitudinal optical vibrations there is an restoring force due to the polarization field generated by the vibration. The lattice polarization \mathbf{P}_{Lat} is proportional to the lattice displacement \mathbf{U} and the Fröhlich constant F_c

$$\mathbf{P}_{\text{Lat}} = F_c \hat{\mathbf{U}} \quad (5.8)$$

where F_c is given by [84]

$$F_c = \left[\frac{\hbar\omega_{LO}}{2} \epsilon_0^2 \left(\frac{1}{\epsilon_{\infty}} - \frac{1}{\epsilon_s} \right) \right]^{1/2} \quad (5.9)$$

Here, ϵ_0 is the vacuum dielectric constant, ϵ_s and ϵ_{∞} are the static dielectric permittivity and high frequency dielectric permittivity.

An electric displacement \mathbf{D} is generated by the charge distribution according to

$$\nabla \cdot \mathbf{D} = \rho(\mathbf{x}) \quad (5.10)$$

The interaction potential $\Delta\hat{U}$ between the external electric displacement and the lattice polarization reads

$$\Delta\hat{U} = -\frac{F_c}{\epsilon_0} \hat{\mathbf{U}} \cdot \mathbf{D} \quad (5.11)$$

with

$$\hat{\mathbf{U}} = \frac{1}{\sqrt{V}} \sum_{\mathbf{q}} \mathbf{q} [\hat{a}_{\mathbf{q}} e^{i\mathbf{q} \cdot \mathbf{x}} + \hat{a}_{\mathbf{q}}^{\dagger} e^{-i\mathbf{q} \cdot \mathbf{x}}] \quad (5.12)$$

where \hat{a}_q and \hat{a}_q^\dagger denote the annihilation and creation operators. The summation over all generated dipoles result in the total interaction Hamiltonian, hence

$$\hat{H}_{\text{e-ph}}^{\text{LO}} = \int \Delta \hat{U} d\mathbf{x} \quad (5.13)$$

An electron located at \mathbf{x} generates a displacement at \mathbf{x}' according to

$$\mathbf{D}(\mathbf{x}') = -\frac{e}{4\pi} \frac{\mathbf{x}' - \mathbf{x}}{|\mathbf{x}' - \mathbf{x}|^3} \quad (5.14)$$

which yields an interaction Hamiltonian of the form

$$\hat{H}_{\text{e-ph}}^{\text{LO}} = \sum_{\mathbf{q}} (\alpha_{\text{LO}} \hat{a}_q e^{i\mathbf{q}\cdot\mathbf{x}} + \alpha_{\text{LO}}^* \hat{a}_q^\dagger e^{-i\mathbf{q}\cdot\mathbf{x}}) \quad (5.15)$$

where the coupling coefficient is given by

$$\alpha_{\text{LO}} = -i \frac{e}{q} \left(\frac{\hbar\omega_{\text{LO}}}{2V} (\varepsilon_\infty^{-1} - \varepsilon_s^{-1}) \right)^{1/2} \quad (5.16)$$

The scattering rate for an electron initially in subband ν and stage λ to a final subband ν' and stage λ' , can be written as (see Appendix B.1)

$$\begin{aligned} \frac{1}{\tau_{\nu\lambda}^{\nu'\lambda'}(\mathbf{k}_\parallel)} &= \frac{e^2 \hbar\omega_{\text{LO}} m_{\nu\lambda}^*}{4\hbar^3} \left(\frac{1}{\varepsilon_\infty} - \frac{1}{\varepsilon_s} \right) \left(N_{\text{LO}} + \frac{1}{2} \mp \frac{1}{2} \right) \Theta(E_{\nu\lambda}^\eta(\mathbf{k}) - E_{\nu'\lambda'}^{\eta'} \pm \hbar\omega_{\text{LO}} + \Delta_{\lambda\lambda'}) \\ &\times \int dq_z \frac{|F_{\nu'\lambda'}^{\nu\lambda}(q_z)|^2}{q_z^4 + (Q_{\nu\lambda}^{\nu'\lambda'})_\pm^4 + 2q_z^2 [2k_\parallel^2 \pm (Q_{\nu\lambda}^{\nu'\lambda'})_\pm^2]} \end{aligned} \quad (5.17)$$

where m^* is the electron effective mass, $\hbar\omega_{\text{LO}}$ is the longitudinal optical phonon energy. Here, $\Delta_{\lambda\lambda'}$ denotes the energy change due to reinjection of the electron into the central region after an interstage scattering process

$$\Delta_{\lambda\lambda'} = eFL(\delta_{\lambda',\lambda+1} - \delta_{\lambda',\lambda-1}) \quad (5.18)$$

5.4 Acoustic Deformation Potential Scattering

In this section, the coupling of the electrons with acoustic phonons is analyzed. Displacement of the atoms from their lattice sites are induced by crystal vibrations, which induces a modification of the bandstructure. For electrons in the conduction band, the variation of the conduction band edge E_c can be induced by acoustic phonons and the corresponding interaction Hamiltonian $\hat{H}_{\text{e-ph}}^{\text{AC}}$ is given by

$$\hat{H}_{\text{e-ph}}^{\text{AC}} = \delta E_c \quad (5.19)$$

For small displacements δE_c can be written as

$$\delta E_c = \Xi_{ac} \frac{\delta V}{V} \quad (5.20)$$

where Ξ_{ac} denotes the acoustic deformation potential and δV is the variation of the crystal volume V . The local variation of the volume results from the lattice displacement $\mathbf{U} = \mathbf{x}' - \mathbf{x}$. The volume of a cube generated by the orthogonal vectors $\mathbf{a} = (\delta x, 0, 0)$, $\mathbf{b} = (0, \delta y, 0)$ and $\mathbf{c} = (0, 0, \delta z)$, is given by

$$V = \mathbf{a} \cdot (\mathbf{b} \times \mathbf{c}) = \delta x \delta y \delta z \quad (5.21)$$

The cube is distorted according to the transformations

$$\mathbf{a}' = \begin{pmatrix} \delta x + \frac{\partial U_x}{\partial x} \delta x \\ \frac{\partial U_y}{\partial x} \delta x \\ \frac{\partial U_z}{\partial x} \delta x \end{pmatrix}, \quad \mathbf{b}' = \begin{pmatrix} \frac{\partial U_x}{\partial y} \delta y \\ \delta y + \frac{\partial U_y}{\partial y} \delta y \\ \frac{\partial U_z}{\partial y} \delta y \end{pmatrix}, \quad \mathbf{c}' = \begin{pmatrix} \frac{\partial U_x}{\partial z} \delta z \\ \frac{\partial U_y}{\partial z} \delta z \\ \delta z + \frac{\partial U_z}{\partial z} \delta z \end{pmatrix}$$

and the new volume can be written as

$$V' = \mathbf{a}' \cdot (\mathbf{b}' \times \mathbf{c}') = \delta x \delta y \delta z \left(1 + \frac{\partial U_x}{\partial x} + \frac{\partial U_y}{\partial y} + \frac{\partial U_z}{\partial z} + \dots \right) \quad (5.22)$$

Since

$$\frac{\delta V}{V} = \frac{V' - V}{V} = \frac{\partial U_x}{\partial x} + \frac{\partial U_y}{\partial y} + \frac{\partial U_z}{\partial z} = \nabla \cdot \mathbf{U}, \quad (5.23)$$

where the lattice displacement is given by [85]

$$\hat{\mathbf{U}} = \frac{1}{\sqrt{V}} \sum_{\mathbf{q}} \mathbf{w}_q \left(\frac{\hbar}{2\rho\omega_q} \right)^{1/2} (\hat{a}_q e^{i\mathbf{q}\cdot\mathbf{x}} + \hat{a}_q^\dagger e^{-i\mathbf{q}\cdot\mathbf{x}}), \quad (5.24)$$

the interaction Hamiltonian reads

$$\begin{aligned} \hat{H}_{e\text{-ph}}^{\text{AC}} &= \Xi_{ac} \nabla \cdot \hat{\mathbf{U}} \\ &= \sum_{\mathbf{q}} (\alpha_{\text{AC}} \hat{a}_q e^{i\mathbf{q}\cdot\mathbf{x}} + \alpha_{\text{AC}}^* \hat{a}_q^\dagger e^{-i\mathbf{q}\cdot\mathbf{x}}). \end{aligned} \quad (5.25)$$

Here, ρ is the mass density of the semiconductor, and \mathbf{w}_q denotes the polarization vector. The coupling coefficient can be written as [86]

$$\alpha_{\text{AC}} = i\mathbf{w} \cdot \mathbf{q} \left(\frac{\hbar \Xi_{ac}^2}{2V\rho\omega_q} \right)^{1/2} \quad (5.26)$$

The electron scattering rate with the assistance of acoustic phonons can be written in the following form [87] (see Appendix B.2)

$$\frac{1}{\tau_{\nu\lambda}^{\nu'\lambda'}(\mathbf{k}_{\parallel})} = \frac{\Xi_{ac}^2 m_{\nu'\lambda'}^* k_B T}{\rho \hbar^3 v_s^2} I_{\nu\lambda}^{\nu'\lambda'} \Theta(E_{\nu\lambda}(\mathbf{k}_{\parallel}) - E_{\nu'\lambda'} + \Delta_{\lambda\lambda'}) \quad (5.27)$$

where E_{ac} is the acoustic deformation potential, ρ is the density of the material, and v_s stands for the sound velocity. This equation is only valid for $\hbar\omega_q \ll k_B T$, i.e. when the thermal energy is much larger than the energy of the phonon involved in the transition, and in the elastic approximation limit $\hbar\omega_q \rightarrow 0$ (see Appendix B.2).

5.5 Optical Deformation Potential Scattering

In contrast to the case of acoustic vibrations where the perturbation Hamiltonian is proportional to the derivative of the atomic displacement, the perturbation Hamiltonian for the optical modes is assumed to be proportional to the atomic displacement. Due to the quite flat dispersion curve, the energy associated with optical phonons is assumed to be constant. In this case, the phonon occupation number N_{op} is independent on the phonon wave vector. Since the scattering arises from the band edge variation induced by optical phonons, we can rely on the considerations done for deformation potential scattering for acoustic phonons. Assuming an isotropic deformation potential, the coupling coefficient of its interaction potential can be written as

$$\alpha_{\text{OP}} = \left(\frac{\hbar \Xi_{\text{op}}^2}{2V \rho \omega_{\text{op}}} \right)^{1/2} \quad (5.28)$$

The scattering rate caused by optical phonons is given by (see Appendix B.3)

$$\frac{1}{\tau_{\nu\lambda}^{\nu'\lambda'}(\mathbf{k}_{\parallel})} = \frac{\Xi_{\text{op}}^2 m_{\nu'\lambda'}^*}{2\rho \hbar^2 \omega_{\text{op}}} I_{\nu\lambda}^{\nu'\lambda'} \left(N_{\text{op}} + \frac{1}{2} \mp \frac{1}{2} \right) \Theta(E_{\nu\lambda}(\mathbf{k}_{\parallel}) - E_{\nu'\lambda'} \pm \hbar\omega_{\text{op}} + \Delta_{\lambda\lambda'}) \quad (5.29)$$

5.6 Intervalley Scattering

Formally, the intervalley scattering is treated in the same way as the scattering due to optical phonons with a deformation potential. It has been shown that the phonon assisted intervalley scattering can be modeled by means of an intervalley deformation potential [88].

$$\frac{1}{\tau_{\nu\lambda\eta}^{\nu'\lambda'\eta'}} = \frac{Z_{\eta'} D_{\eta\eta'}^2 m_{\nu'\lambda'}^{\eta'*}}{2\hbar\rho E_{\eta\eta'}} \left(N_{\eta\eta'} + \frac{1}{2} \mp \frac{1}{2} \right) I_{\nu\lambda\eta}^{\nu'\lambda'\eta'} \Theta(E_{\nu\lambda}^{\eta}(\mathbf{k}_{\parallel}) - E_{\nu'\lambda'}^{\eta'} \pm E_{\eta\eta'} + \Delta_{\lambda\lambda'}) \quad (5.30)$$

where η and η' denote the initial and the final valley index, respectively. $D_{\eta\eta'}$ is the intervalley deformation potential constant, ρ is the mass density, $E_{\eta\eta'}$ is the intervalley phonon energy, and $Z_{\eta'}$ denotes the degeneracy of the final valley. The overlap integral is determined by

$$I_{\nu\lambda\eta}^{\nu'\lambda'\eta'} = \int |\Phi_{\nu\lambda}^{\eta}(z)|^2 |\Phi_{\nu'\lambda'}^{\eta'}(z)|^2 dz \quad (5.31)$$

5.7 Interface Roughness Scattering

The roughness of interfaces in a heterostructure leads to spatial fluctuations of the well width, and consequently to fluctuations of the energy levels. These fluctuations of the

energy levels act as a fluctuating potential for the motion of confined carriers [89]. A distribution of terraces is present at the interfaces and the electrons are scattered elastically by them [90].

The randomness of the interface is described by a correlation function at the in-plane position $\mathbf{x}_{\parallel} = (x, y)$, which is usually taken to be Gaussian with a characteristic height of the roughness Δ , and a correlation length Λ representing a length scale for fluctuations of the roughness along the interface [91], such that

$$\langle \Delta(\mathbf{x}_{\parallel}) \Delta(\mathbf{x}'_{\parallel}) \rangle = \Delta^2 e^{-|\mathbf{x}_{\parallel} - \mathbf{x}'_{\parallel}|^2 / \Lambda^2} \quad (5.32)$$

The perturbation in the potential $V(z)$ due to a position shift $\Delta(\mathbf{x}_{\parallel})$ is given by

$$\delta V = V[z - \Delta(\mathbf{x}_{\parallel})] - V(z) \approx -\Delta(\mathbf{x}_{\parallel}) \frac{dV(z)}{dz} \quad (5.33)$$

For the I -th interface, which is centered about the plane z_I and extends over the range $[z_{L,I}, z_{R,I}]$, the scattering matrix element can be defined as

$$\begin{aligned} \langle \alpha', \mathbf{k}'_{\parallel} | V_{\text{IR}} | \alpha, \mathbf{k}_{\parallel} \rangle &= \left\langle \alpha', \mathbf{k}'_{\parallel} \left| \delta V \text{rect} \left(\frac{z - z_I}{z_{R,I} - z_{L,I}} \right) \right| \alpha, \mathbf{k}_{\parallel} \right\rangle \\ &= \frac{\varphi_{\alpha'\alpha, I}^2}{A} \int \Delta(\mathbf{x}_{\parallel}) e^{i(\mathbf{k}_{\parallel} - \mathbf{k}'_{\parallel}) \cdot \mathbf{x}_{\parallel}} d\mathbf{x}_{\parallel} \end{aligned} \quad (5.34)$$

where $|\alpha'\rangle$ and $|\alpha\rangle$ denote the final and initial wave functions, respectively. Here, $\varphi_{\alpha'\alpha, I}$ is defined as

$$\varphi_{\alpha'\alpha, I} = \int \Phi_{\alpha'}^*(z) \frac{dV}{dz} \text{rect} \left(\frac{z - z_I}{z_{R,I} - z_{L,I}} \right) \Phi_{\alpha}(z) dz \quad (5.35)$$

and the rectangular function reads

$$\text{rect}(z) = \begin{cases} 1, & |z| \leq 0.5 \\ 0, & |z| > 0.5 \end{cases}$$

The expectation value of the square of the matrix element is given by

$$\langle |\langle \alpha', \mathbf{k}'_{\parallel} | V_{\text{IR}} | \alpha, \mathbf{k}_{\parallel} \rangle|^2 \rangle = \frac{\varphi_{\alpha'\alpha, I}^2}{A^2} \iint \langle \Delta(\mathbf{x}'_{\parallel}) \Delta(\mathbf{x}_{\parallel}) \rangle e^{i(\mathbf{k}_{\parallel} - \mathbf{k}'_{\parallel}) \cdot (\mathbf{x}_{\parallel} - \mathbf{x}'_{\parallel})} d\mathbf{x}'_{\parallel} d\mathbf{x}_{\parallel} \quad (5.36)$$

Making use of eq. (5.32) and Fermi's Golden Rule, the interface roughness induced scattering rates are given by [92]

$$\begin{aligned} \frac{1}{\tau_{\alpha}^{\alpha'}(\mathbf{k}_{\parallel})} &= \frac{\pi \Delta^2 \Lambda^2}{\hbar} \sum_I |\varphi_{\alpha'\alpha, I}|^2 \int_0^{\pi} d\theta \int dk'_{\parallel} k'_{\parallel} e^{-(\mathbf{k}'_{\parallel} - \mathbf{k}_{\parallel})^2 \Lambda^2 / 4} \delta(E_{\alpha'}(\mathbf{k}'_{\parallel}) - E_{\alpha}(\mathbf{k}_{\parallel})) \\ &= \frac{2\pi^2 \Delta^2 \Lambda^2 m^*}{\hbar^3} \left[e^{-k_{\parallel}^2} + e^{-\frac{2m^*}{\hbar^2}(E_{\alpha}(k_{\parallel}) - E_{\alpha'})} + \frac{1}{2\pi} \int_0^{\pi} e^{\sqrt{\frac{8m^*}{\hbar^2}(E_{\alpha}(k_{\parallel}) - E_{\alpha'})} k_{\parallel} \cos \theta} d\theta \right] \\ &\quad \times \Theta(E_{\alpha}(\mathbf{k}_{\parallel}) - E_{\alpha'}) \end{aligned} \quad (5.37)$$

where \mathbf{k}'_{\parallel} and \mathbf{k}_{\parallel} are the final and initial wave vectors, respectively, and θ is the scattering angle. The integral is evaluated numerically by means of the MATLAB integration routines.

5.8 Alloy Scattering

We consider an alloy $A_xB_{1-x}C$, where the atoms A and B are distributed randomly and the crystal potential $V(\mathbf{x}_{\parallel})$ is not periodic. In general, the crystal potential of an alloy can be represented in terms of an average potential $\bar{V}(\mathbf{x}_{\parallel})$, which is periodic, plus a fluctuating potential $\delta V(\mathbf{x}_{\parallel})$ which describes the local departure of the actual alloy potential $V(\mathbf{x}_{\parallel})$ from the average potential $\bar{V}(\mathbf{x}_{\parallel})$. An effective scattering process (alloy scattering) is introduced by this fluctuating potential $\delta V(\mathbf{x}_{\parallel})$.

Here, we will introduce the most important expressions and identities for the mentioned potentials, and the detailed derivation of the alloy scattering rate can be looked up in Appendix B.6. The crystal potential for the alloy $A_xB_{1-x}C$ is the superposition of the potential contributed by the atoms A, B and C, which can be written as [93]

$$V(\mathbf{x}_{\parallel}) = \sum_{\mathbf{X}_A} V_A(\mathbf{x}_{\parallel} - \mathbf{X}_A) + \sum_{\mathbf{X}_B} V_B(\mathbf{x}_{\parallel} - \mathbf{X}_B) + \sum_{\mathbf{X}_C} V_C(\mathbf{x}_{\parallel} - \mathbf{X}_C) \quad (5.38)$$

By introducing the mathematical identities

$$\begin{aligned} V_A(\mathbf{x}_{\parallel} - \mathbf{X}_A) &= xV_A(\mathbf{x}_{\parallel} - \mathbf{X}_A) + (1-x)V_B(\mathbf{x}_{\parallel} - \mathbf{X}_A) + (1-x)V_A(\mathbf{x}_{\parallel} - \mathbf{X}_A) \\ &\quad - (1-x)V_B(\mathbf{x}_{\parallel} - \mathbf{X}_A) \\ V_B(\mathbf{x}_{\parallel} - \mathbf{X}_B) &= xV_A(\mathbf{x}_{\parallel} - \mathbf{X}_B) + (1-x)V_B(\mathbf{x}_{\parallel} - \mathbf{X}_B) - xV_A(\mathbf{x}_{\parallel} - \mathbf{X}_B) \\ &\quad + xV_B(\mathbf{x}_{\parallel} - \mathbf{X}_B) \end{aligned}$$

the crystal potential is given by

$$V(\mathbf{x}_{\parallel}) = \bar{V}(\mathbf{x}_{\parallel}) + \delta V(\mathbf{x}_{\parallel}) \quad (5.39)$$

where the average lattice potential $\bar{V}(\mathbf{x}_{\parallel})$ can be written as

$$\bar{V}(\mathbf{x}_{\parallel}) = \sum_{\mathbf{X}_i=\{\mathbf{X}_A, \mathbf{X}_B\}} xV_A(\mathbf{x}_{\parallel} - \mathbf{X}_i) + (1-x)V_B(\mathbf{x}_{\parallel} - \mathbf{X}_i) + \sum_{\mathbf{X}_C} V_C(\mathbf{x}_{\parallel} - \mathbf{X}_C) \quad (5.40)$$

and the fluctuating potential $\delta V(\mathbf{x}_{\parallel})$ reads

$$\delta V(\mathbf{x}_{\parallel}) = \sum_{\mathbf{X}_A} (1-x)[V_A(\mathbf{x}_{\parallel} - \mathbf{X}_A) - V_B(\mathbf{x}_{\parallel} - \mathbf{X}_A)] + \sum_{\mathbf{X}_B} x[V_B(\mathbf{x}_{\parallel} - \mathbf{X}_B) - V_A(\mathbf{x}_{\parallel} - \mathbf{X}_B)] \quad (5.41)$$

The alloy scattering rate can be expressed as [94]

$$\frac{1}{\tau_{\alpha}^{\alpha'}} = \frac{2m^*}{\hbar^3} \Omega_0 \Delta V_{AB}^2 x(1-x) \int \Phi_{\alpha'}^*(z) \Phi_{\alpha}(z) dz \quad (5.42)$$

In heterostructures, the alloy scattering rate is found to be independent of the electron kinetic energy. The volume of the elementary cell is given as $\Omega_0 = a_0^2/4$.

Chapter 6

Simulation Results

In this chapter the simulation results are presented. In section 6.1 results from calculations using Robin boundary conditions are demonstrated and discussed. Especially, the tunneling current and the optical gain are analyzed. Section 6.2 contains the results of the Monte Carlo simulations, where special focus is put on the role of interface roughness and intervalley scattering.

6.1 Quantum Ballistic Transport Calculations

Throughout this section we consider GaAs wells and barriers composed of $\text{Al}_x\text{Ga}_{1-x}\text{As}$.

6.1.1 Tunneling Current Density

On the basis of the Robin boundary conditions (3.19) and (3.20) the current density is numerically evaluated for periodic QCL structures as well for quasi-periodic systems. The transport of charge through the structure arises as a property of the wave function, and the current density is expressed as [1]

$$J_{(z)} = -\frac{2e}{A} \sum_{\alpha, k_{\parallel}} f_{\alpha}(k_{\parallel}) \text{Re} \left[\Phi_{\alpha}^*(z) \frac{i\hbar}{m^*(z)} \frac{\partial}{\partial z} \Phi_{\alpha}(z) \right] \quad (6.1)$$

where A is the cross-sectional area of the quantum well structure. The work of P. Harrison [95] suggests that the electron distributions in both the active region and the injector subbands are thermalized and thus the energy distribution of electrons in each subband can be approximated by a Fermi-Dirac distribution function

$$f_{\alpha}(k_{\parallel}) = \frac{1}{1 + \exp \left(\frac{E_{\alpha}(k_{\parallel}) - E_{F,\alpha}}{k_B T} \right)} \quad (6.2)$$

where $E_{F,\alpha}$ is the quasi Fermi energy of the α -th subband and $E_\alpha(k_{\parallel}) = E_\alpha + \hbar^2 k_{\parallel}^2 / 2m^*$.

The electron states are evaluated using a selfconsistent Schrödinger-Poisson solver, where the electron concentration is related to the electronic wave functions and the electron sheet densities in the corresponding subbands which can be calculated according to the Fermi-Dirac distribution. For a given total sheet density the quasi Fermi level is obtained iteratively, where the initial value of the quasi Fermi level is taken to be [96]

$$E_{F,\alpha}(T) = E_c(T) - \frac{E_g(T)}{2}$$

while the band gap in eV is

$$E_g(T) = E_g(0) - 5.41 \left[\frac{T^2}{(T + 204)} 10^{-4} \right]$$

with

$$E_g(0) = 1.519 + 1.155x + 0.37x^2$$

The conduction band edge is given by

$$\begin{aligned} E_c(T) &= E_g(T) \quad \text{for } 0 \leq x < 0.45 \\ E_c(T) &= E_X(T) \quad \text{for } 0x > 0.45 \end{aligned}$$

where

$$E_X(T) = E_X(0) - 4.6 \left[\frac{T^2}{(T + 204)} 10^{-4} \right]$$

with

$$E_X(0) = 1.981 + 0.124x + 0.144x^2$$

6.1.1.1 Comparison with the Tsu-Esaki Model

The Tsu-Esaki Model describes the tunneling current density. The corresponding formula is usually written as an integral over the product of two independent parts which only depend on the energy component perpendicular to the interface [97].

$$J = \frac{4\pi m^* e}{h^3} \int_{E_{\min}}^{E_{\max}} T_c(E) N(E) dE \quad (6.3)$$

$T_c(E)$ is the transmission coefficient which characterizes the penetrability of the considered energy barrier. The supply function $N(E)$ describes the supply of carriers for tunneling.

Figure 6.2 compares the simulated current density using the Robin boundary condition approach with the current density calculated by the Tsu-Esaki model for a GaAs/Al_{0.3}Ga_{0.7}As Fibonacci superlattice (FSL) [98] which is a quasi-periodic multibarrier system. The generalized FSL is generated by an iterative process according to the Fibonacci sequence [99]

$$S_1 = \{A\} \quad S_2 = \{B\} \quad \dots \quad S_n = S_{n-1}S_{n-2}$$

where A and B are the blocks of the well and barrier. A special kind of FSLs with a higher quasi-periodicity follows the iteration rule [100]

$$S'_n = (2S_{n-1})S_{n-2}$$

Table 6.1 presents a few initial generations of FSLs of the two different kinds.

The FSL type considered is S'_5 which has the sequence BBABBABBBABBABBBA, where A and B are the elementary blocks corresponding to the GaAs quantum well and the $\text{Al}_{0.3}\text{Ga}_{0.7}\text{As}$ barrier, respectively. The width of the well block is taken to be 5 unit cells of GaAs monolayers, whereas the number of the unit cells belonging to $\text{Al}_{0.3}\text{Ga}_{0.7}\text{As}$ monolayers for the barrier block equals to 3. The lattice constants for the well and barrier materials are 5.6533 Å and 5.65564 Å, respectively. The appearance of resonance-type peaks in the current density curves is typical for quasi-periodic systems, and the results obtained are in good agreement with the Tsu-Esaki model.

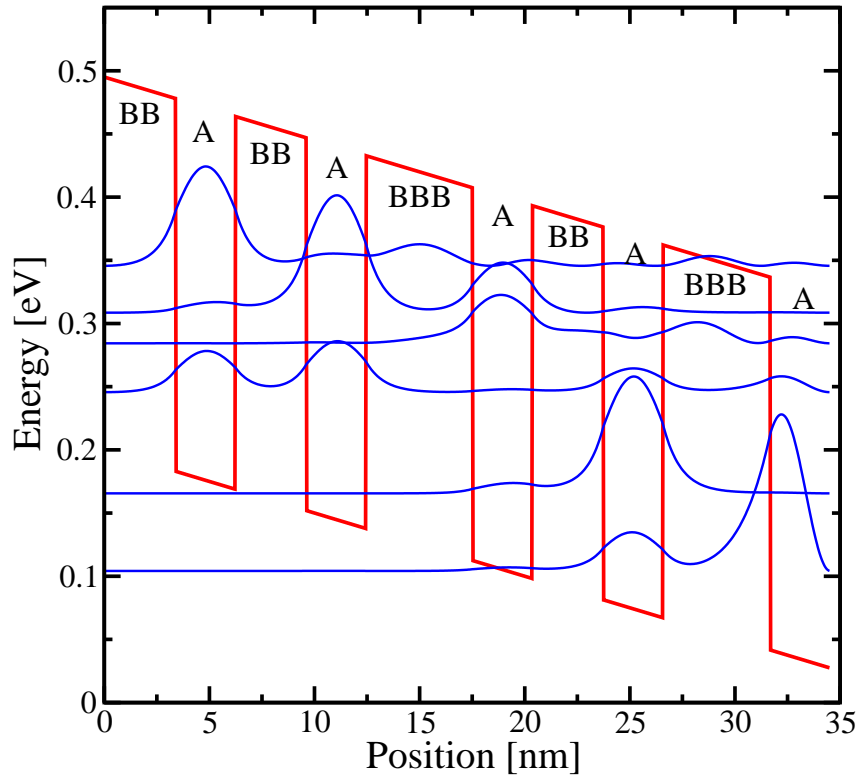


Figure 6.1: Band structure of the considered FSL at an applied field of 50 kV/cm.

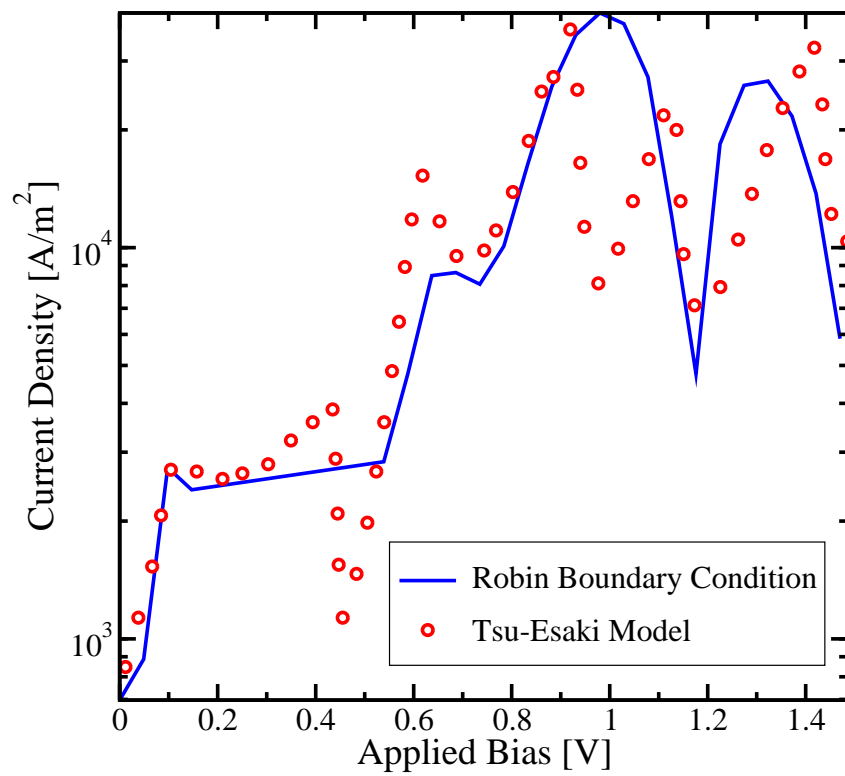


Figure 6.2: Current-density voltage characteristics of a GaAs/Al_{0.3}Ga_{0.7}As Fibonacci superlattice at $T = 200\text{K}$.

n	S_n	S'_n
1	A	A
2	B	B
3	BA	BBA
4	BAB	$BBABBAB$
5	$BABBA$	$BBABBABBBABBABBBA$

Table 6.1: A few initial generalized FSLs.

6.1.1.2 Comparison with the NEGF Approach

The ability of the Robin boundary conditions to produce satisfactory current carrying states is also verified by comparing our results for the tunneling current density with calculations based on nonequilibrium Green's functions (NEGF) [1]. For this purpose a typical example of a midinfrared quantum cascade laser is considered [9].

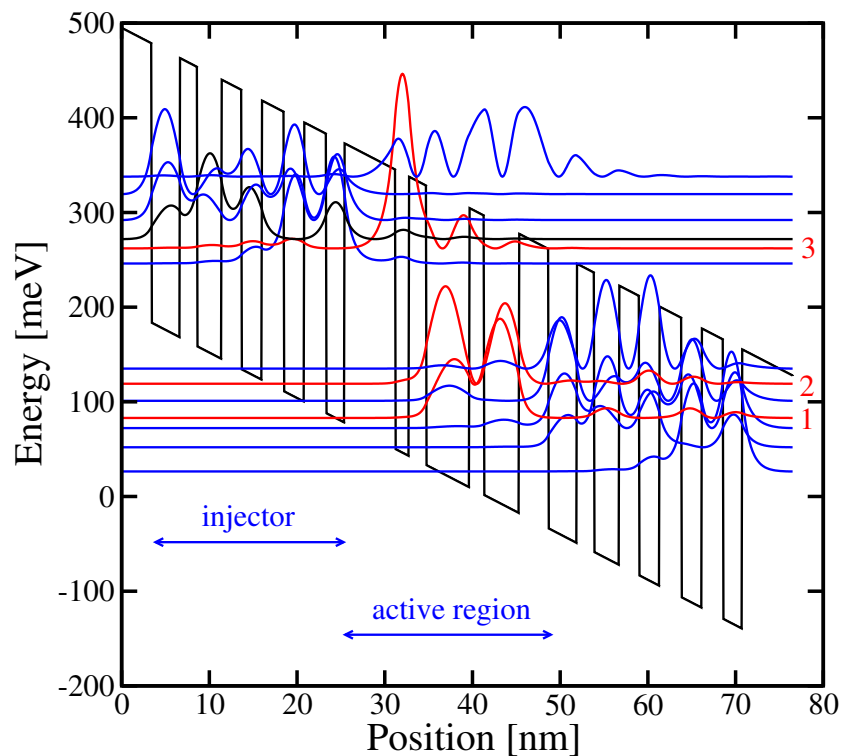


Figure 6.3: A schematic diagram of the conduction band profile for one and a half periods of the GaAs/Al_{0.33}Ga_{0.67}As QCL for an electric field of 48 kV/cm.

Figure 6.3 illustrates the conduction band profile of this device. The layer sequence of one period belonging to the GaAs/Al_{0.33}Ga_{0.67}As structure, in nanometers, starting from the injection barrier is: **5.8**, 1.5, **2.0**, 4.9, **1.7**, 4.0, **3.4**, 3.2, **2.0**, 2.8, **2.3**, 2.3, **2.5**, 2.3, **2.5**, and 2.1, where normal scripts represent the wells, bold the barriers.

The comparison of the obtained current-voltage characteristics with the simulation employing the nonequilibrium Green's functions method is illustrated in Figure 6.4. The simulation is performed with the number of periods to be 30 and the temperature is taken to be 77 K. As in the case of quasi-periodic superlattices, the application of our method to calculate current carrying states proves to be very promising for periodic QCL structures as well.

To illustrate the convergence of the solution to the Robin problem and the Dirichlet problem as $E_\alpha \rightarrow \infty$, we investigated the transformations of the wave functions as a function of the applied electric field, because the energy levels increase as the electric field decreases. For this purpose the real part of the wave functions belonging to the Robin problem are compared to the solutions of the Dirichlet problem. The imaginary part, indicating the development of the current carrying states, are studied analogously.

The order of magnitude we use for the electric field is 10^3 kV/cm on the one hand and 10^{-6}

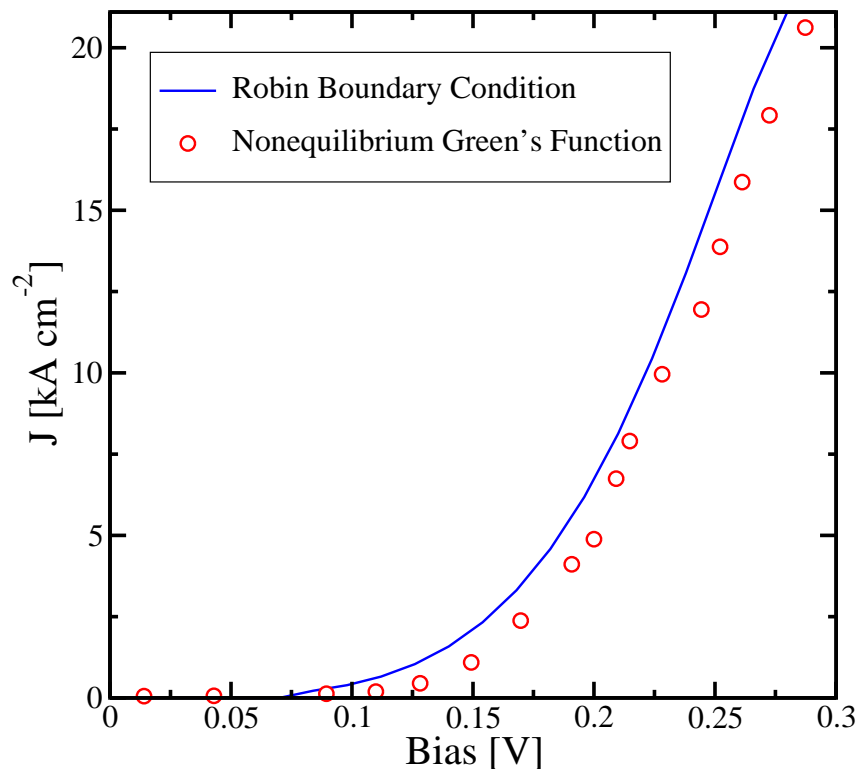


Figure 6.4: Comparison of the current-voltage characteristics of a GaAs/Al_{0.33}Ga_{0.67}As QCL calculated using the Robin boundary condition approach with a nonequilibrium Green's functions simulation [1].

kV/cm for the weak field calculation. The investigated structure is the same three-level QCL design as above. The real components of the wave functions are plotted in Figure 6.5 for the electric fields $F = 10^3$ kV/cm and $F = 10^{-6}$ kV/cm. For $F = 10^3$ kV/cm the calculations show obvious deviations in the spatial dependence between the solutions of the Robin and Dirichlet boundary value problems, unlike the weak field case $F = 10^{-6}$ kV/cm, where a convergence between these solutions is observable.

The imaginary components of the wave functions corresponding to the Robin boundary value problem are plotted in Figure 6.6. At the very small electric field $F = 10^{-6}$ kV/cm the imaginary part is almost zero everywhere except some very small peaks whose magnitudes are insignificant compared to the imaginary part of the wave function at $F = 10^3$ kV/cm.

Since the imaginary part of the wave function becomes zero with increasing energy, our results indicate that the tunneling current vanishes in this case. This behavior can be

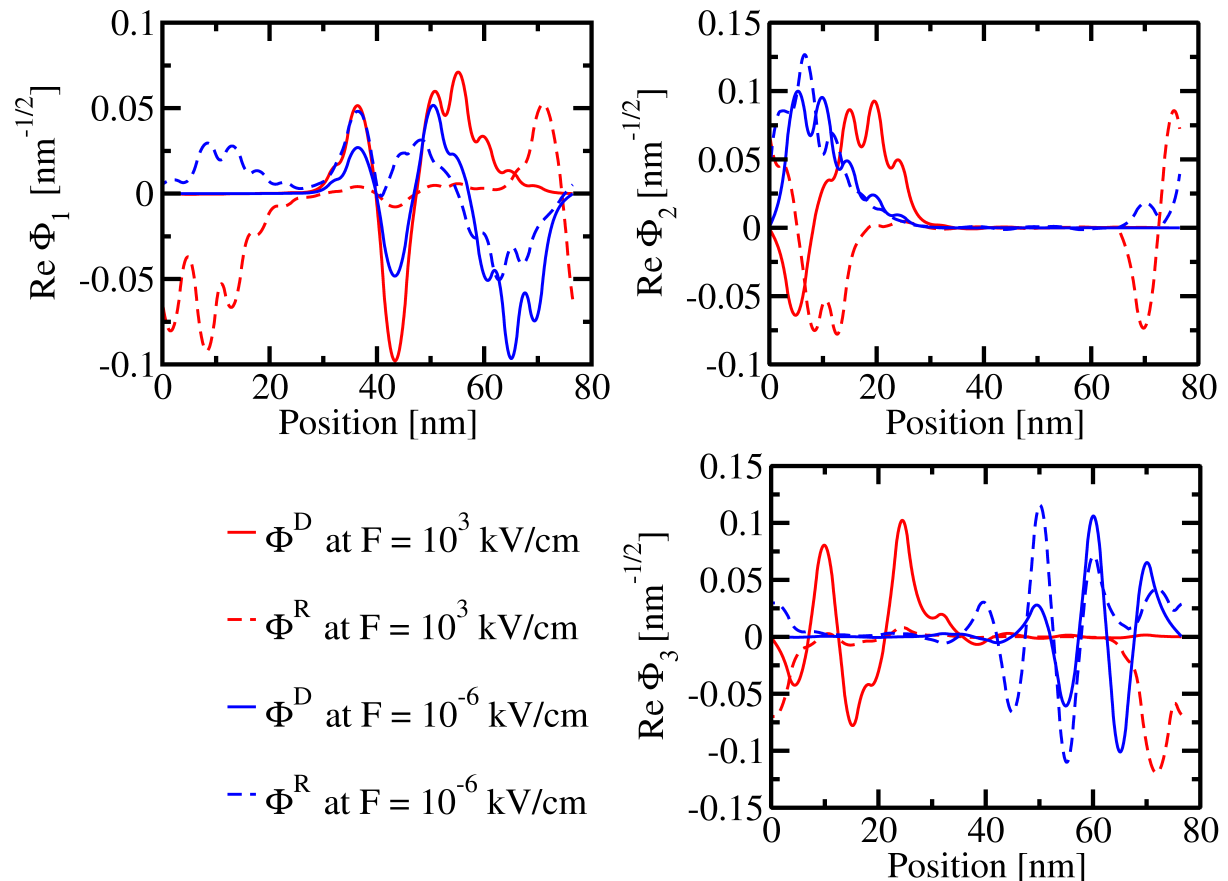


Figure 6.5: The spatial dependences of the real parts of the envelope functions are plotted for different values of the electric field. The solid lines correspond to the solution of the Dirichlet problem and the dashed lines represent the wavefunctions of the Robin problem.

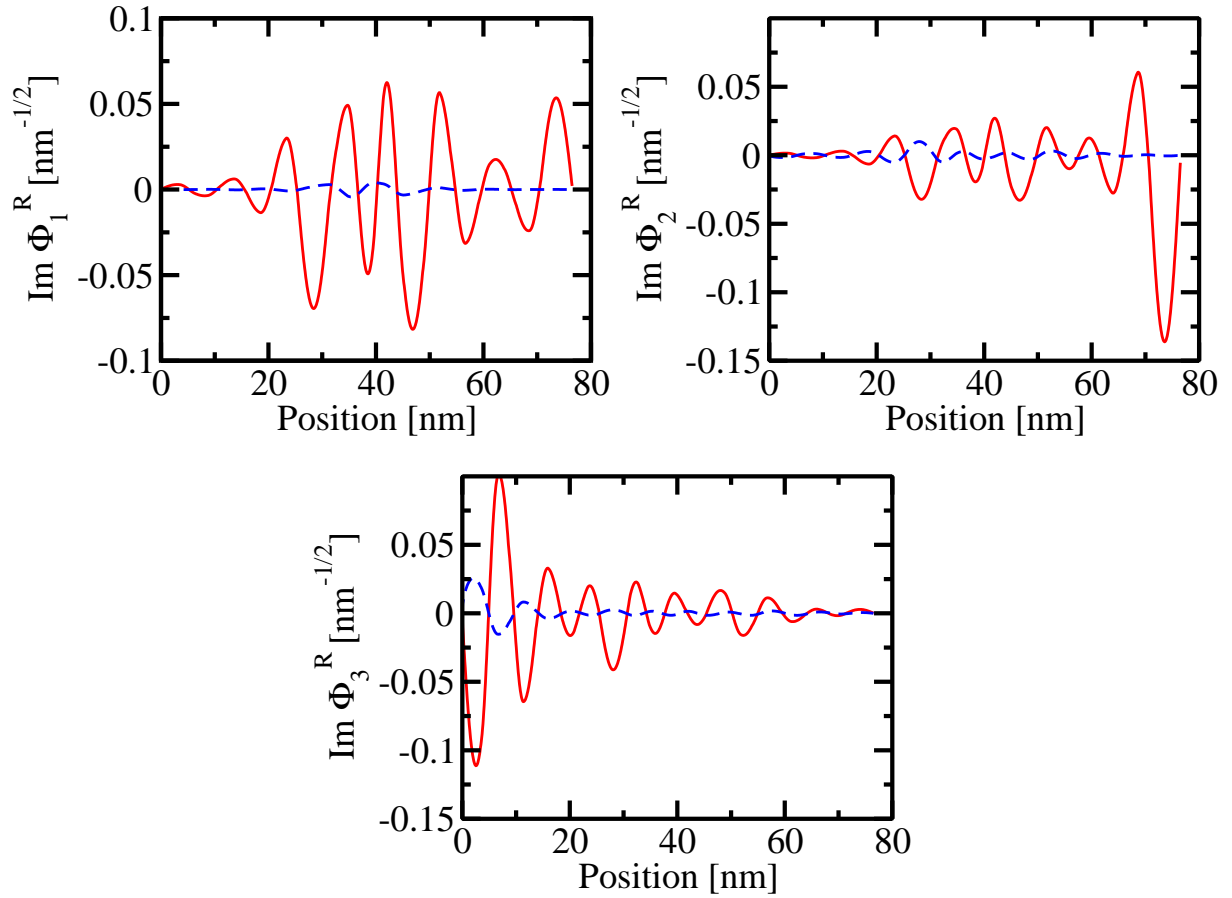


Figure 6.6: The spatial dependences of the imaginary parts of the envelope functions belonging to the solution of the Robin Problem at $F = 10^3 \text{ kV/cm}$ (solid line) and $F = 10^{-6} \text{ kV/cm}$ (dashed line).

understood in terms of the transmission coefficient which expresses the probability of tunneling and decays rapidly with energy according to [101]

$$T_c(E) = \left(1 + \frac{V^2 \sinh^2(L\sqrt{2m^*|V-E|/\hbar^2})}{4E(V-E)} \right)^{-1} \quad (6.4)$$

where T_c denotes the transmission coefficient for an electron in a heterostructure.

As mentioned above, the energy levels increase as the electric field decreases. Due to equation (6.4) the transmission coefficient decreases significantly with decreasing electric field, which is illustrated in Table 6.2. The three energy levels correspond to the upper and lower laser levels. Thus, by reducing the bias the conduction decreases and only minimal current flows. In this low field region the open boundary condition approach yields no significant deviation from the Dirichlet boundary value problem.

F	E_1	E_2	E_3	$T_c(E_1)$	$T_c(E_2)$	$T_c(E_3)$
10^3	9.7	11.4	24.4	0.683	0.721	0.787
10	31.5	49.8	67.8	0.524	0.611	0.672
10^{-2}	72.3	94.7	118.2	0.337	0.375	0.384
10^{-6}	114.6	138.8	169.3	0.118	0.133	0.171

Table 6.2: Column one contains the applied electric fields in kV/cm. The next three columns show the corresponding energy levels given in meV. Finally the transmission coefficients are given in the last three columns.

6.1.2 Optical Gain

Here, we focus on the calculation of optical gain under consideration of the proposed Robin boundary conditions. Due to the strong dependence of the dipole matrix element on the wave function the determination of optical gain qualifies for verification of boundary conditions.

In QCLs intersubband transitions contribute to the gain profile, especially the transitions between the upper and the lower laser level. In general, the standard expression for optical gain in semiconductors can be written as [102]

$$g(\hbar\omega) = \frac{\pi e^2 \hbar}{n \epsilon_0 c m_0^2 \hbar \omega} |M_{u,l}|^2 \rho \int [f_u(E) - f_l(E)] \Lambda(\hbar\omega) dE \quad (6.5)$$

Here, $f(E)$ denotes the distribution function for the electrons. $|M_{u,l}|^2$ represents the transition matrix element, ρ is the density of states, and Λ is the lineshape function. In a quantum well, the density of states can be taken as $\rho = m^*/\pi \hbar^2 L$ [103] and the transition matrix element is approximated by the dipole matrix element according to $M_{u,l} = m_0^2 \omega^2 |z_{ul}|^2$. Substituting these approximations for the density of states and the dipole matrix element, and using the line shape as proposed in [104]

$$\Lambda(\hbar\omega) = \frac{\gamma(E)/\pi}{[\hbar\omega - E]^2 + \gamma^2(E)} \quad (6.6)$$

the optical gain can be estimated as [105]

$$g(\hbar\omega) = \frac{e^2 |z_{ul}|^2 m^* \omega}{\hbar^2 c n_r \epsilon_0 L} \int_0^\infty dE \frac{\hbar \gamma(E) [f_u(E) - f_l(E)]}{\pi [\hbar\omega - E]^2 + [\hbar \gamma(E)]^2} \quad (6.7)$$

where z_{ul} is the dipole matrix element, n_r is the refractive index, ϵ_0 is the vacuum permittivity and c is the speed of light. The dipole matrix element depends strongly on the wave functions of the relevant states, and so does the optical gain.

The validity of equation (6.7) is not restricted to any particular scattering mechanism. Certain assumptions have to be made about γ . We assume that the homogeneous broadening γ is dominated by the interaction with optical phonons [106]. Thus

$$\gamma(E) = \gamma_0 \times \begin{cases} N_{ph} \\ (N_{ph} + 1)\Theta(E - \hbar\omega_{ph}) \end{cases}$$

The top line describes optical phonon absorption and the bottom line optical phonon emission, where $\gamma_0 = (\pi e^2/2\hbar)[1/\varepsilon_\infty - 1/\varepsilon_0]q_{ph}$, $q_{ph} = (2m_e\omega_{ph}/\hbar)^{1/2}$, and the phonon occupation number is given by $N_{ph} = 1/(\exp(\hbar\omega_{ph}/k_B T) - 1)$. Furthermore, ε_s and ε_∞ are the low and high frequency dielectric constants respectively.

6.1.2.1 Calculation Results

We consider a laser consisting of 90 periods of a GaAs/Al_{0.15}Ga_{0.85}As heterostructure at a temperature of 70 K [107]. The GaAs/Al_{0.15}Ga_{0.85}As layer sequence in nanometers is **3.8**, 14.0, **0.6**, 9.0, **0.6**, 15.8, **1.5**, 12.8, **1.8**, 12.2, **2.0**, 12.0, **2.0**, 11.4, **2.7**, 11.3, **3.5**, and 11.6, where the AlGaAs layers are in bold. Figure 6.7 shows our simulation results to be in good agreement with measurements that are performed on this QCL design [108].

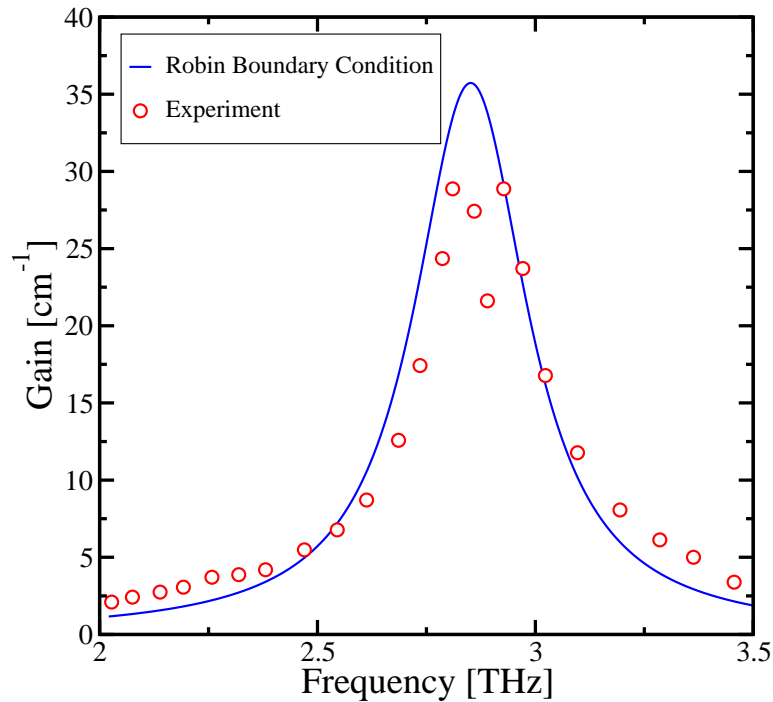


Figure 6.7: Optical gain of a THz GaAs/Al_{0.15}Ga_{0.85}As QCL driven at 160 A cm⁻². The solid line represents the result calculated using the Robin boundary condition approach and the dashed line corresponds to measured values.

The dipole matrix element between states Ψ_α and Ψ_β along the well growth direction z is given by [109]

$$z_{\alpha\beta} = A\langle\Psi_\alpha|z|\Psi_\beta\rangle = e^{i\mathbf{k}_\parallel\cdot\mathbf{x}_\parallel} \int_0^L z\Phi_\alpha^*(z)\Phi_\beta(z)dz \quad (6.8)$$

In order to obtain numerical illustrations for $z_{\alpha\beta} = e^{i2\pi k_\parallel/k_\parallel^{\max}} \int_0^L z\Phi_\alpha^*(z)\Phi_\beta(z)dz$, the product $|\mathbf{x}_\parallel|\cos(\mathbf{x}_\parallel, \mathbf{k}_\parallel)$ is set to $2\pi/k_\parallel^{\max}$, and $k_\parallel^{\max} = 0.1\text{nm}^{-1}$. The calculations of the dipole matrix elements, which performed for the two different electric field strengths 10^3 kV/cm and 10^{-6} kV/cm, are illustrated in Figure 6.8 as functions of the wave vector k_\parallel . The dashed curves represent the results determined taking into account Robin boundary conditions and the solid curves result from Dirichlet boundary conditions. A comparison of the results belonging to the different electric fields reveals that the solutions of the Robin and Dirichlet boundary value problems converge when lowering the electric field. Thus, our calculations demonstrate the accuracy of the proposed Robin boundary conditions for QCL simulations. However, for the unbiased case Dirichlet boundary conditions yield nearly comparable results.

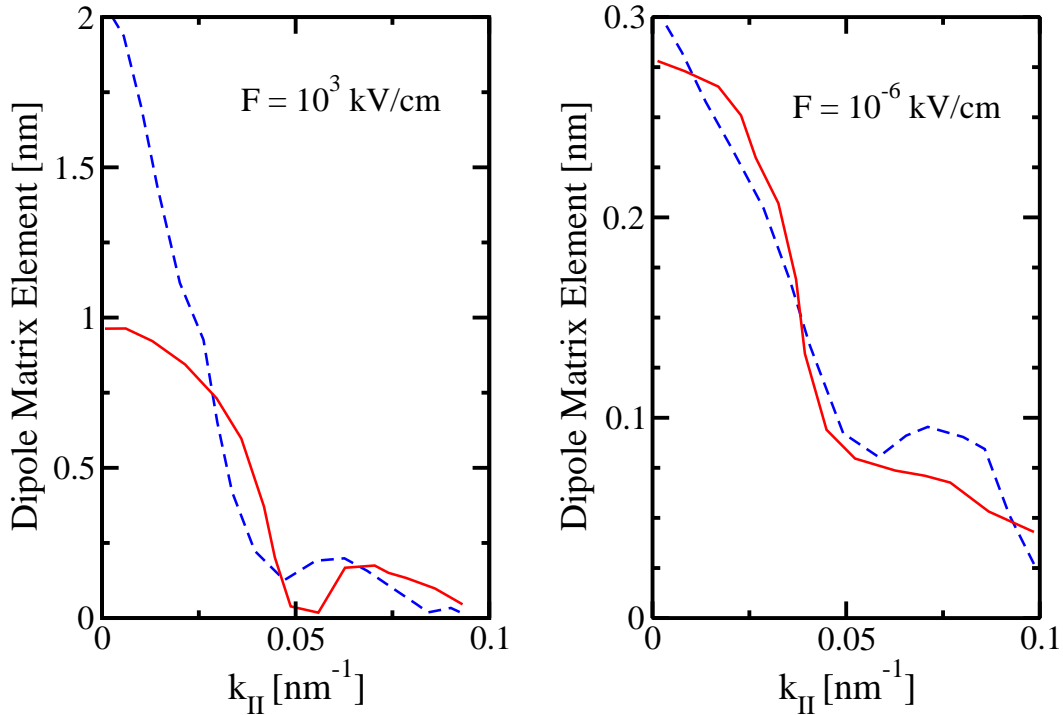


Figure 6.8: Calculated values of the dipole matrix elements for $F = 10^3$ kV/cm and $F = 10^{-6}$ kV/cm. The solid lines represent the solution of the Dirichlet problem and the dashed lines correspond to the solution of the Robin problem.

6.2 Design and Performance Investigations

6.2.1 A THz QCL

Using the Monte Carlo simulation scheme described previously, we have calculated the steady state carrier distributions and the current-voltage characteristics of a QCL in the THz region.

6.2.1.1 Structure

The structure considered consists of a combination GaAs wells and $\text{Al}_{0.15}\text{Ga}_{0.85}\text{As}$ barriers [110]. The layer sequence of one cascade, in nanometers, is: 9.2, **3**, 15.5, **4.1**, 6.6, **2.7**, 8, **5.5**, where normal scripts denote the wells and bold the barriers. Only the widest well is n-type doped with a low density of $1.8 \times 10^{10} \text{ cm}^{-2}$. Together with the squared envelope functions of the relevant bound states, the conduction band profile is plotted under an applied bias of 10 kV/cm in Figure 6.9.

The numerical values used for the relevant material parameters are listed in Table 6.3, where the difference in the electron affinity χ_e between the two materials determines the conduction band offset, and ϵ_S and ϵ_∞ denote the static and high frequency dielectric constants. For the given GaAs/AlGaAs system, these values are well established and can be looked up in [111] and [112].

The optical transitions occur between the upper and lower laser states. The lower laser state is rapidly depopulated into the states $5'$, $4'$ or $3'$ via LO-phonon emission. In order

	GaAs	$\text{Al}_{0.15}\text{Ga}_{0.85}\text{As}$
m_Γ^*	0.067	0.075
m_X^*	0.32	0.311
ϵ_S	12.90	12.47
ϵ_∞	10.89	10.48
χ_e [eV]	4.07	3.905
$\hbar\omega_{\text{LO}}$ [meV]	36.25	35.30
ρ [g/cm ³]	5.36	5.12
E_{ac} [eV/Å]	3.6	3.49
E_{op} [eV/Å]	5.9	6.0
$D_{\Gamma X}$ [eV/Å]	4.1	5.2

Table 6.3: Overview of the material parameters used in the simulation presented in this section, illustrated for the well and barrier material, respectively.

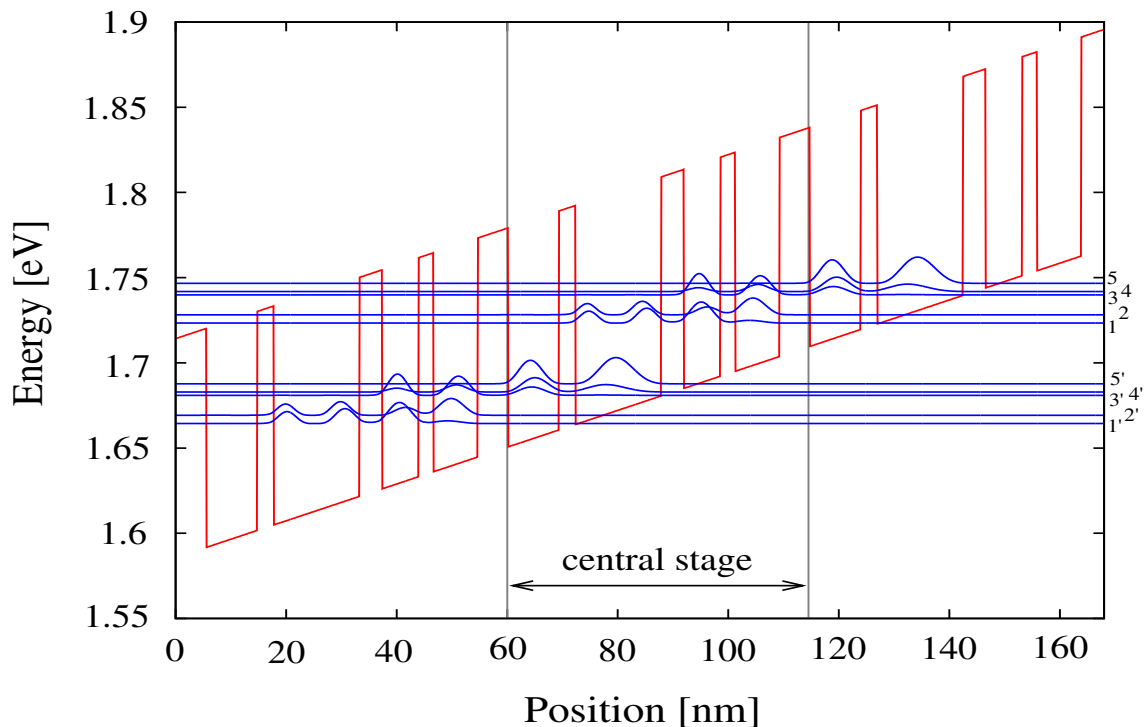


Figure 6.9: Calculated conduction band diagram and squared wave functions for a GaAs/Al_{0.15}Ga_{0.85}As QCL under an applied field of 10 kV/cm.

to enhance this process, the energy separation between these subbands should be close to the LO-phonon energy of the well material. Furthermore, the spatial overlap between the upper state and the lower state is kept as small as possible to increase the upper state lifetime. Figure 6.10 depicts the calculated LO-phonon rates $4 \rightarrow 4$ and $4 \rightarrow 3$. The energy of the initial states are given on the horizontal axis, and the zero energy reference value is taken at the bottom of subband 4.

6.2.1.2 Results

Starting with a constant population initially assigned to each subband and using a constant time step of 5 fs we have monitored 10000 particles during 10 ps. Initially each subband has an equal number of particles, and subsequently the ensemble evolves until the simulation ends. After each time step the statistics are updated. The numerical model for the QCL structure studied includes five subbands per stage and periodic boundary conditions are imposed [113].

Electron-LO phonon, acoustic and optical deformation potential, and intervalley scattering are included in the simulation with the relevant scattering rates computed at a temperature of 70 K and stored for each subband pair for a discrete number of initial

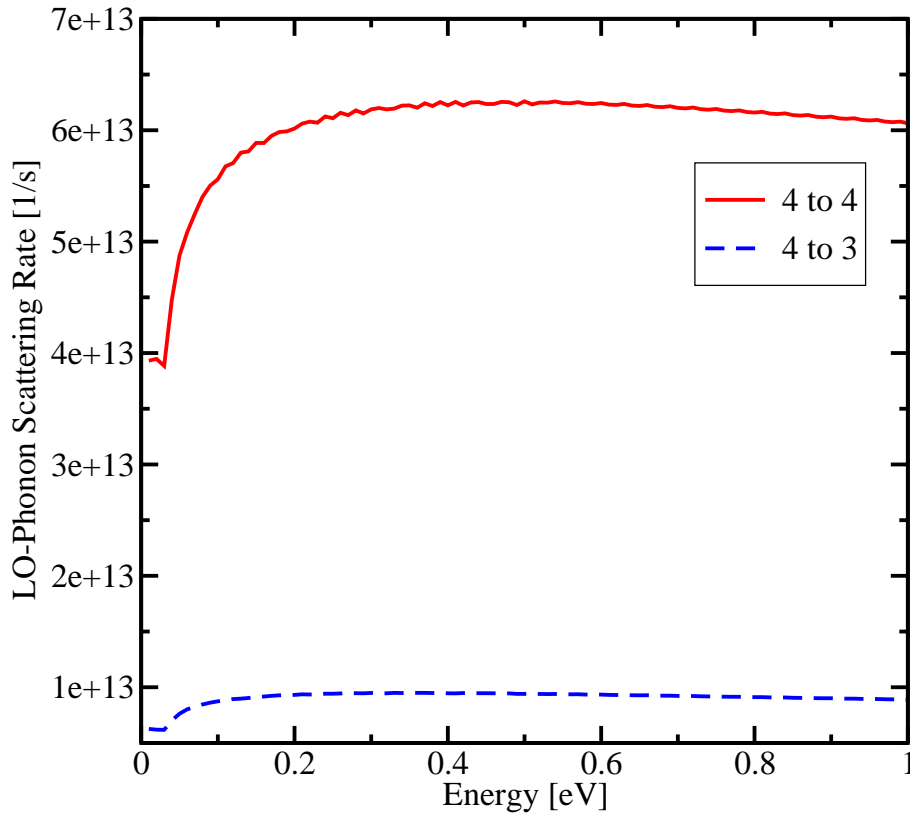


Figure 6.10: Calculated LO-phonon scattering rates $4 \rightarrow 4$ and $4 \rightarrow 3$ at an applied bias of 10 kV/cm and an operating temperature of 70 K.

electron energies.

Figure 6.11 shows the time evolution of the current density with and without Γ -X intervalley scattering at an electric field of 10 kV/cm. It can be seen that the inclusion of intervalley scattering increases the current density indicating that the Γ -X electron transfer plays a significant role as a mechanism for depopulation of the lower laser level. In Figure 6.12, the obtained electron distributions of the individual subbands are depicted over the kinetic energy.

Figure 6.13 displays the obtained current density with and without X valley transport, where the range of the applied field is 10 to 70 kV/cm and the chosen calculation step is 5 kV/cm. The results demonstrate that for this QCL structure the inclusion of Γ -X intervalley scattering leads to an increase in the current flow. Without Γ -X electron transfer the results are up to 10 % lower.

The output characteristics of the Monte Carlo simulation show that the effect of intervalley scattering processes is significant for the charge transport and not negligible in performance investigations.

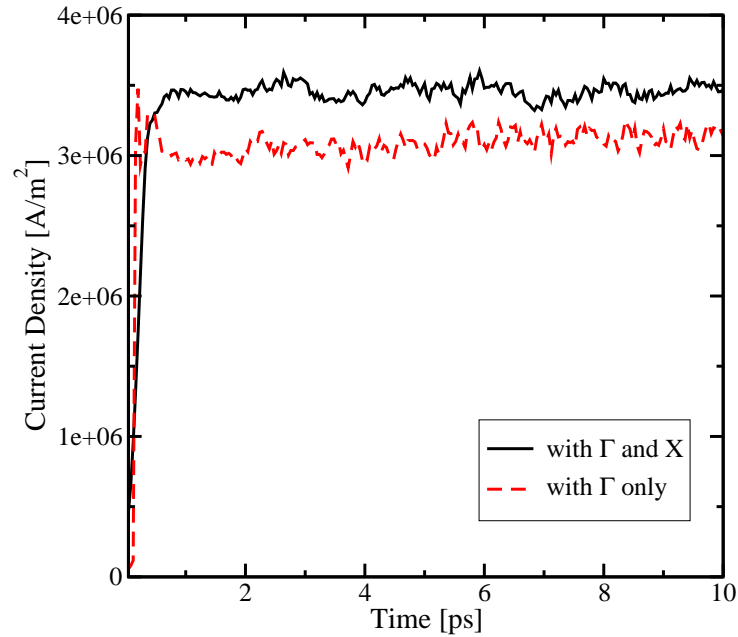


Figure 6.11: Time evolution of the current density at an electric field of 10 kV/cm, with and without Γ -X intervalley scattering, illustrating the good convergence behavior. The current densities averaged over the time are $3.45 \cdot 10^6$ A/m² by including the X valley, and $3.08 \cdot 10^6$ A/m² for the Γ valley only.

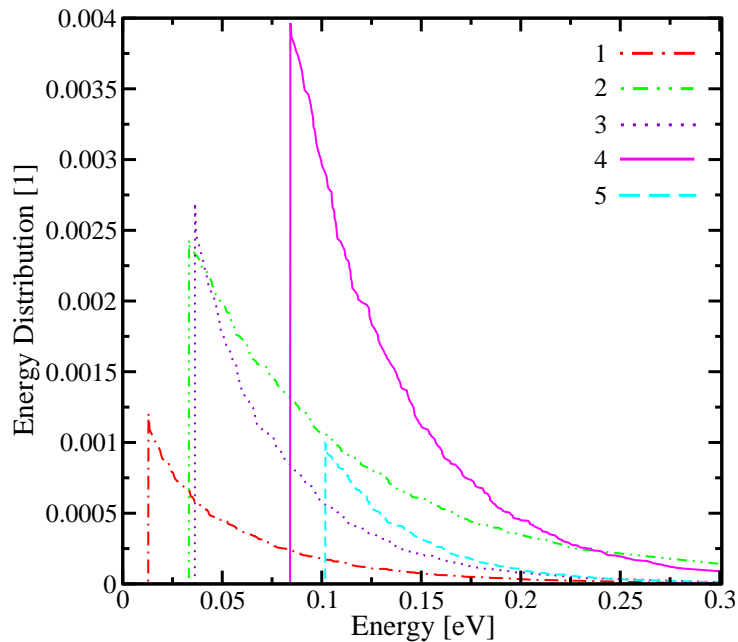


Figure 6.12: Population of the individual subbands as a function of the kinetic energy.

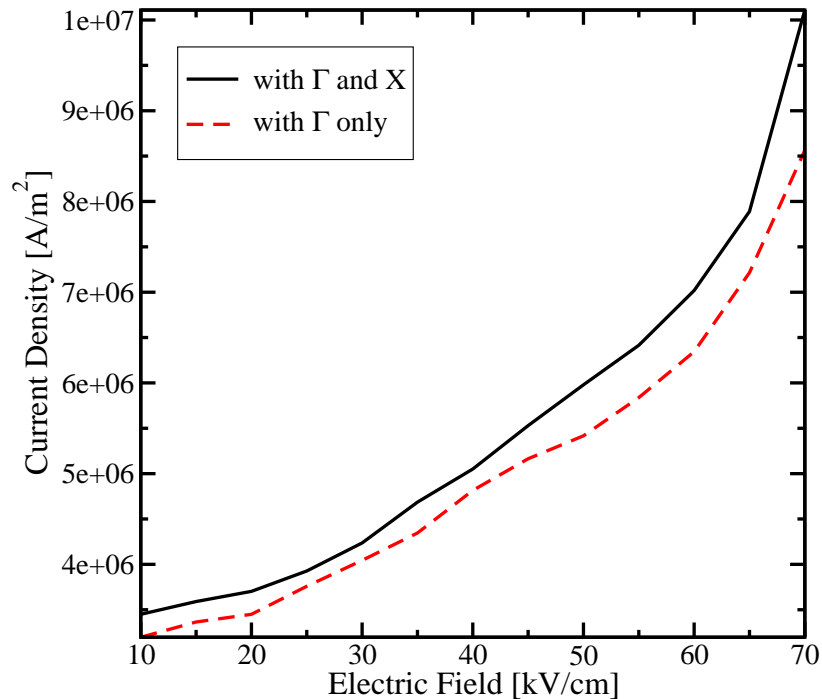


Figure 6.13: Current density as a function of the applied electric field with and without X valley transport.

6.2.1.3 Interface Roughness Effects

In this section, the impact of interface roughness scattering on the device performance is of particular interest. Especially, we focus on the temperature sensitivity of the electron transport. For this purpose, we take a look at the subband population and the current density as a function of the temperature. Throughout the simulations, the characteristic height and the correlation length of the interface roughness are taken as $\Delta = 2.83 \text{ \AA}$ and $\Lambda = 70 \text{ \AA}$ respectively [114].

In Figure 6.14 and 6.15 we show the calculated electron distributions of the upper and lower subband for different temperatures. In general, the interface roughness scattering is found to be more dominant for higher temperatures. Moreover, it changes the occupation of the upper and lower laser levels significantly. We observe an increase in the occupation of the upper laser level due to interface roughness, while the occupation of the lower laser level gets reduced. The variations of the occupation due to rough interfaces increase with temperature, and for 300 K the variation can be as large as 27%, which illustrates their important influence on this THz QCL design.

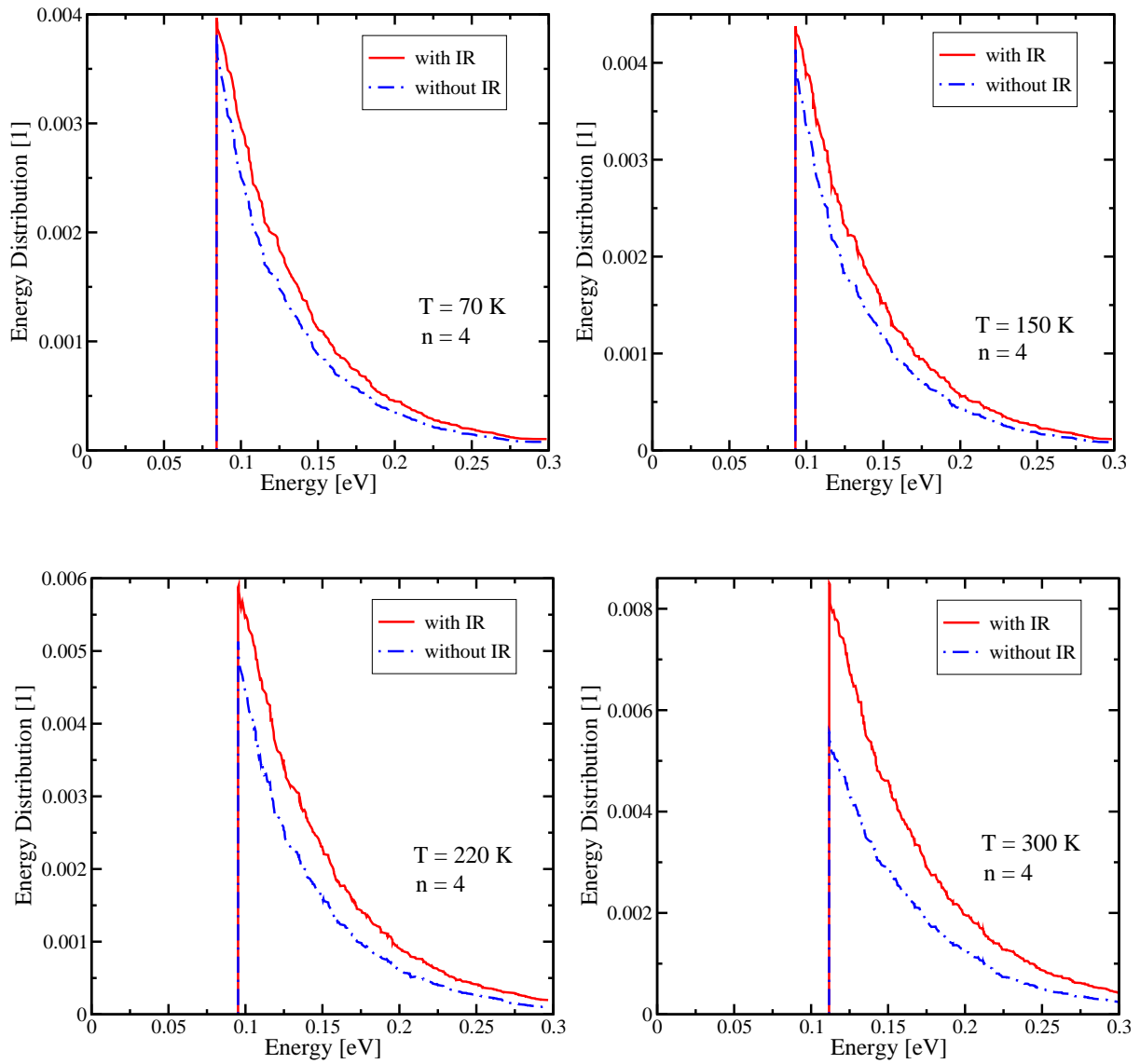


Figure 6.14: Comparison of the energy distributions of subband 4 for different temperatures. The dashed lines show the results without interface roughness scattering and the solid ones illustrate the results including scattering on rough interfaces.

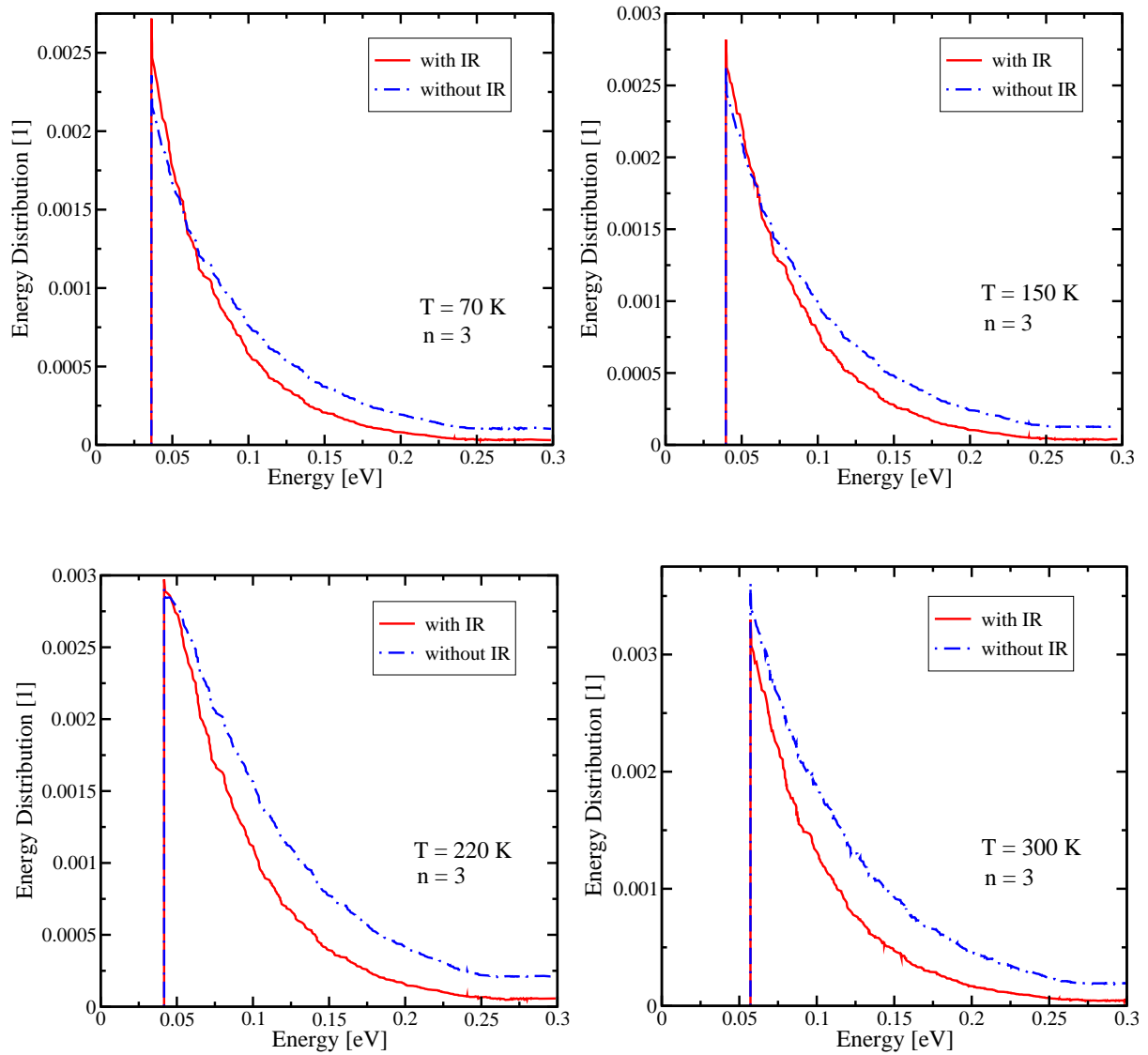


Figure 6.15: Comparison of the energy distributions of subband 3 for different temperatures. The dashed lines show the results without interface roughness scattering and the solid ones illustrate the results including scattering on rough interfaces.

In general, we observe a significant increase in the population of the upper laser level for higher temperatures, while the population of the lower laser level decreases somewhat.

The effect of rough interfaces on the current voltage characteristics is illustrated in Figure 6.16 where the current density with and without interface roughness scattering is displayed. The temperature is taken as 70 K. Interface roughness scattering enables a better population of the upper levels and obviously increases the current density. Moreover, this effect gets more dominant for higher electric fields.

Figure 6.17 illustrates the dependence of the current density on the temperature for the considered THz QCL structure at different applied biases. In the case of $F = 10$ kV/cm, the inclusion of interface roughness scattering results in a significant impact only for higher temperatures. However, for $F = 70$ kV/cm the effect of rough interfaces is noticeable even for 70 K and increases with temperature.

The determined results demonstrate that interface roughness scattering plays an important role for the electron transport in THz QCLs. This mechanism introduces a significantly higher temperature sensitivity for the electron transport.

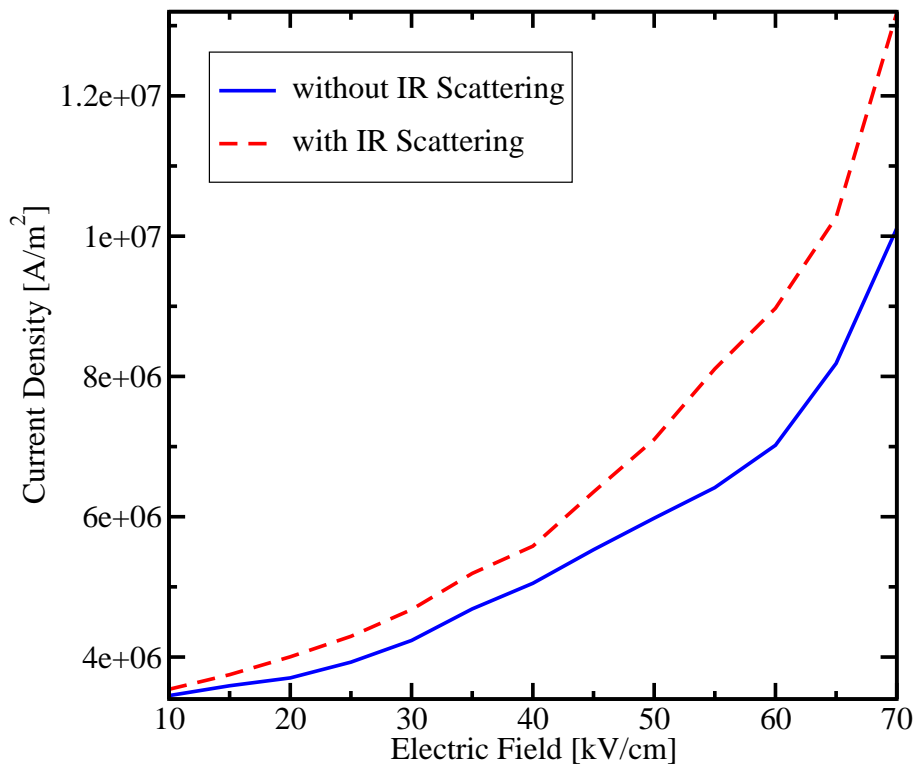


Figure 6.16: Current density as a function of the applied electric field with and without interface roughness scattering at 70 K.

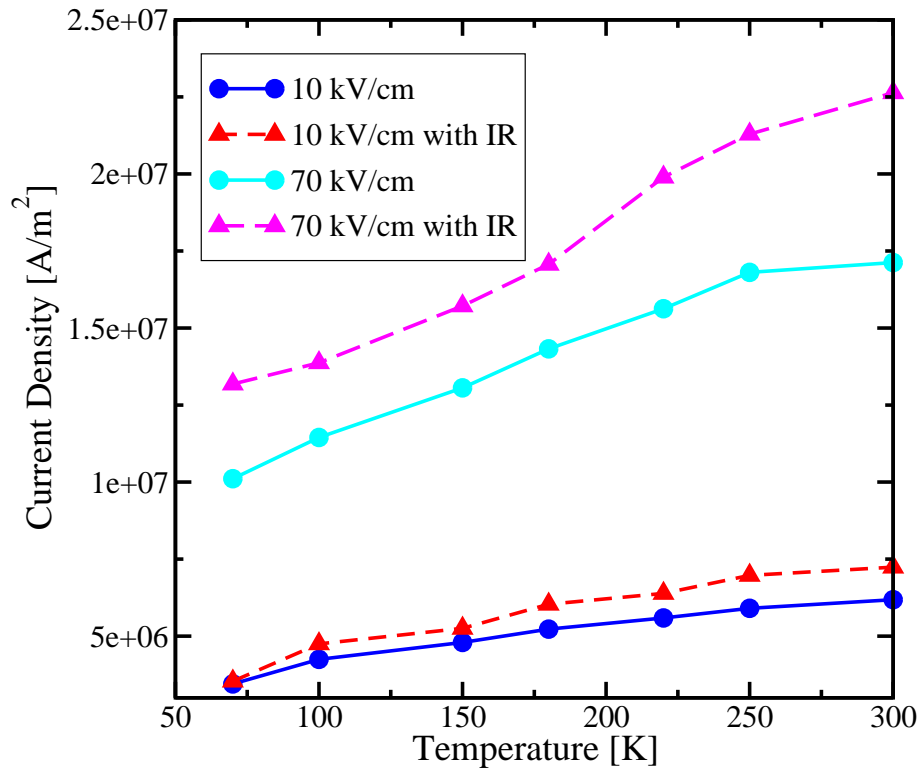


Figure 6.17: Current density as a function of the temperature with and without interface roughness scattering.

6.2.2 Mid-infrared QCL

The simulator has been used to simulate a GaAs/AlGaAs MIR QCL structure and investigate the role of Γ -X intervalley scattering as a mechanism for the depopulation of the lower laser level, since a lot of interest arose for intervalley electron transfer in quantum well structures [115–117].

We propose to modify the Al content and the width of the collector barrier of the given QCL design in order to increase the overlap between the upper X-state of the next stage and the lower Γ -state of the central one.

6.2.2.1 Initial Structure

Figure 6.18 illustrates the conduction band profile under an applied field of 40 kV/cm. In the following, we will call this design structure A, where the layer sequence of one cascade starting from the collector barrier is, in nanometers [2]: **3.9**, 2.6, **3.1**, 2.8, **2.9**, 2.9, **2.7**, 2.9, **2.4**, 2.9, **2.2**, 2.9, **2.2**, 3, **2**, 3.2, **2**, 3.5, **1.9**, 4.3, **0.94**, 5, **0.94**, 5.4, **0.94**, and 1.6. Normal scripts denote the GaAs wells and bold ones the $\text{Al}_{0.45}\text{Ga}_{0.55}\text{As}$ barriers. The upper laser level is labeled 9, and the lower level is labeled 2.

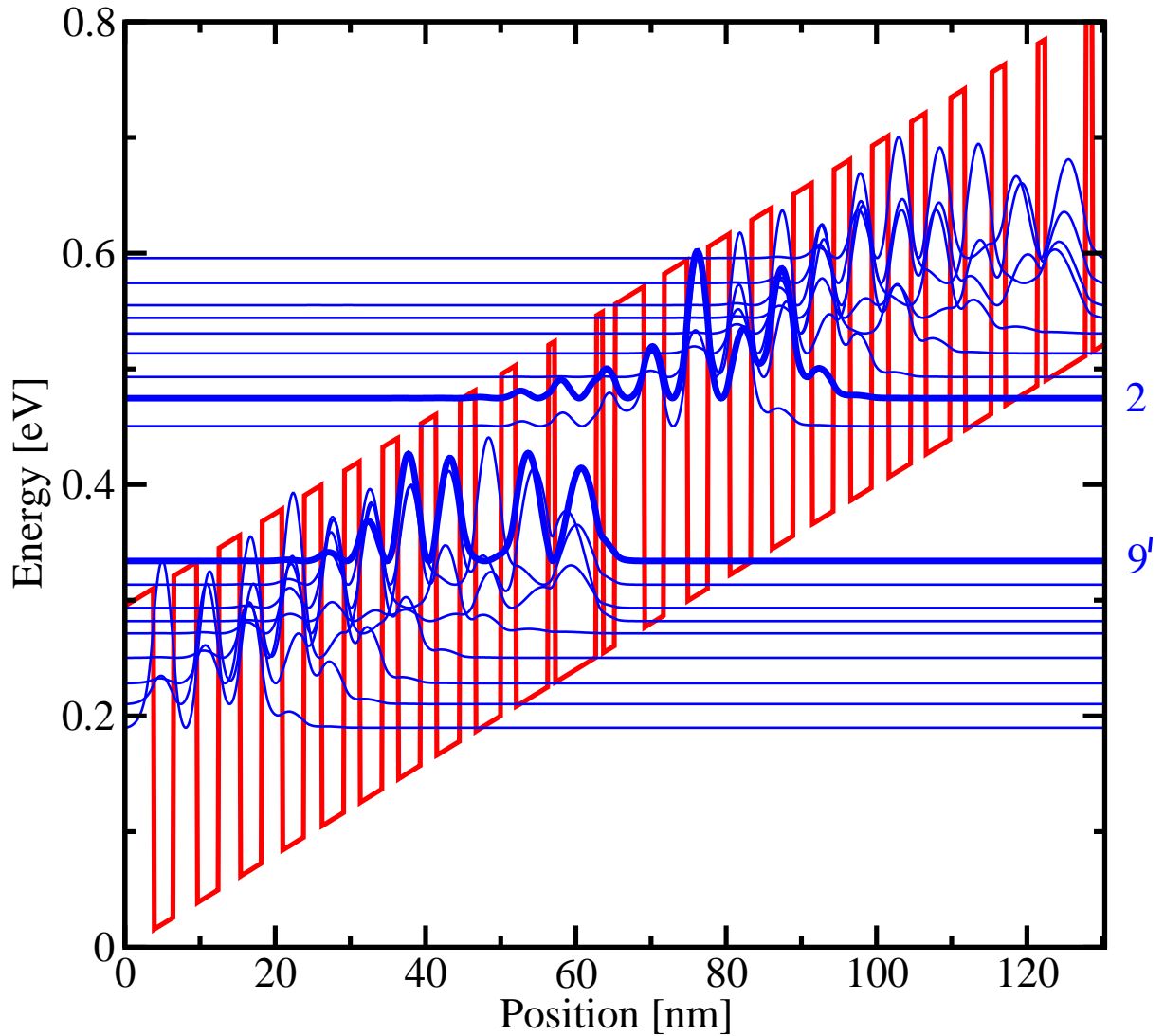


Figure 6.18: Conduction band diagram and squared wave functions for a GaAs/ $\text{Al}_{0.45}\text{Ga}_{0.55}\text{As}$ QCL in the MIR region under an applied field of 40 kV/cm [2]. The conduction band discontinuity between GaAs and $\text{Al}_x\text{Ga}_{1-x}\text{As}$ layers is taken to be $\Delta E_c = 1.1x$ eV for $0 \leq x \leq 0.45$, and $\Delta E_c = 0.43 + 0.14x$ eV for $0.45 < x \leq 1$.

6.2.2.2 Optimization of the Collector Barrier

The idea is to modify the collection barrier in a way that the Γ -X intervalley scattering mechanism can be used for an improvement of the device performance. Primarily, the intention is to increase the overlap between the lower Γ -state of the central stage and the upper X-state of the next stage. This is realized by modifying the width and the Al content of the collector barrier. In the following, the modified design will be called structure B.

Figure 6.19 shows the overlap between the lower Γ -state and the upper X-state of two adjacent stages for different Al contents and collector barrier widths. Regarding structure B, these results suggest to set the collector barrier width to 4.5 nm and the Al content to 35 %.

Applying these modifications, the determined Γ -X intervalley scattering between the lower state 2 and the upper state 9' of the next stage increases significantly. Figure 6.20 illustrates this circumstance by showing the corresponding scattering rate for structure A and structure B at an electric field of 40 kV/cm.

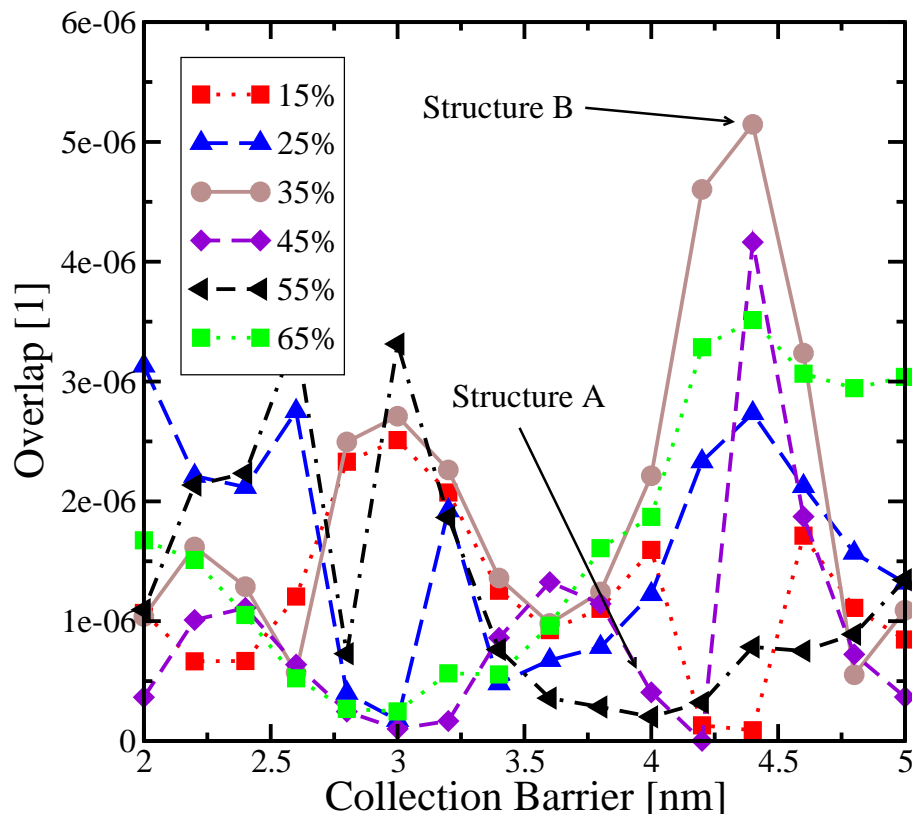


Figure 6.19: Overlap between the lower Γ -state of the central stage and the upper X-state of the next stage at an electric field of 40 kV/cm in dependence on the Al content.

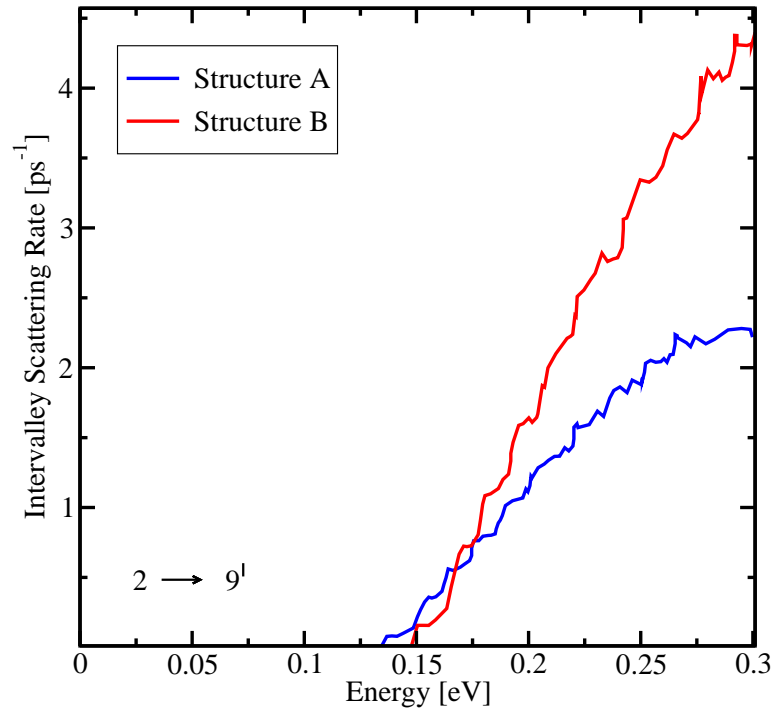


Figure 6.20: Γ -X intervalley scattering between the lower state 2 and the upper state 9^1 of the next stage at $F = 40 \text{ kV/cm}$.

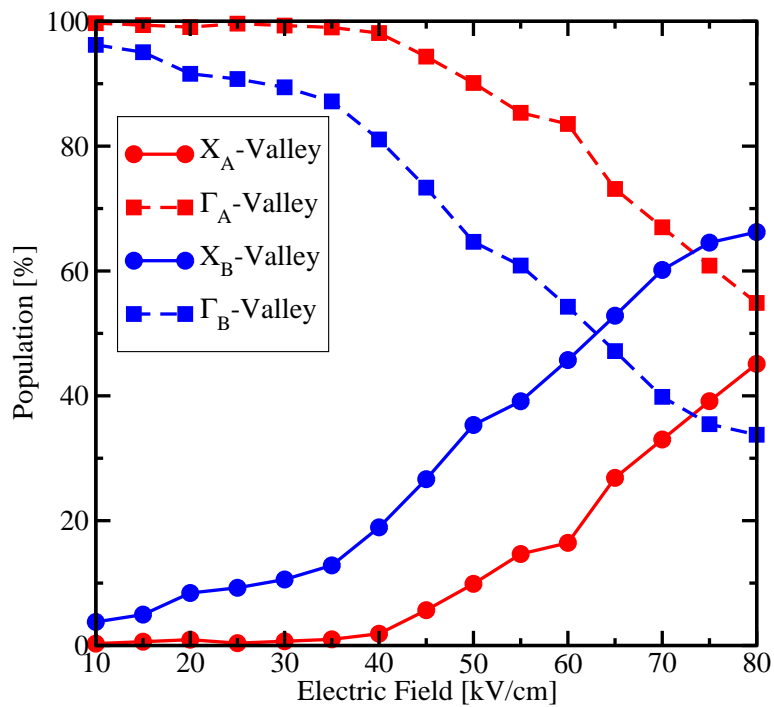


Figure 6.21: Electron population of the Γ and X valleys in dependence on the electric field.

In Figure 6.21, the variation of the electron population in the Γ and X valleys with the electric field is presented. By comparing the trends of structure A and structure B, one can observe that the X-valley electron population increases with the field, where the increase is obviously higher for structure B.

Our results indicate a significant increase in current density when considering Γ -X intervalley scattering for the modified structure B, whereas structure A shows negligible deviations. Figure 6.22 shows the obtained current densities for both structures in dependence on the electric field and highlights the importance of intervalley charge transport for QCL design considerations [118].

Since design modifications in terms of optimizing the overlap cause a crucial change in charge transport properties, it is obvious that the inclusion of X-states in the QCL dynamics introduces a new degree of freedom in the engineering of intersubband devices.

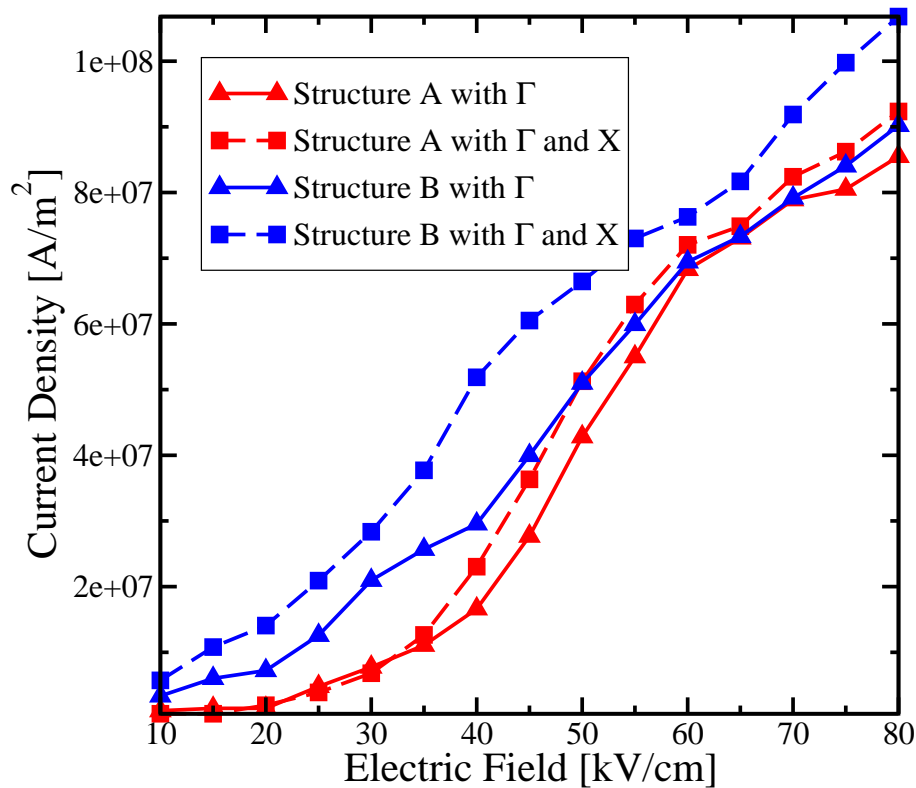


Figure 6.22: Current density as a function of electric field for structure A and structure B, with and without X-valley transport.

6.2.3 Simulation of an Al-free QCL

Here, a comparison of simulation results with experimental measurements for a recently developed InGaAs/GaAsSb QCL is presented. Aluminum-free QCLs are of big interest, since these structures do not suffer from degradation owing to the oxidation of aluminum during the fabrication process and laser operation [119]. Furthermore, aluminum-free structures are resistant to dark-line defects [120], which are responsible for abrupt failures in GaAs/AlGaAs lasers. A promising candidate for an aluminum-free QCL is the InGaAs/GaAsSb material system where the electron effective mass in the GaAsSb barriers is $0.045 m_0$. Compared to common QCL barriers such as AlGaAs and InGaAs, this effective mass is low and results in the growth of thicker barriers which are less sensitive to thickness fluctuations [121–123]. This is the notable advantage of InGaAs/GaAsSb structures compared to designs containing aluminum.

6.2.3.1 Structure

Figure 6.23 illustrates the conduction band profile for the considered QCL under an applied bias of 30 kV/cm. The layer thicknesses of the $\text{In}_{0.53}\text{Ga}_{0.47}\text{As}/\text{GaAs}_{0.51}\text{Sb}_{0.49}$ structure starting from the injection barrier are, in nanometers [3]: **8.1**, 2.7, **1.3**, 6.7, **2.2**, 5.9, **7.0**, 5.0, **1.9**, 1.2, **1.9**, 3.8, **2.7**, 3.8, **2.8**, 3.2. The barriers are in bold, and the underlined layers are Si doped ($4 \times 10^{17} \text{ cm}^{-3}$). The fabricated QCL is 60 μm wide and 2 mm long.

Table 6.4 shows the numerical values for some relevant material parameters. These standard values can be looked up in the literature [124–129].

	$\text{In}_{0.53}\text{Ga}_{0.47}\text{As}$	$\text{GaAs}_{0.51}\text{Sb}_{0.49}$
m_{Γ}^*	0.043	0.045
m_X^*	0.279	0.26
ϵ_S	13.90	14.30
ϵ_{∞}	11.60	12.64
χ_e [eV]	4.06	4.46
$\hbar\omega_{\text{LO}}$ [meV]	34	33.20
ρ [g/cm ³]	5.50	5.45
E_{ac} [eV/Å]	6.4	5.7
E_{op} [eV/Å]	7.2	6.8
$D_{\Gamma X}$ [eV/Å]	1.6	2.4

Table 6.4: Material parameters for the well and barrier material used in the simulation.

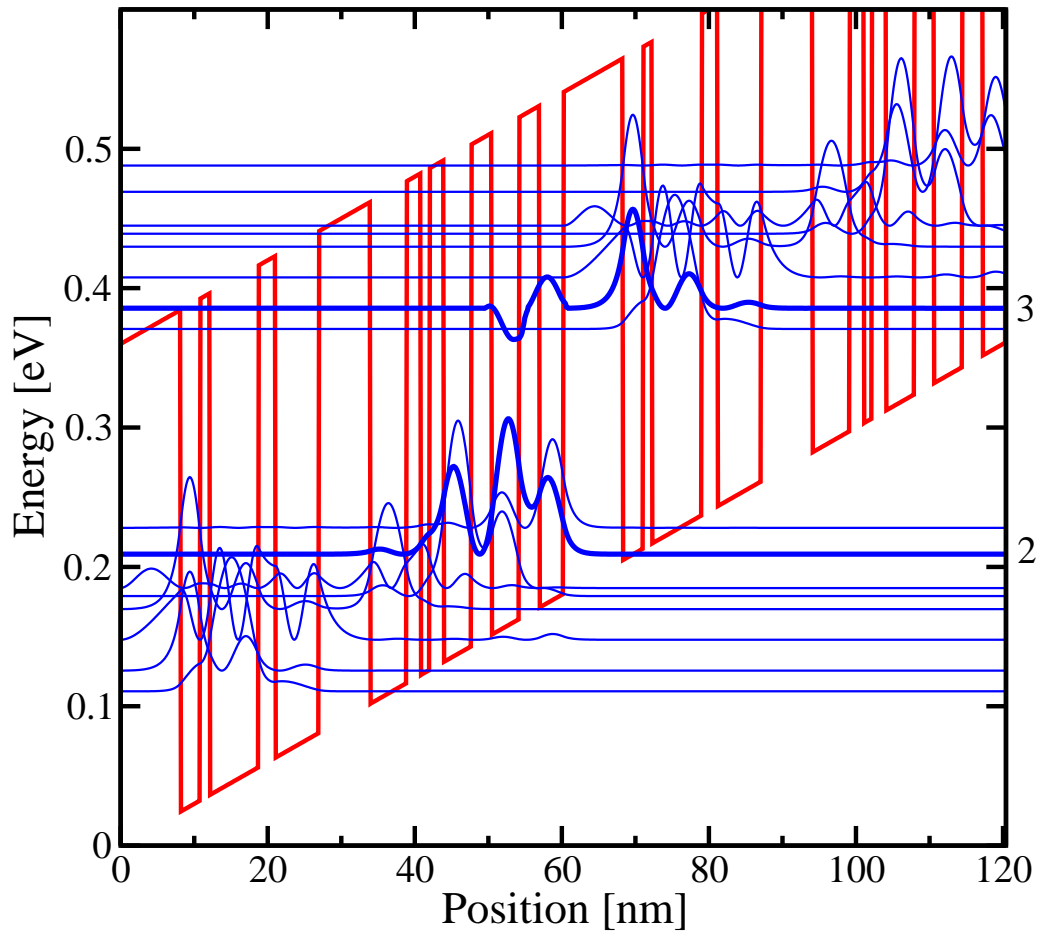


Figure 6.23: Conduction band diagram for an $\text{In}_{0.53}\text{Ga}_{0.47}\text{As}/\text{GaAs}_{0.51}\text{Sb}_{0.49}$ QCL under an applied field of 30 kV/cm [3]. The upper and lower laser levels are labelled with 3 and 2, respectively.

6.2.3.2 Results of the Monte Carlo Simulation

As in the simulations described before, we use a constant time step of 5 fs and monitor 10000 particles during 10 ps. According to the Monte Carlo algorithm presented in this work, we calculated the current density for this device and compared the obtained voltage-current characteristics with the measured values, which is illustrated in Figure 6.24. Electron scattering by polar optical and acoustic phonons, optical deformation potential interaction, inter-valley phonons, and interface roughness are included. The dashed curve displays the calculated current density for several bias points, while the symbols represent the measured values. The calculated and measured voltage-current characteristics are in good agreement, and the existing deviations can be attributed to the non-optimized scattering parameters and to additional scattering mechanisms not considered in the simulation.

Figure 6.25 shows the current density as a function of the temperature with and without interface roughness scattering. We observe a weak dependence of the current density on temperature, which can be explained by the dominance of electron scattering due to PO-phonon emission.

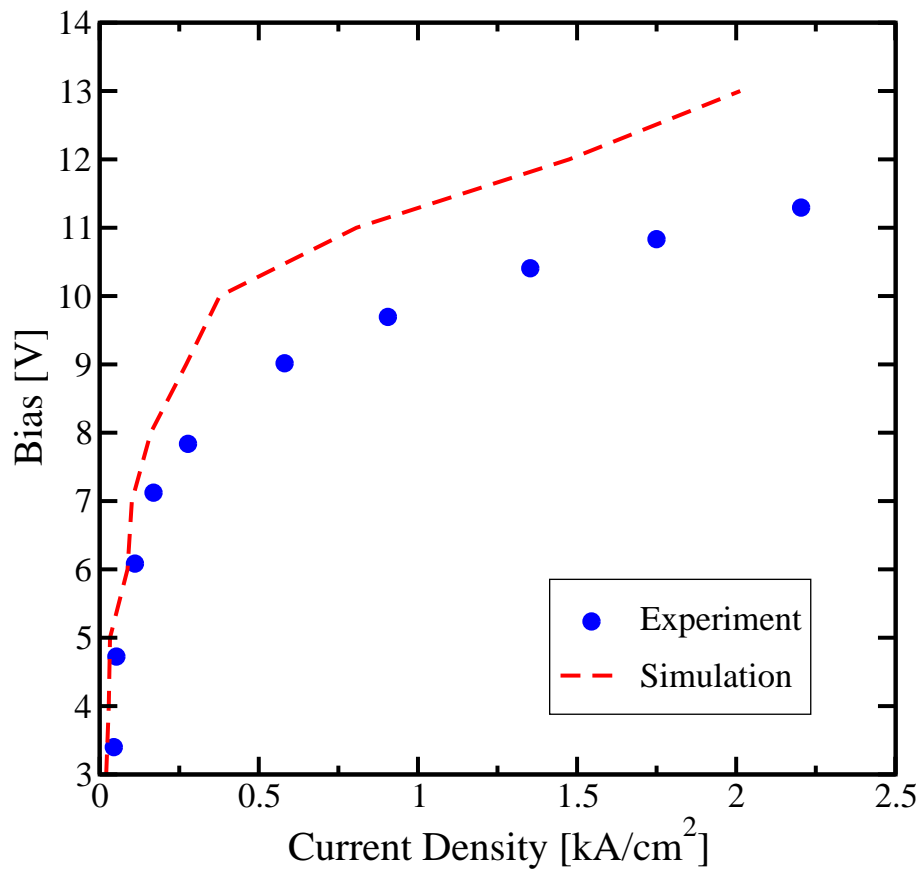


Figure 6.24: Voltage-current characteristics at $T = 78$ K.

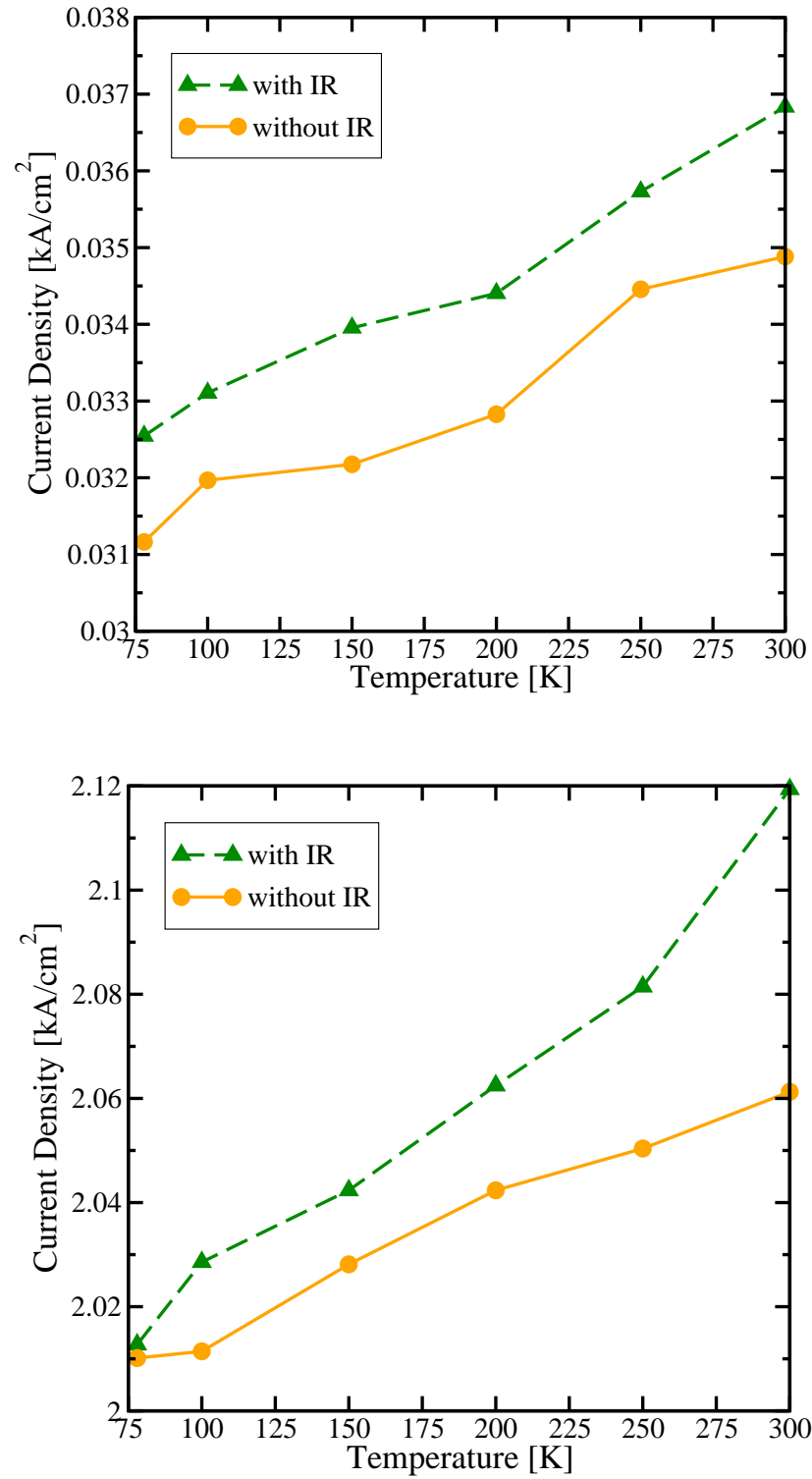


Figure 6.25: Current density versus temperature at 5 V and 13 V with and without interface roughness scattering.

The scattering rate due to emission of polar optical phonons as a function of temperature for different bias points is plotted in Figure 6.26. A weak temperature dependence can be seen from this diagram.

The dominance of electron scattering due to polar optical phonons is clearly illustrated by Figure 6.27 where the energy distributions of the upper and lower laser levels are depicted. The orange curves show the results without polar optical phonon scattering and the green ones illustrate the results including scattering due to polar optical phonons. We observe an increase in the occupation of the upper level and the lower level, while the increase of the upper level is much more significant compared to the lower level. The results plotted in this Figure fully support the notion that the polar optical phonon scattering mechanism is essential in order to provide a good condition for population inversion.

Since one of the aims in designing QCL structures is to obtain a significant population inversion between the upper and lower laser level, it is crucial to find out what mechanisms are decisive to achieve it. Our modeling approach was able to demonstrate that the scattering due to polar optical phonons is mainly accounting for this behavior regarding this MIR QCL design.

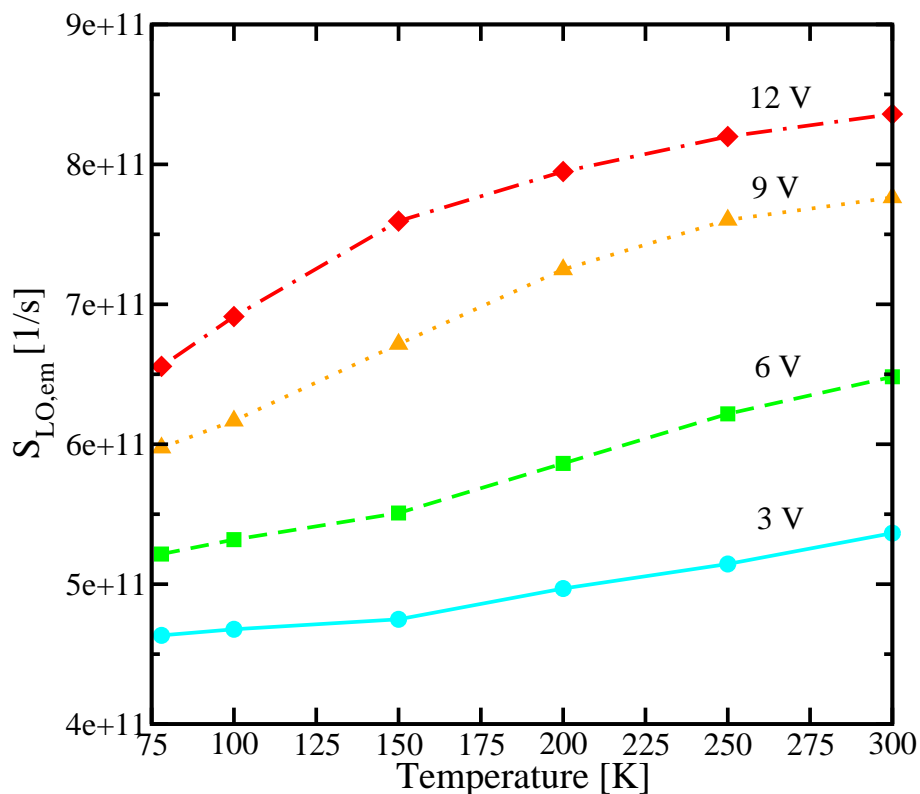


Figure 6.26: Scattering rate due to LO phonon emission as a function of temperature at several bias points.

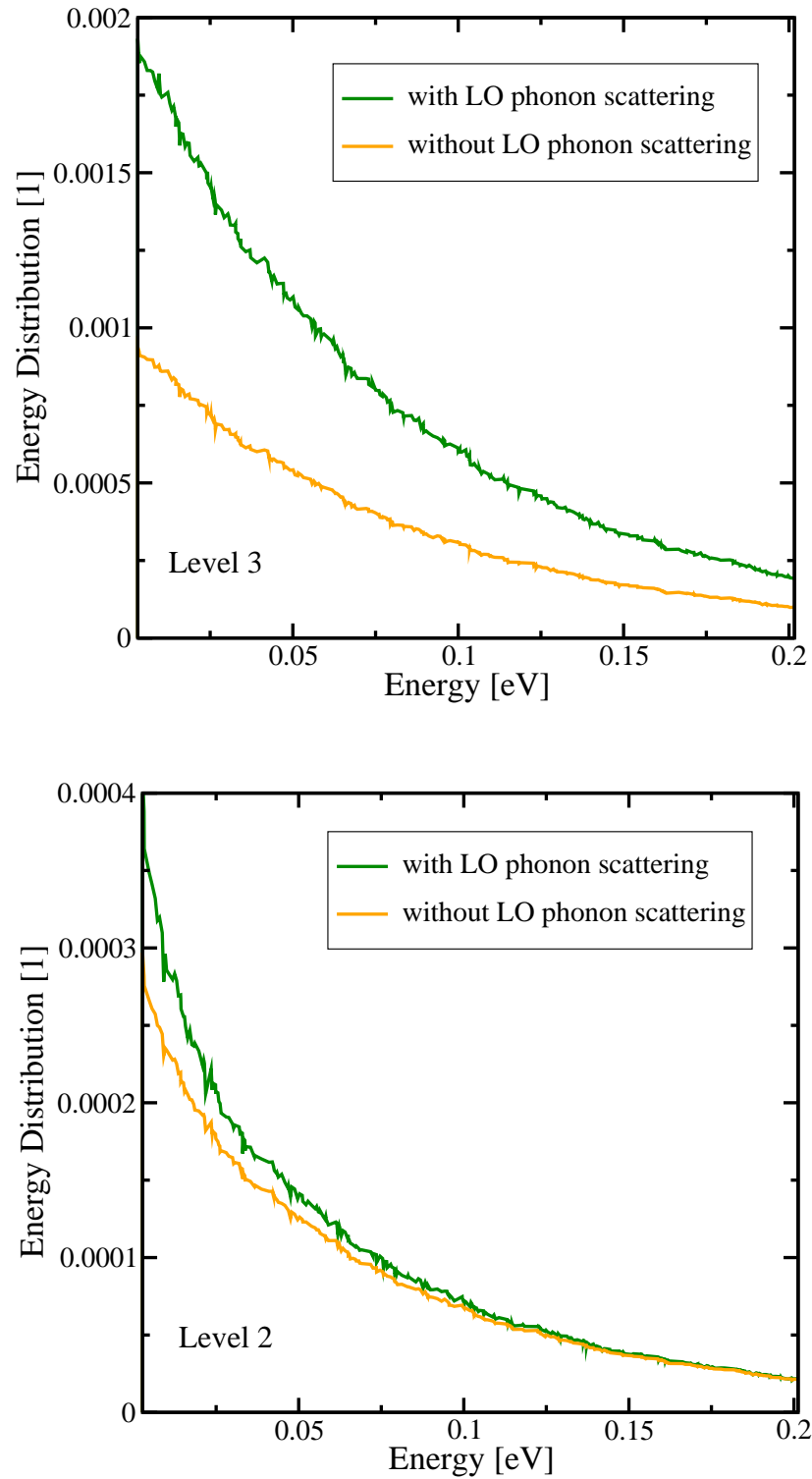


Figure 6.27: Energy distributions of the upper and lower laser level with and without taking into account polar optical phonon scattering.

6.2.3.3 Inclusion of Alloy Scattering

The comparison between the calculated and the measured current density suggests that there are also other important mechanisms which should be considered in order to get more realistic results.

Figure 6.28 shows the calculated voltage-current characteristics when the alloy scattering is included in the simulation which is performed at 78 K. Due to its significant effect on the simulation results, the comparison with the experimental measurements gets sensitively better. In the following, we will investigate the impact of alloy scattering for higher temperatures. Table 6.5 shows the temperature dependence of the band gap energies of $\text{In}_{0.53}\text{Ga}_{0.47}\text{As}$ and $\text{GaAs}_{0.51}\text{Sb}_{0.49}$ as well as the conduction band discontinuity [4]. Figure 6.29 illustrates the effect of the alloy scattering mechanism in dependence on the temperature. This scattering mechanism is mostly dominant at low temperatures, and somewhat weaker at high temperatures. This circumstance is also depicted in Figure 6.30. The ratio of the calculated current densities with and without taking into account alloy scattering is shown. We conclude that the alloy scattering mechanism is necessary to be considered in transport modeling of QCLs, especially in the low temperature region.

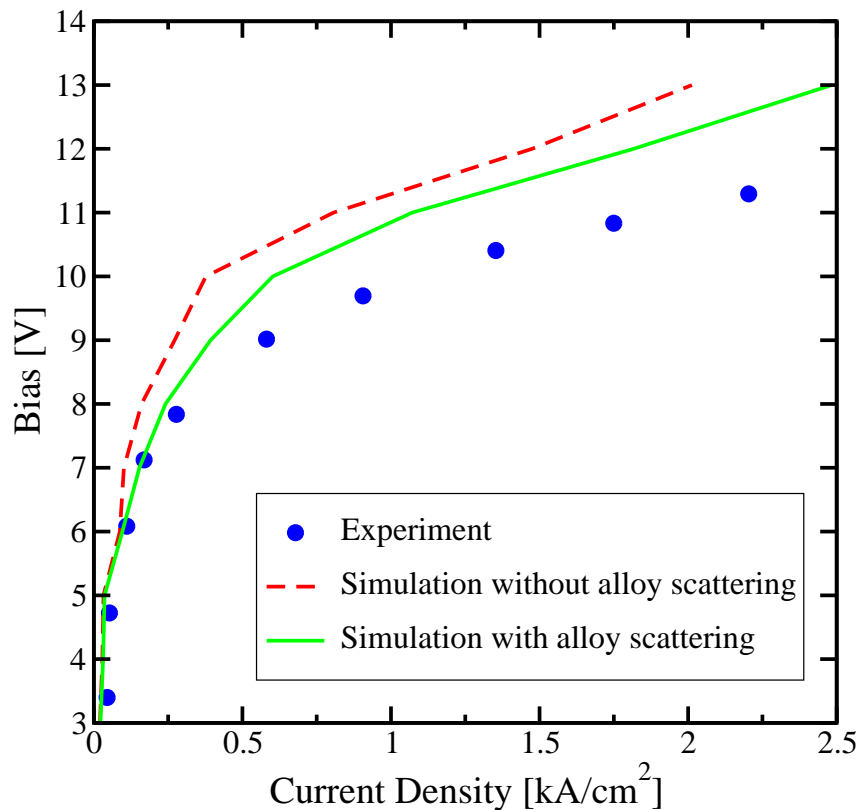


Figure 6.28: Voltage-current characteristics at 78 K. Comparison between the measured values and the simulation results with and without alloy scattering.

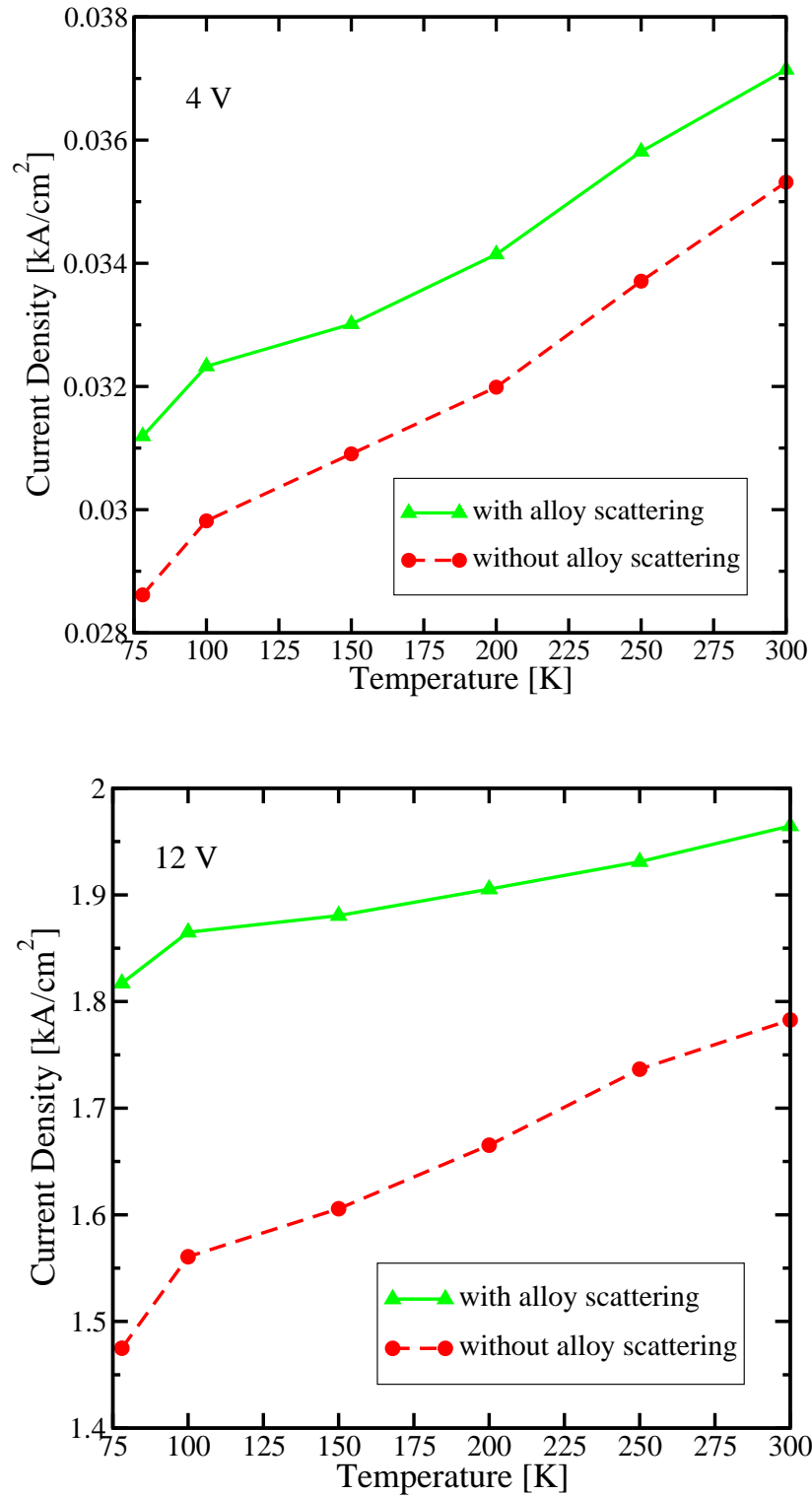


Figure 6.29: Current density versus temperature at 5 V and 13 V with and without alloy scattering.

T [K]	$E_g(\text{In}_{0.53}\text{Ga}_{0.47}\text{As})$ [eV]	$E_g(\text{GaAs}_{0.51}\text{Sb}_{0.49})$ [eV]	ΔE_c [eV]
78	0.7756	0.7869	0.1613
100	0.7723	0.7820	0.1597
150	0.7649	0.7739	0.1590
200	0.7507	0.7590	0.1583
250	0.7360	0.7412	0.1552
300	0.7209	0.7237	0.1528

Table 6.5: Temperature dependence of band gap energies and conduction band discontinuities [4].

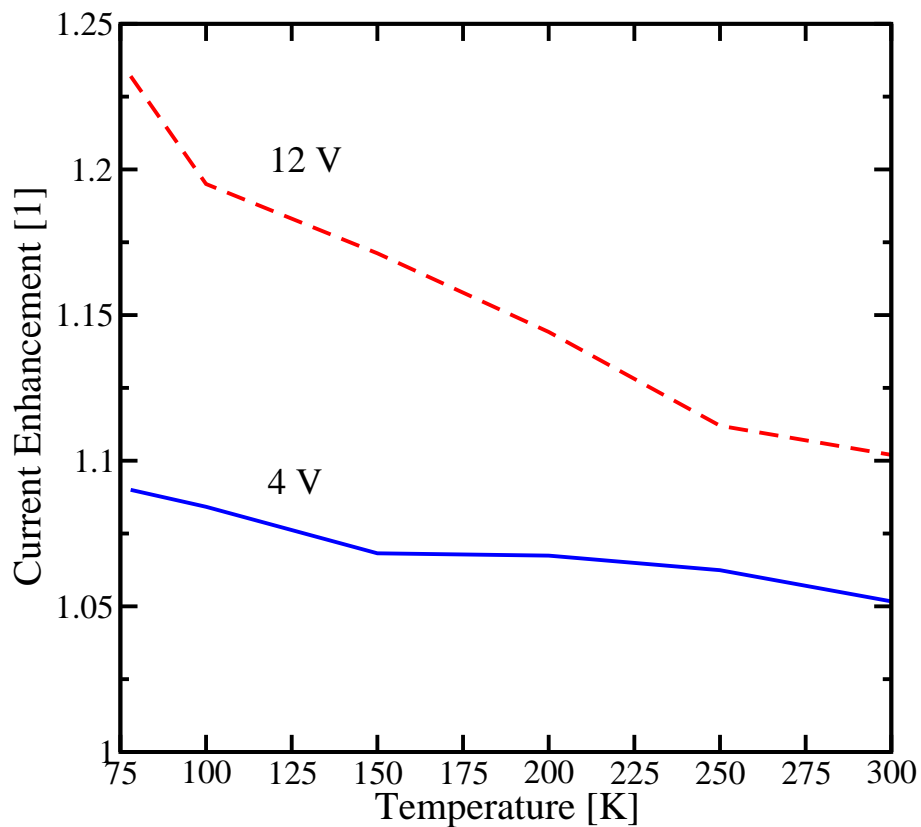


Figure 6.30: Current enhancement due to inclusion of alloy scattering for several temperatures.

Chapter 7

Summary and Outlook

A detailed introduction into fundamental transport models was presented, especially the quantum ballistic transport and the density matrix formulation. Special focus was laid on the semiclassical transport model and the stationary charge transport described by the PME.

Thereafter, we presented numerical solutions of the Schrödinger equation based on Robin boundary conditions in order to obtain current carrying states. Special attention has been turned to calculations of the fundamental quantities like the tunneling current density. The method has been applied to several heterostructure designs and the determined results have been compared to simulations using nonequilibrium Greens functions and the TsuEsaki model and also experimental measurements. Good numerical agreement has been obtained. In addition, we have investigated the asymptotic behavior of the wave functions. A proof that the solution of the Robin problem converges to the solution of the Dirichlet problem has been presented. This behavior has been also illustrated numerically by comparing simulated wave functions as well as the dipole matrix elements of the Robin and Dirichlet boundary value problems in situations with high energy levels. It has been shown that the tunneling current vanishes with decreasing electric field, which can be explained in terms of the transmission coefficient. The presented results indicate the necessity to treat QCLs as open quantum systems with non-selfadjoint boundary conditions.

In this thesis, I have described a semi-classical approach to model transport in QCLs. Over the course of this work, a simulator has been developed which solves the PME by means of a Monte Carlo method. As a prototypical example, we simulated a GaAs based QCL in the THz region. We have investigated the current density in dependence of the applied bias, and the electron distribution functions of the individual subbands have been computed. In general, it is demonstrated that the developed Monte Carlo simulator is an efficient approach for simulating stationary charge transport in quantum cascade structures governed by the PME. Special focus was laid on the study of intervalley

scattering effects on the carrier dynamics. In particular, the simulation results indicate that the Γ -X electron transfer plays a considerable role and highlights the importance of intervalley charge transport for QCL design considerations. It has been shown that the modification of the Al content and the width of the collector barrier in a GaAs/AlGaAs QCL can yield a significant increase in current density when considering Γ -X intervalley scattering. This can be explained by an increase of the overlap between the upper X-state and the lower Γ -state of two adjacent stages, which is particularly important for QCL design considerations. Finally, a comparison of simulation results with measurements for a recently developed InGaAs/GaAsSb QCL has been presented. We were able to observe dominant impact due to optical phonon scattering and also a non negligible effect due to alloy scattering.

However, more remains to be done for future research. A large number of states are involved in transport, especially for THz QCLs. Subbands are close in energy and strongly coupled by Coulomb scattering which can play an important role [130]. For more precise simulations, a model for electron-electron scattering has to be added. Moreover, the semi-classical picture is accurate only for strong coupling and the Boltzmann-like formalism is sufficient for stationary states, but phase coherent phenomena are disregarded. The scattering induced phase coherence can be described by a density matrix formulation of the quantum transport theory. Hence, it will be important to incorporate the subband dependent dephasing which can yield a more accurate description of the electron transport. Furthermore, the parameters of InGaAs based material systems are not well characterized. This may be significant when adapting the Monte Carlo simulator to InGaAs based QCLs, which requires careful attention.

Appendix

A Derivation of the Effective Mass Equation

In order to derive the effective mass theory it is imperative to formulate the envelope function method. In the envelope function approximation, the electron wave functions can be expressed by

$$\Psi(\mathbf{x}) = \sum_{\nu} \Psi_{\nu, \mathbf{k}_{\parallel}}(\mathbf{x}) = \frac{1}{\sqrt{A}} e^{i\mathbf{k}_{\parallel} \cdot \mathbf{x}_{\parallel}} \sum_{\nu} \Phi_{\nu}(z) U_{\nu}(\mathbf{x}) \quad (7.1)$$

where ν is the index of the envelope function Φ_{ν} and the corresponding Bloch function U_{ν} . This definition of the expansion is identical to the one given by Luttinger and Kohn [38]. Exact equations for the envelope functions Φ_{ν} can be derived by inserting the envelope function expansion (7.1) into the Schrödinger equation of the form

$$\hat{H}\Psi(\mathbf{x}) = (\hat{T} + \hat{V}(\mathbf{x}))\Psi(\mathbf{x}) = E\Psi(\mathbf{x}) \quad (7.2)$$

By applying the abbreviation $\tilde{U}_{\nu}(\mathbf{x}) = \frac{1}{\sqrt{A}} e^{i\mathbf{k}_{\parallel} \cdot \mathbf{x}_{\parallel}} U_{\nu}(\mathbf{x})$, the kinetic energy term can be written as

$$\hat{T}\Psi = -\frac{\hbar^2}{2m_0} \sum_{\nu} \left[(\nabla^2 \Phi_{\nu}) \tilde{U}_{\nu} + 2(\nabla \Phi_{\nu}) \cdot (\nabla \tilde{U}_{\nu}) + \Phi_{\nu} \nabla^2 \tilde{U}_{\nu} \right] \quad (7.3)$$

Due to the completeness of the \tilde{U}_{ν}

$$\sum_{\nu} \tilde{U}_{\nu}^* \tilde{U}_{\nu} = \mathbf{1} \quad (7.4)$$

the functions $\nabla \tilde{U}_{\nu}$ and $\nabla^2 \tilde{U}_{\nu}$ can be expressed in terms of the matrix elements of the kinetic energy and momentum with respect to the \tilde{U}_{ν}

$$\hat{T}\Psi = \sum_{\nu} \left[-\frac{\hbar^2}{2m_0} (\nabla^2 \Phi_{\nu}) + \sum_{\nu'} \frac{(-i\hbar)}{m} p_{\nu\nu'} \cdot \nabla \Phi_{\nu'} + \sum_{\nu'} \hat{T}_{\nu\nu'} \Phi_{\nu'} \right] \tilde{U}_{\nu} \quad (7.5)$$

where

$$\begin{aligned} p_{\nu\nu'} &= \int \tilde{U}_{\nu'} p \tilde{U}_{\nu} d^3\mathbf{x} \\ \hat{T}_{\nu\nu'} &= \int \tilde{U}_{\nu'} \hat{T} \tilde{U}_{\nu} d^3\mathbf{x} \end{aligned}$$

Equating coefficients of \tilde{U}_{ν} on both sides of equation (7.2) yields

$$-\frac{\hbar^2}{2m_0}(\nabla^2\Phi_{\nu}) + \sum_{\nu'} \frac{(-i\hbar)}{m_0} p_{\nu\nu'} \cdot \nabla\Phi_{\nu'} + \sum_{\nu'} \hat{H}_{\nu\nu'} \Phi_{\nu'} = E\Phi_{\nu} \quad (7.6)$$

where $\hat{H}_{\nu\nu'}$ denote the corresponding matrix elements of the Hamiltonian.

The elimination of “small“ envelope functions in favour of the dominant ones is the crucial point in the derivation of the effective mass equation from the envelope function equations. The slowly varying envelope functions are divided into two groups S and R. The functions belonging to the group R ($\Phi_r, \Phi_{r'}$, etc.) are small and thus eliminated approximately in favour of the dominant functions which are members of the group S ($\Phi_s, \Phi_{s'}$, etc.). For the slowly varying envelope functions, one gets approximately

$$\Phi_r = (E - \hat{H}_{rr})^{-1} \sum_{s'} \left(\frac{(-i\hbar)}{m_0} p_{rs'} \cdot \nabla\Phi_{s'} + \hat{H}_{rs'} \Phi_{s'} \right) \quad (7.7)$$

Substituting this expression for Φ_r in equation (7.6), we obtain

$$\begin{aligned} E\Phi_s &= -\frac{\hbar^2}{2m_0} \sum_{s'} \nabla \cdot [\gamma_{ss'} \cdot \nabla\Phi_{s'}] + \sum_{s'} \frac{(-i\hbar)}{m_0} p_{ss'} \cdot \nabla\Phi_{s'} + \sum_{s'} \hat{H}_{ss'}^{(2)} \Phi_{s'} \\ &+ \sum_{s'r} \frac{(-i\hbar)}{m_0} p_{sr} \cdot \nabla[(E - \hat{H}_{rr})^{-1} \hat{H}_{rs'}] \Phi_{s'} \\ &+ \sum_{s'r} \frac{(-i\hbar)}{m_0} (E - \hat{H}_{rr})^{-1} (p_{sr} \hat{H}_{rs'} + \hat{H}_{sr} p_{rs'}) \cdot \nabla\Phi_{s'} \end{aligned} \quad (7.8)$$

where

$$\gamma_{ss'} = \mathbf{1}\delta_{ss'} + \frac{2}{m_0} \sum_r p_{sr} [E - \hat{H}_{rr}]^{-1} p_{rs'} \quad (7.9)$$

and

$$\hat{H}_{ss'}^{(2)} = \hat{H}_{ss'} + \sum_r \hat{H}_{sr} [E - \hat{H}_{rr}]^{-1} \hat{H}_{rs'} \quad (7.10)$$

Neglecting interface contributions to the effective Hamiltonian, \hat{H}_{rr} and $\hat{H}_{rs'}$ are considered to be constant and the gradient of $(E - \hat{H}_{rr})^{-1} \hat{H}_{rs'}$ vanishes. Thus, the fourth term on the r.h.s of equation (7.8) is zero. Considering the case of conduction band states, the energy is close to the conduction band edge and the envelope functions corresponding to the conduction band-like basis states \tilde{U}_c are expected to be dominant. For such an

approximation, \tilde{U}_c is chosen to be a reasonable approximation to the conduction band minimum wavefunction of each constituent material [131]. Hence, \tilde{U}_c corresponds to a band extremum and the momentum matrix $p_{ss'}$ has only one element p_{cc} which is zero. The fifth term of equation (7.8) becomes

$$\sum_r \frac{(-i\hbar)}{m_0} (E - \hat{H}_{rr})^{-1} (p_{cr} \hat{H}_{rc} + \hat{H}_{cr} p_{rc}) \cdot \nabla \Phi_c \quad (7.11)$$

This term will be neglected, since it is dominated by the interface parts of the Hamiltonian. Hence, the effective mass equation reads

$$-\frac{\hbar^2}{2} \nabla \cdot \left(\frac{1}{m_c(E)} \nabla \Phi_c \right) + \hat{H}_{cc}^{(2)} \Phi_c = E \Phi_c \quad (7.12)$$

where $\hat{H}_{cc}^{(2)}$ denotes the effective band edge profile and the effective mass $m_c(E)$ is defined by

$$\frac{m_0}{m_c(E)} = 1 + \frac{2}{m_0} \sum_r p_{cr} [E - \hat{H}_{rr}]^{-1} p_{rc} \quad (7.13)$$

B Derivation of the Scattering Rates

B.1 Polar Optical Phonon Scattering

The envelope function is given by

$$\Psi_{\nu\lambda, \mathbf{k}_{\parallel}}^{\eta}(\mathbf{x}) = \frac{1}{\sqrt{A}} e^{i\mathbf{k}_{\parallel} \cdot \mathbf{x}_{\parallel}} \Phi_{\nu\lambda}^{\eta}(z)$$

According to the hermitian interaction Hamiltonian described in 5.3, the Hamiltonian matrix elements of the electron-phonon interaction are as follows

$$\begin{aligned} \langle \alpha', \mathbf{k}'_{\parallel} | \hat{H}_{\text{e-ph}}^{\text{LO}} | \alpha, \mathbf{k}_{\parallel} \rangle &= \alpha_{\text{LO}} \int \Psi_{\alpha', \mathbf{k}'_{\parallel}}^{\star}(\mathbf{x}) e^{i\mathbf{q} \cdot \mathbf{x}} \Psi_{\alpha, \mathbf{k}_{\parallel}}(\mathbf{x}) d\mathbf{x} + \text{c.c} \\ &= \alpha_{\text{LO}} \int \frac{1}{L_x} e^{-i(k_x - q_x - k'_x)x} dx \int \frac{1}{L_y} e^{-i(k_y - q_y - k'_y)y} dy \\ &\quad \times \int \Phi_{\alpha'}^{\star}(z) e^{iq_z z} \Phi_{\alpha}(z) dz a_q + \text{c.c} \\ &= \alpha_{\text{LO}} \delta_{\mathbf{k}'_{\parallel}, \mathbf{k}_{\parallel} - \mathbf{q}_{\parallel}} \int \Phi_{\alpha'}^{\star}(z) e^{iq_z z} \Phi_{\alpha}(z) dz + \text{c.c} \end{aligned}$$

The scattering rate can be calculated by integrating the transition probability over all possible \mathbf{k}'_{\parallel} according to

$$\begin{aligned} \frac{1}{\tau_{\alpha'}^{\alpha}(\mathbf{k}_{\parallel})} &= \frac{A}{(2\pi)^2} \int S_{\alpha}^{\alpha'}(\mathbf{k}_{\parallel}, \mathbf{k}'_{\parallel}) d\mathbf{k}'_{\parallel} \\ &= C_{\text{LO}}^{\pm} \int dq_z \int d\mathbf{k}'_{\parallel} |F_{\alpha'}^{\alpha}(q_z)|^2 \frac{1}{(\mathbf{k}_{\parallel} - \mathbf{k}'_{\parallel})^2 + q_z^2} \delta(E_{\alpha'}(\mathbf{k}'_{\parallel}) - E_{\alpha}(\mathbf{k}_{\parallel}) \mp \hbar\omega_{\text{LO}}) \end{aligned}$$

where

$$F_{\nu'\lambda'}^{\nu\lambda}(q_z) = \int dz \Phi_{\nu'\lambda'}^{\star}(z) \Phi_{\nu\lambda}(z) e^{iq_z z}$$

and $C_{\text{LO}}^{\pm} = e^2 \omega_{\text{LO}} (\varepsilon_{\infty}^{-1} - \varepsilon_S^{-1}) (N_{\text{LO}} + 1/2 \pm 1/2) / 4\pi$. Due to the energy conservation

$$E_{\alpha'}(\mathbf{k}'_{\parallel}) = E_{\alpha}(\mathbf{k}_{\parallel}) \pm \hbar\omega_{\text{LO}}$$

one gets

$$k'_{\parallel}{}^2 = k_{\parallel}^2 + \underbrace{\frac{2m^{\star}}{\hbar^2} (E_{\alpha} - E_{\alpha'} \pm \hbar\omega_{\text{LO}})}_{(Q_{\alpha'}^{\alpha})_{\pm}}$$

Making use of $k'_{\parallel} dk'_{\parallel} = m^{\star} / \hbar^2 dE'$, the scattering rate can be written as

$$\begin{aligned} \frac{1}{\tau_{\alpha'}^{\alpha}(\mathbf{k}_{\parallel})} &= C_{\text{LO}}^{\pm} \int dq_z \int_{-\pi}^{\pi} d\theta \int dE' \frac{m^{\star}}{\hbar^2} |F_{\alpha'}^{\alpha}(q_z)|^2 \frac{\delta(E_f - E')}{k_{\parallel}^2 - 2k_{\parallel} k_{\parallel}(E') \cos \theta + k_{\parallel}(E')^2 + q_z^2} \\ &= C_{\text{LO}}^{\pm} \int dq_z \int_{-\pi}^{\pi} d\theta \frac{m^{\star}}{\hbar^2} |F_{\alpha'}^{\alpha}(q_z)|^2 \frac{1}{k_{\parallel}^2 - 2k_{\parallel} k_{\parallel}^f \cos \theta + k_{\parallel}^f{}^2 + q_z^2} \end{aligned}$$

With the transformation

$$\cos \theta = \frac{1-t^2}{1+t^2}, \quad d\theta = \frac{2}{1+t^2} dt$$

we get

$$\begin{aligned} \frac{1}{\tau_{\alpha'}^{\alpha'}(\mathbf{k}_{\parallel})} &= C_{\text{LO}}^{\pm} \int dq_z \int_{-\infty}^{+\infty} dt \frac{m^*}{\hbar^2} |F_{\alpha'}^{\alpha'}(q_z)|^2 \frac{1}{k_{\parallel}^2 + k_{\parallel}^{f2} - 2k_{\parallel} k_{\parallel}^f + q_z^2 + t^2(k_{\parallel}^2 + k_{\parallel}^{f2} + 2k_{\parallel} k_{\parallel}^f + q_z^2)} \\ &= \frac{m^* \pi}{\hbar^2} C_{\text{LO}}^{\pm} \int dq_z |F_{\alpha'}^{\alpha'}(q_z)|^2 \frac{1}{\sqrt{[q_z^2 + (k_{\parallel} - k_{\parallel}^f)^2] [q_z^2 + (k_{\parallel} + k_{\parallel}^f)^2]}} \end{aligned}$$

Finally, by taking into account the energy balance for the required emission and absorption processes, the result is

$$\begin{aligned} \frac{1}{\tau_{\alpha'}^{\alpha'}(\mathbf{k}_{\parallel})} &= \frac{e^2 \hbar \omega_{\text{LO}} m_{\alpha'}^*}{4 \hbar^3} \left(\frac{1}{\varepsilon_{\infty}} - \frac{1}{\varepsilon_S} \right) \left(N_{\text{LO}} + \frac{1}{2} \mp \frac{1}{2} \right) \int dq_z \frac{|F_{\alpha'}^{\alpha'}(q_z)|^2}{q_z^4 + (Q_{\alpha'}^{\alpha'})_{\pm}^4 + 2q_z^2 [2k_{\parallel}^2 \pm (Q_{\alpha'}^{\alpha'})_{\pm}^2]} \\ &\quad \times \Theta(E_{\alpha}(\mathbf{k}_{\parallel}) - E_{\alpha'} \pm \hbar \omega_{\text{LO}}) \end{aligned} \tag{7.14}$$

B.2 Acoustic Deformation Potential Scattering

Here, we consider the elastic approximation ($\hbar\omega = 0$). For longitudinal phonons, the polarization vector is

$$\mathbf{w} = \frac{\mathbf{q}}{q}$$

Thus, the interaction Hamiltonian is given by

$$\hat{H}_{\text{e-ph}}^{\text{AC}} = \sum_q iq \Xi_{ac} \sqrt{\frac{\hbar}{2V\rho\omega_q}} (\hat{a}_q e^{i\mathbf{q}\cdot\mathbf{x}} + \hat{a}_q^{\dagger} e^{-i\mathbf{q}\cdot\mathbf{x}}) \tag{7.15}$$

In the occupation number representation, the matrix element reads

$$\begin{aligned} \langle \alpha', \mathbf{k}'_{\parallel} | \langle n'_{\mathbf{q}} | \hat{H}_{\text{e-ph}}^{\text{AC}} | n_{\mathbf{q}} \rangle | \alpha, \mathbf{k}_{\parallel} \rangle &= \langle \alpha', \mathbf{k}'_{\parallel} | \sum_q q \Xi_{ac} \sqrt{\frac{\hbar}{2V\rho\omega_q}} e^{i\mathbf{q}\cdot\mathbf{x}} \langle n'_{\mathbf{q}} | \hat{a}_q | n_{\mathbf{q}} \rangle | \alpha, \mathbf{k}_{\parallel} \rangle \\ &\quad + \langle \alpha', \mathbf{k}'_{\parallel} | \sum_q q \Xi_{ac} \sqrt{\frac{\hbar}{2V\rho\omega_q}} e^{-i\mathbf{q}\cdot\mathbf{x}} \langle n'_{\mathbf{q}} | \hat{a}_q^{\dagger} | n_{\mathbf{q}} \rangle | \alpha, \mathbf{k}_{\parallel} \rangle \end{aligned}$$

Since

$$\begin{aligned} \langle n'_{\mathbf{q}} | \hat{a}_q | n_{\mathbf{q}} \rangle &= \sqrt{n_{\mathbf{q}}} \langle n'_{\mathbf{q}} | n_{\mathbf{q}} - 1 \rangle = \sqrt{n_{\mathbf{q}}} \delta_{n'_{\mathbf{q}}, n_{\mathbf{q}}-1} \\ \langle n'_{\mathbf{q}} | \hat{a}_q^{\dagger} | n_{\mathbf{q}} \rangle &= \sqrt{n_{\mathbf{q}} + 1} \langle n'_{\mathbf{q}} | n_{\mathbf{q}} + 1 \rangle = \sqrt{n_{\mathbf{q}} + 1} \delta_{n'_{\mathbf{q}}, n_{\mathbf{q}}+1} \end{aligned}$$

one gets

$$\begin{aligned} \langle \alpha', \mathbf{k}'_{\parallel} | \langle n'_{\mathbf{q}} | \hat{H}_{e\text{-ph}}^{\text{AC}} | n_{\mathbf{q}} \rangle | \alpha, \mathbf{k}_{\parallel} \rangle &= q \Xi_{ac} \sqrt{\frac{\hbar}{2V \rho \omega_q}} \sqrt{n_{\mathbf{q}}} F_{\alpha'}^{\alpha}(q_z) \delta_{\mathbf{k}_{\parallel} + \mathbf{q}_{\parallel}, \mathbf{k}'_{\parallel}} \\ &+ q \Xi_{ac} \sqrt{\frac{\hbar}{2V \rho \omega_q}} \sqrt{n_{\mathbf{q}} + 1} F_{\alpha'}^{\alpha}(q_z) \delta_{\mathbf{k}_{\parallel} - \mathbf{q}_{\parallel}, \mathbf{k}'_{\parallel}} \end{aligned}$$

Taking into account the following dispersion relation

$$\frac{\omega_q}{q} = v_s$$

Under the assumption that the phonon energy is much smaller than the thermal energy ($\hbar\omega_q \ll k_B T$), the Bose-Einstein relation can be approximated according to

$$n_{\mathbf{q}} = \frac{1}{e^{\hbar\omega_q/k_B T} - 1} \approx n_{\mathbf{q}} + 1 \approx \frac{k_B T}{\hbar\omega_q}$$

Due to this approximation, the absorption and emission terms are the same and the scattering rate becomes

$$\begin{aligned} \frac{1}{\tau_{\alpha'}^{\alpha}(\mathbf{k}_{\parallel})} &= \frac{V}{2\pi\hbar} \int dz |\Phi_{\alpha}(z)|^2 |\Phi_{\alpha'}(z)|^2 \int d\mathbf{k}'_{\parallel} \Xi_{ac}^2 \frac{k_B T}{2V \rho v_s^2} \delta(E_{\alpha}(\mathbf{k}_{\parallel}) - E_{\alpha'}(\mathbf{k}'_{\parallel})) \\ &= \frac{\Xi_{ac}^2 m_{\alpha'}^* k_B T}{\rho \hbar^3 v_s^2} I_{\alpha}^{\alpha'} \Theta(E_{\alpha}(\mathbf{k}_{\parallel}) - E_{\alpha'}) \end{aligned} \quad (7.16)$$

B.3 Optical Deformation Potential Scattering

The interaction Hamiltonian is given by

$$\hat{H}_{e\text{-ph}}^{\text{OP}} = \sum_q \Xi_{op} \sqrt{\frac{\hbar}{2V \rho \omega_q}} (\hat{a}_q e^{i\mathbf{q}\cdot\mathbf{x}} + \hat{a}_q^{\dagger} e^{-i\mathbf{q}\cdot\mathbf{x}}) \quad (7.17)$$

The calculation of the matrix elements is mainly the same as in the case of acoustic phonons, only the phonon energy is not equal zero. Thus

$$\begin{aligned} \langle \alpha', \mathbf{k}'_{\parallel} | \langle n'_{\mathbf{q}} | \hat{H}_{e\text{-ph}}^{\text{OP}} | n_{\mathbf{q}} \rangle | \alpha, \mathbf{k}_{\parallel} \rangle &= \Xi_{op} \sqrt{\frac{\hbar}{2V \rho \omega_q}} \sqrt{n_{\mathbf{q}}} F_{\alpha'}^{\alpha}(q_z) \delta_{\mathbf{k}_{\parallel} + \mathbf{q}_{\parallel}, \mathbf{k}'_{\parallel}} \\ &+ \Xi_{op} \sqrt{\frac{\hbar}{2V \rho \omega_q}} \sqrt{n_{\mathbf{q}} + 1} F_{\alpha'}^{\alpha}(q_z) \delta_{\mathbf{k}_{\parallel} - \mathbf{q}_{\parallel}, \mathbf{k}'_{\parallel}} \end{aligned}$$

$n_{\mathbf{q}}$ and ω_q are considered to be constant. The scattering rate for the absorption reads

$$\begin{aligned} \frac{1}{\tau_{\alpha'}^{\alpha}(\mathbf{k}_{\parallel})} \Big|_{\text{abs}} &= \frac{V}{2\pi\hbar} \int dz |\Phi_{\alpha}(z)|^2 |\Phi_{\alpha'}(z)|^2 \int d\mathbf{k}'_{\parallel} \Xi_{op}^2 \frac{\hbar}{2V \rho \omega_q} \sqrt{n_{\mathbf{q}}} \delta(E_{\alpha}(\mathbf{k}_{\parallel}) - E_{\alpha'}(\mathbf{k}'_{\parallel}) + \hbar\omega) \\ &= \frac{\Xi_{op}^2 m_{\alpha'}^*}{2\rho \hbar^2 \omega_q} I_{\alpha}^{\alpha'} n_{\mathbf{q}} \Theta(E_{\alpha}(\mathbf{k}_{\parallel}) - E_{\alpha'} + \hbar\omega) \end{aligned} \quad (7.18)$$

The emission term is treated analogously, which is

$$\frac{1}{\tau_{\alpha}^{\alpha'}(\mathbf{k}_{\parallel})}\Big|_{\text{ems}} = \frac{\Xi_{op}^2 m_{\alpha'}^*}{2\rho\hbar^2\omega_q} I_{\alpha}^{\alpha'} (n_{\mathbf{q}} + 1) \Theta(E_{\alpha}(\mathbf{k}_{\parallel}) - E_{\alpha'} - \hbar\omega) \quad (7.19)$$

B.4 Intervalley Scattering

The derivation of the intervalley scattering is formally the same as for the optical deformation potential scattering. The only difference is in the parameters in the prefactor of the interaction Hamiltonian which is given by

$$\hat{H}_{e\text{-ph}}^{\text{IV}} = \sum_q D_{\eta\eta'} \sqrt{\frac{Z_{\eta'} \hbar^2}{2V\rho E_{\eta\eta'}}} (\hat{a}_q e^{i\mathbf{q}\cdot\mathbf{x}} + \hat{a}_q^{\dagger} e^{-i\mathbf{q}\cdot\mathbf{x}}) \quad (7.20)$$

Hence, the calculation for the total scattering rate is totally analogous to the one done before and the result is

$$\frac{1}{\tau_{\alpha}^{\alpha'}(\mathbf{k}_{\parallel})} = \frac{Z_{\eta'} D_{\eta\eta'}^2 m_{\nu'\chi'}^{*\prime}}{2\hbar\rho E_{\eta\eta'}} \left(n_{\mathbf{q}} + \frac{1}{2} \mp \frac{1}{2} \right) I_{\alpha}^{\alpha'} \Theta(E_{\alpha}(\mathbf{k}) - E_{\alpha'} \pm E_{\eta\eta'}) \quad (7.21)$$

B.5 Interface Roughness Scattering

Within the interface roughness scattering, the electron is scattered elastically by terraces which are distributed at the interface. The corresponding potential at the interface can be written as [132]

$$V_{\text{IR}} = \frac{dV(z)}{dz} \text{rect}\left(\frac{z - z_I}{z_{R,I} - z_{L,I}}\right) \Delta(\mathbf{x}_{\parallel})$$

The function $\Delta(\mathbf{x}_{\parallel})$ describes the distribution of the terraces. The matrix element of V_{IR} is

$$\langle \alpha', \mathbf{k}'_{\parallel} | V_{\text{IR}} | \alpha, \mathbf{k}_{\parallel} \rangle = \underbrace{\int \Phi_{\alpha'}^*(z) \frac{dV}{dz} \text{rect}\left(\frac{z - z_I}{z_{R,I} - z_{L,I}}\right) \Phi_{\alpha}(z) dz}_{\varphi_{\alpha'\alpha,I}} \frac{1}{A} \underbrace{\int \Delta(\mathbf{x}_{\parallel}) e^{i(\mathbf{k}_{\parallel} - \mathbf{k}'_{\parallel}) \cdot \mathbf{x}_{\parallel}} d\mathbf{x}_{\parallel}}_{\langle \mathbf{k}'_{\parallel} | \Delta(\mathbf{x}_{\parallel}) | \mathbf{k}_{\parallel} \rangle}$$

where $\Delta(\mathbf{x}_{\parallel})$ can be represented as a superposition of square terraces [133]

$$\Delta(\mathbf{x}_{\parallel}) = \sum_t \text{rect}\left(\frac{\mathbf{x}_{\parallel} - \mathbf{x}_{\parallel}^t}{L_t}\right)$$

Here, \mathbf{x}_{\parallel}^t denotes the position of the terrace center and L_t the width of the terrace. The scattering of electrons by the roughness of interfaces is described by a distribution of

terraces present at the interface. The electrons scatter elastically by these terraces which are assumed to be of Gaussian type

$$\frac{1}{N_t} \sum_t \text{rect} \left(\frac{\mathbf{x}_{\parallel} - \mathbf{x}_{\parallel}^t}{L_t} \right) = \exp \left(-\frac{|\mathbf{x}_{\parallel}|^2}{2\sigma^2} \right) = N(\mathbf{x}_{\parallel})$$

Here, σ^2 is the average area of the terraces and N_t denotes the number of terraces in $A = L_x L_y$. Assuming that the cross-correlation between different terraces is zero, the autocorrelation function can be written as

$$\begin{aligned} \langle \Delta(\mathbf{x}_{\parallel}) \Delta(\mathbf{x}'_{\parallel}) \rangle &= \lim_{L_x \rightarrow \infty} \lim_{L_y \rightarrow \infty} \frac{1}{L_x L_y} \int_{-L_x/2}^{L_x/2} \int_{-L_y/2}^{L_y/2} \Delta(\mathbf{x}_{\parallel}) \Delta(\mathbf{x}'_{\parallel}) d\mathbf{x}_{\parallel} \\ &= \lim_{L_x \rightarrow \infty} \lim_{L_y \rightarrow \infty} \frac{N_t}{L_x L_y} \int_{-L_x/2}^{L_x/2} \int_{-L_y/2}^{L_y/2} N(\mathbf{x}_{\parallel}) N(\mathbf{x}_{\parallel}) d\mathbf{x}_{\parallel} \end{aligned}$$

Using the integral

$$\int_{-\infty}^{\infty} \exp \left[-\frac{(x - a/2)^2}{\sigma^2} \right] dx = \sqrt{\pi} \sigma \exp \left(-\frac{a^2}{4\sigma^2} \right)$$

yields

$$\langle \Delta(\mathbf{x}_{\parallel}) \Delta(\mathbf{x}'_{\parallel}) \rangle = \Delta^2 e^{-|\mathbf{x}_{\parallel} - \mathbf{x}'_{\parallel}|^2 / \Lambda^2} \quad (7.22)$$

with $\Delta^2 = N_t \pi \sigma^2 / A$ and $\Lambda = 2\sigma$. Except for the prefactor, this model is equivalent to the phenomenological one of Prange and Nee [134]. Assuming that $\Delta(\mathbf{x}_{\parallel})$ is a periodic function according to $\Delta(x, y) = \Delta(x + L_x, y + L_y)$, it can be expanded in a Fourier series

$$\Delta(\mathbf{x}_{\parallel}) = \sum_{\mathbf{q}_{\parallel}} \Delta_{\mathbf{q}_{\parallel}} e^{i\mathbf{q}_{\parallel} \cdot \mathbf{x}_{\parallel}}$$

where $\mathbf{q}_{\parallel} = \mathbf{k}_{\parallel} - \mathbf{k}'_{\parallel}$. The Fourier coefficient reads

$$\Delta_{\mathbf{q}_{\parallel}} = \langle \mathbf{k}'_{\parallel} | \Delta(\mathbf{x}_{\parallel}) | \mathbf{k}_{\parallel} \rangle = \frac{1}{A} \int_{-L_x/2}^{L_x/2} \int_{-L_y/2}^{L_y/2} e^{i(\mathbf{k}_{\parallel} - \mathbf{k}'_{\parallel}) \cdot \mathbf{x}_{\parallel}} \Delta(\mathbf{x}_{\parallel}) d\mathbf{x}_{\parallel}$$

Thus, the amplitude squared of the matrix element $\Delta(\mathbf{x}_{\parallel})$ is

$$|\Delta_{\mathbf{q}_{\parallel}}|^2 = \frac{1}{A^2} \int d\mathbf{x}_{\parallel} \int d\mathbf{x}'_{\parallel} e^{i(\mathbf{k}_{\parallel} - \mathbf{k}'_{\parallel}) \cdot (\mathbf{x}_{\parallel} - \mathbf{x}'_{\parallel})} \Delta(\mathbf{x}_{\parallel}) \Delta(\mathbf{x}'_{\parallel})$$

By means of equation (7.22), the ensemble average of this matrix element can be written as

$$\langle |\Delta_{\mathbf{q}_{\parallel}}|^2 \rangle = \frac{\Delta^2}{A^2} \int d\mathbf{x}_{\parallel} \int d\mathbf{x}'_{\parallel} e^{i(\mathbf{k}_{\parallel} - \mathbf{k}'_{\parallel}) \cdot (\mathbf{x}_{\parallel} - \mathbf{x}'_{\parallel})} e^{-|\mathbf{x}_{\parallel} - \mathbf{x}'_{\parallel}|^2 / \Lambda^2}$$

Using $\tilde{\mathbf{x}}_{\parallel} = \mathbf{x}_{\parallel} - \mathbf{x}'_{\parallel}$, and extending the integration limits to infinity, we get

$$\begin{aligned} \langle |\Delta_{\mathbf{q}_{\parallel}}|^2 \rangle &= \frac{\Delta^2}{A} \int_{-\infty}^{\infty} e^{-\tilde{x}_{\parallel}/\Lambda^2} e^{i\tilde{\mathbf{x}}_{\parallel} \cdot \mathbf{q}_{\parallel}} d\tilde{\mathbf{x}}_{\parallel} \\ &= \frac{\Delta^2}{A} \int_{-\infty}^{\infty} e^{-\tilde{x}_{\parallel,x}/\Lambda^2} e^{i\tilde{x}_{\parallel,x} q_{\parallel,x}} d\tilde{x}_{\parallel,x} \int_{-\infty}^{\infty} e^{-\tilde{x}_{\parallel,y}/\Lambda^2} e^{i\tilde{x}_{\parallel,y} q_{\parallel,y}} d\tilde{x}_{\parallel,y} \end{aligned}$$

Making use of the identity

$$\int_{-\infty}^{\infty} e^{-a^2 x^2} e^{i\xi x} dx = \frac{\sqrt{\pi}}{a} e^{-\xi^2/4a^2}$$

with $a^2 = 1/\Lambda^2$ and $\xi = q_{\parallel,y}$, the evaluated integrals are

$$\langle |\Delta_{\mathbf{q}_{\parallel}}|^2 \rangle = \frac{1}{A} \pi \Delta^2 \Lambda^2 e^{-q_{\parallel}^2 \Lambda^2/4} \quad (7.23)$$

Thus

$$\begin{aligned} \frac{1}{\tau_{\alpha'}^{\alpha'}(\mathbf{k}_{\parallel})} &= \frac{2\pi}{\hbar} \sum_{I, \mathbf{k}'_{\parallel}} |\langle \alpha', \mathbf{k}'_{\parallel} | V_{\text{IR}} | \alpha, \mathbf{k}_{\parallel} \rangle|^2 \delta(E_{\alpha'}(\mathbf{k}'_{\parallel}) - E_{\alpha}(\mathbf{k}_{\parallel})) \\ &= \frac{2\pi^2 \Delta^2 \Lambda^2}{\hbar A} \sum_{I, \mathbf{k}'_{\parallel}} |\varphi_{\alpha', \alpha, I}|^2 \delta(E_{\alpha'}(\mathbf{k}'_{\parallel}) - E_{\alpha}(\mathbf{k}_{\parallel})) \int_0^{\pi} e^{-(\mathbf{k}'_{\parallel} - \mathbf{k}_{\parallel})^2 \Lambda^2/4} d\theta \\ &= \frac{\pi \Delta^2 \Lambda^2}{\hbar} \sum_I |\varphi_{\alpha', \alpha, I}|^2 \int_0^{\pi} d\theta \int d\mathbf{k}'_{\parallel} d\mathbf{k}_{\parallel} e^{-(\mathbf{k}'_{\parallel} - \mathbf{k}_{\parallel})^2 \Lambda^2/4} \delta(E_{\alpha'}(\mathbf{k}'_{\parallel}) - E_{\alpha}(\mathbf{k}_{\parallel})) \end{aligned} \quad (7.24)$$

B.6 Alloy Scattering

Using the abbreviation $\delta V_{AB}(\mathbf{x}_{\parallel})$ and assuming that it can be approximated by an impulse function $\delta(\mathbf{x}_{\parallel})$ according to

$$\delta V_{AB}(\mathbf{x}_{\parallel}) = \Omega_0 \Delta V_{AB} \delta(\mathbf{x}_{\parallel})$$

the correlation function can be expressed in the following form

$$\begin{aligned} \langle \delta V(\mathbf{x}_{\parallel}) \delta V(\mathbf{x}'_{\parallel}) \rangle &= \lim_{A \rightarrow \infty} \frac{1}{A} \int \delta V(\mathbf{x}_{\parallel}) \delta V(\mathbf{x}'_{\parallel}) d\mathbf{x}'_{\parallel} \\ &= \lim_{A \rightarrow \infty} \frac{1}{A} \left[\sum_{\mathbf{x}_A} (1-x)^2 \delta(\mathbf{x}_{\parallel} - \mathbf{x}'_{\parallel}) \Omega_0^2 \Delta V_{AB}^2 + \sum_{\mathbf{x}_B} x^2 \delta(\mathbf{x}_{\parallel} - \mathbf{x}'_{\parallel}) \Omega_0^2 \Delta V_{AB}^2 \right] \end{aligned}$$

where ΔV_{AB} denotes the conduction band discontinuity between the crystals AC and BC. Considering that there is a fraction x at the \mathbf{X}_A sites and $(1-x)$ at the \mathbf{X}_B sites, the correlation function can be rewritten as

$$\begin{aligned}\langle \delta V(\mathbf{x}_{\parallel}) \delta V(\mathbf{x}'_{\parallel}) \rangle &= \lim_{A \rightarrow \infty} \frac{1}{A} \Omega_0^2 \Delta V_{AB}^2 \delta(\mathbf{x}_{\parallel} - \mathbf{x}'_{\parallel}) \left[x \frac{A}{\Omega_0} (1-x)^2 + (1-x) \frac{A}{\Omega_0} x^2 \right] \\ &= \Omega_0 \Delta V_{AB}^2 x(1-x) \delta(\mathbf{x}_{\parallel} - \mathbf{x}'_{\parallel})\end{aligned}$$

Under the assumption that $\delta V(\mathbf{x}_{\parallel})$ is periodic, it can be expanded in a Fourier series

$$\delta V(\mathbf{x}_{\parallel}) = \sum_{\mathbf{q}_{\parallel}} V_{\mathbf{q}_{\parallel}} e^{i\mathbf{q}_{\parallel} \cdot \mathbf{x}_{\parallel}} \quad (7.25)$$

Hence, the amplitude squared of the matrix element $\delta V(\mathbf{x}_{\parallel})$ is

$$\begin{aligned}|V_{\mathbf{q}_{\parallel}}|^2 &= |\langle \mathbf{k}'_{\parallel}, \alpha' | \delta V(\mathbf{x}_{\parallel}) | \mathbf{k}_{\parallel}, \alpha \rangle|^2 \\ &= \frac{1}{A^2} \int d\mathbf{x}_{\parallel} \int d\mathbf{x}'_{\parallel} e^{i(\mathbf{k}_{\parallel} - \mathbf{k}'_{\parallel}) \cdot (\mathbf{x}_{\parallel} - \mathbf{x}'_{\parallel})} \delta V(\mathbf{x}_{\parallel}) \delta V(\mathbf{x}'_{\parallel}) \int \Phi_{\alpha'}^*(z) \Phi_{\alpha}(z) dz\end{aligned}$$

Making use of the correlation function obtained previously, the ensemble average is given by

$$\begin{aligned}\langle |V_{\mathbf{q}_{\parallel}}|^2 \rangle &= \frac{1}{A^2} \int d\mathbf{x}_{\parallel} \int d\mathbf{x}'_{\parallel} e^{i(\mathbf{k}_{\parallel} - \mathbf{k}'_{\parallel}) \cdot (\mathbf{x}_{\parallel} - \mathbf{x}'_{\parallel})} \Omega_0 \Delta V_{AB}^2 x(1-x) \delta(\mathbf{x}_{\parallel} - \mathbf{x}'_{\parallel}) \int \Phi_{\alpha'}^*(z) \Phi_{\alpha}(z) dz \\ &= \Omega_0 \Delta V_{AB}^2 x(1-x) \int \Phi_{\alpha'}^*(z) \Phi_{\alpha}(z) dz\end{aligned}$$

Finally, the alloy scattering rate can be written as [135]

$$\begin{aligned}\frac{1}{\tau_{\alpha}^{\alpha'}} &= \frac{2\pi}{\hbar} \langle |V_{\mathbf{q}_{\parallel}}|^2 \rangle \rho_{\text{DOS}}^{2\text{D}} \int \Phi_{\alpha'}^*(z) \Phi_{\alpha}(z) dz \\ &= \frac{2m^*}{\hbar^3} \Omega_0 \Delta V_{AB}^2 x(1-x) \int \Phi_{\alpha'}^*(z) \Phi_{\alpha}(z) dz\end{aligned} \quad (7.26)$$

Bibliography

- [1] S. C. Lee, F. Banit, M. Woerner, and A. Wacker, “Quantum Mechanical Wavepacket Transport in Quantum Cascade Laser Structures,” *Phys. Rev. B*, vol. 73, no. 24, p. 245320, 2006.
- [2] C. Pfluegl, W. Schrenk, S. Anders, G. Strasser, C. Becker, C. Sirtori, Y. Bonetti, and A. Muller, “High-temperature Performance of GaAs-based Bound-to-continuum Quantum-cascade Lasers,” *Appl. Phys. Lett.*, vol. 83, no. 23, p. 4698, 2003.
- [3] M. Nobile, P. Klang, E. Mujagic, H. Detz, A. M. Andrews, W. Schrenk, and G. Strasser, “Quantum Cascade Laser utilising Aluminium-free Material System: InGaAs/GaAsSb Lattice-matched to InP,” *Electron. Lett.*, vol. 45, no. 20, p. 1031, 2009.
- [4] H. Detz, A. M. Andrews, M. Nobile, P. Klang, E. Mujagic, G. Hesser, W. Schrenk, F. Schäffler, and G. Strasser, “Intersubband Optoelectronics in the InGaAs/GaAsSb Material System,” *J. Vac. Sci. Technol. B*, vol. 28, no. 3, p. C3G19, 2010.
- [5] L. Esaki and R. Tsu, “Superlattice and Negative Differential Conductivity in Semiconductors,” *IBM J.Res.Dev.*, vol. 14, no. 1, p. 61, 1970.
- [6] R. F. Kazarinov and R. A. Suris, “Possibility of the Amplification of Electromagnetic Waves in a Semiconductor with a Superlattice,” *Sov. Phys. Semicond.*, vol. 5, no. 4, p. 707, 1971.
- [7] C. Gmachl, F. Capasso, D. L. Sivco, and A. Y. Cho, “Recent Progress in Quantum Cascade Lasers and Applications,” *Rep. Prog. Phys.*, vol. 64, p. 1533, 2001.
- [8] J. Faist, F. Capasso, D. L. Sivco, C. Sirtori, A. L. Hutchinson, and A. Y. Cho, “Quantum Cascade Laser,” *Science*, vol. 264, no. 5158, p. 553, 1994.
- [9] C. Sirtori, P. Kruck, S. Barbieri, P. Collot, J. Nagle, M. Beck, J. Faist, and U. Oesterle, “GaAs/AlGaAs Quantum Cascade Lasers,” *Appl. Phys. Lett.*, vol. 73, no. 24, p. 3486, 1998.

BIBLIOGRAPHY

- [10] C. Sirtori, H. Page, and C. Becker, "GaAs-based Quantum Cascade Lasers," *Phil. Trans. R. Soc. Lond. A*, vol. 359, p. 505, 2001.
- [11] P. J. Douglas, "Si/SiGe Heterostructures: From Material and Physics to Devices and Circuits," *Semicond. Sci. Technol.*, vol. 19, no. 10, p. R75, 2004.
- [12] A. Tredicucci, C. Gmachl, F. Capasso, A. L. Hutchinson, D. L. Sivco, and A. Y. Cho, "Single-mode Surface-plasmon Laser," *Appl. Phys. Lett.*, vol. 76, no. 16, p. 2164, 2000.
- [13] J. Faist, "Continuous-wave, Room-temperature Quantum Cascade Lasers," *Optics and Photonics News*, vol. 17, no. 5, p. 32, 2006.
- [14] A. A. Kosterev, F. K. Tittel, W. Durante, M. Allen, R. Koehler, C. Gmachl, F. Capasso, D. L. Sivco, and A. Y. Cho, "Detection of Biogenic CO Production above Vascular Cell Cultures using a Near-room-temperature QC-DFB Laser," *Appl. Phys. B: Lasers Opt.*, vol. 74, no. 1, p. 95, 2002.
- [15] R. F. Curl, F. Capasso, C. Gmachl, A. A. Kosterev, B. McManus, R. Lewicki, M. Pusharsky, G. Wysocki, and F. K. Tittel, "Quantum Cascade Lasers in Chemical Physics," *Chem. Phys. Lett.*, vol. 487, no. 1-3, p. 1, 2010.
- [16] C. Sirtori, F. Capasso, J. Faist, A. L. Hutchinson, D. L. Sivco, and A. Y. Cho, "Resonant Tunneling in Quantum Cascade Lasers," *IEEE J. Quantum Electron.*, vol. 34, no. 9, p. 1722, 1998.
- [17] Q. K. Yang and A. Z. Li, "Calculation of Spontaneous Emission and Gain Spectra for Quantum Cascade Lasers," *J. Phys.: Condens. Matter*, vol. 12, no. 8, p. 1907, 2000.
- [18] J. Faist, F. Capasso, C. Sirtori, D. L. Sivco, J. N. Baillargeon, A. L. Hutchinson, S. G. Chu, and A. Y. Cho, "High Power Mid-infrared ($\lambda \sim 5\mu\text{m}$) Quantum Cascade Lasers operating above Room Temperature," *Appl. Phys. Lett.*, vol. 68, no. 26, p. 3680, 1996.
- [19] C. Sirtori, J. Faist, F. Capasso, D. L. Sivco, A. L. Hutchinson, and A. Y. Cho, "Long Wavelength Infrared ($\lambda \sim 5\mu\text{m}$) Quantum Cascade Lasers," *Appl. Phys. Lett.*, vol. 69, no. 19, p. 2810, 1996.
- [20] J. Faist, C. Gmachl, F. Capasso, C. Sirtori, D. L. Sivco, J. N. Baillargeon, and A. Y. Cho, "Distributed Feedback Quantum Cascade Lasers," *Appl. Phys. Lett.*, vol. 70, no. 20, p. 2670, 1997.
- [21] G. Scamarcio, F. Capasso, C. Sirtori, J. Faist, A. L. Hutchinson, D. L. Sivco, and A. Y. Cho, "High-power Infrared (8-micrometer Wavelength) Superlattice Lasers," *Science*, vol. 276, no. 5313, p. 773, 1997.

BIBLIOGRAPHY

- [22] C. Sirtori, P. Kruck, S. Barbieri, H. Page, J. Nagle, M. Beck, J. Faist, and U. Oesterle, “Low-loss Al-free Waveguides for Unipolar Semiconductor Lasers,” *Appl. Phys. Lett.*, vol. 75, no. 25, p. 3911, 1999.
- [23] H. Page, C. Becker, A. Robertson, G. Glastre, V. Ortiz, and C. Sirtori, “300 K Operation of a GaAs-based Quantum-cascade Laser at $\lambda \approx 9\mu\text{m}$,” *Appl. Phys. Lett.*, vol. 78, no. 22, p. 3529, 2001.
- [24] S. Anders, W. Schrenk, E. Gornik, and G. Strasser, “Room-temperature Emission of GaAs/AlGaAs Superlattice Quantum-cascade Lasers at $\lambda \approx 12.6\mu\text{m}$,” *Appl. Phys. Lett.*, vol. 80, no. 11, p. 1864, 2002.
- [25] G. Scalari, N. Hoyler, M. Giovannini, and J. Faist, “Terahertz Bound-to-continuum Quantum-cascade Lasers based on Optical-phonon Scattering Extraction,” *Appl. Phys. Lett.*, vol. 86, no. 18, p. 181101, 2005.
- [26] H. Page, S. Dhillon, M. Calligaro, C. Becker, V. Ortiz, and C. Sirtori, “Improved CW Operation of GaAs-based QC Lasers: $T_{\text{max}} = 150\text{ K}$,” *IEEE J. Quantum Electron.*, vol. 40, no. 6, p. 665, 2004.
- [27] R. Colombelli, F. Capasso, C. Gmachl, A. L. Hutchinson, D. L. Sivco, A. Tredicucci, M. C. Wanke, A. M. Sergent, and A. Y. Cho, “Far-infrared Surface-plasmon Quantum-cascade Lasers at $21.5\mu\text{m}$ and $24\mu\text{m}$ Wavelengths,” *Appl. Phys. Lett.*, vol. 78, no. 18, p. 2620, 2001.
- [28] M. Beck, D. Hofstetter, T. Aellen, J. Faist, U. Oesterle, M. Illegems, E. Gini, and H. Melchior, “Continuous Wave Operation of a Mid-infrared Semiconductor Laser at Room Temperature,” *Science*, vol. 295, no. 5553, p. 301, 2002.
- [29] R. Koehler, A. Tredicucci, F. Beltram, H. E. Beere, E. H. Linfield, A. G. Davies, D. A. Ritchie, R. C. Iotti, and F. Rossi, “Terahertz Semiconductor-heterostructure Laser,” *Nature*, vol. 417, p. 156, 2002.
- [30] R. Maulini, M. Beck, J. Faist, and E. Gini, “Broadband Tuning of External Cavity Bound-to-continuum Quantum-cascade Lasers,” *Appl. Phys. Lett.*, vol. 84, no. 10, p. 1659, 2004.
- [31] M. Pushkarsky, A. Tsekoun, I. G. Dunayevskiy, R. Go, C. Kumar, and N. Patel, “Sub-parts-per-billion Level Detection of NO_2 using Room Temperature Quantum-cascade Lasers,” in *Proc. Natl. Acad. Sci. USA*, p. 10846, 2006.
- [32] N. Yu, Q. J. Wang, M. A. Kats, J. A. Fan, S. P. Khanna, L. Li, A. G. Davies, E. H. Linfield, and F. Capasso, “Designer Spoof Surface Plasmon Structures Collimate Terahertz Laser Beams,” *Nature Materials*, vol. 9, no. 9, p. 730, 2010.
- [33] A. Mueller and J. Faist, “Ready for Take-off,” *Nature Photonics*, vol. 4, p. 291, 2010.

BIBLIOGRAPHY

- [34] B. Lendl, M. Brandstetter, A. Genner, and W. Ritter, “Quantum Cascade Laser for Quantitative Analysis in Liquid Phase,” in *Proc. of the 38th FACSS Conference*, 2011.
- [35] M. George and J. Calladine, “Nanosecond Time-resolved IR Spectroscopy in Conventional and Supercritical Fluids Using External Cavity Quantum Cascade Lasers,” in *Proc. of the 38th FACSS Conference*, 2011.
- [36] A. Erlich, “Mid-infrared Absorption Spectroscopy using Quantum Cascade Lasers,” in *Proc. of the 38th FACSS Conference*, 2011.
- [37] F. Capasso, *Physics of Quantum Electron Devices*. Springer Series in Electronics and Photonics, 1990.
- [38] J. M. Luttinger and W. Kohn, “Motion of Electrons and Holes in Perturbed Periodic Fields,” *Phys. Rev.*, vol. 97, no. 4, p. 869, 1955.
- [39] M. G. Burt, “The Justification for Applying the Effective-mass Approximation to Microstructures,” *J. Phys.: Condens. Matter*, vol. 4, no. 32, p. 6651, 1992.
- [40] J. H. Davies, *The Physics of Low-dimensional Semiconductors: An Introduction*. Cambridge University Press, 1998.
- [41] B. J. BenDaniel and C. B. Duke, “Space-charge Effects on Electron Tunneling,” *Phys. Rev.*, vol. 152, no. 2, p. 683, 1966.
- [42] G. W. Hanson and A. B. Yakovlev, *Operator Theory for Electromagnetics: An Introduction*. Springer, 2001.
- [43] S. Selberherr, *Analysis and Simulation of Semiconductor Devices*. Springer Verlag, 1984.
- [44] S. L. Chuang, *Physics of Optoelectronic Devices*. Wiley Interscience, 1995.
- [45] E. J. Roan and S. L. Chuang, “Linear and Nonlinear Intersubband Electroabsorptions in a Modulation-doped Quantum Well,” *J. Appl. Phys.*, vol. 69, no. 5, p. 3249, 1991.
- [46] A. Trellakis, A. T. Galick, A. Pacelli, and U. Ravaioli, “Iteration Scheme for the Solution of the Two-dimensional Schrödinger-Poisson Equations in Quantum Structures,” *J. Appl. Phys.*, vol. 81, no. 12, p. 7880, 1997.
- [47] X. Gao, D. Botez, and I. Knezevic, “Phonon Confinement and Electron Transport in GaAs-based Quantum Cascade Structures,” *J. Appl. Phys.*, vol. 103, no. 7, p. 073101, 2008.
- [48] H.-C. Kaiser, H. Neidhardt, and J. Rehberg, “Density and Current of a Dissipative Schrödinger Operator,” *J. Math. Phys.*, vol. 43, no. 11, p. 5325, 2002.

BIBLIOGRAPHY

- [49] J. D. Bondurant and S. A. Fulling, “The Dirichlet-to-Robin Transform,” *J. Phys. A: Math. Gen.*, vol. 38, no. 7, p. 1505, 2005.
- [50] G. Milovanovic, O. Baumgartner, and H. Kosina, “On Open Boundary Conditions for Quantum Cascade Structures,” *Optical and Quantum Electronics*, vol. 41, no. 11, p. 921, 2009.
- [51] N. B. Abdallah, P. Degond, and P. A. Markowich, “On a One-dimensional Schrödinger-Poisson Scattering Model,” *ZAMP*, vol. 48, no. 1, p. 135, 2005.
- [52] E. Pozdeeva and A. Schulze-Halberg, “Trace Formula for Green’s Functions of Effective Mass Schrödinger Equations and Nth-order Darboux Transformations,” *Int. J. Mod. Phys. A*, vol. 23, no. 16-17, p. 2635, 2008.
- [53] L. P. Kadanoff and G. Baym, *Quantum Statistical Mechanics*. Benjamin, New York, 1962.
- [54] S. Datta, *Electronic Transport in Mesoscopic Systems*. Cambridge University Press, 1997.
- [55] S. Datta, *Quantum Transport: Atom to Transistor*. Cambridge University Press, 2005.
- [56] S. Datta, “The Non-equilibrium Green’s Function (NEGF) Formalism: An Elementary Introduction,” in *Proc. Digest. International Electron Devices Meeting IEDM ’02*, p. 703, 2002.
- [57] S. Datta, “Nanoscale Device Modeling: The Green’s Function Method,” *Superlattices & Microstructures*, vol. 28, no. 4, p. 253, 2000.
- [58] R. C. Iotti and F. Rossi, “Nature of Charge Transport in Quantum-cascade Lasers,” *Phys. Rev. Lett.*, vol. 87, no. 14, p. 146603, 2001.
- [59] S. Mukamel, *Principles of Nonlinear Optical Spectroscopy*. Oxford University Press, 1995.
- [60] M. F. Lensink, J. Mavri, and H. J. C. Berendsen, “Simultaneous Integration of Mixed Quantum-classical Systems by Density Matrix Evolution Equations using Interaction Representation and Adaptive Time Step Integrator,” *J. Comp. Chem.*, vol. 17, no. 11, p. 1287, 1995.
- [61] V. K. Thankappan, *Quantum Mechanics*. New Age International Ltd., 2003.
- [62] K. Blum, *Density Matrix Theory and Applications*. Plenum Press, 1996.
- [63] U. Fano, “Description of States in Quantum Mechanics by Density Matrix and Operator Techniques,” *Rev. Mod. Phys.*, vol. 29, no. 1, p. 74, 1957.
- [64] W. H. Louisell, *Quantum Statistical Properties of Radiation*. Wiley, New York, 1973.

BIBLIOGRAPHY

- [65] M. Sargent, M. O. Scully, and W. E. Lamb, *Laser Physics*. Addison-Wesley, New York, 1974.
- [66] K. Blum and H. Kleinpoppen, “Electron-photon Angular Correlation in Atomic Physics,” *Phys. Rep.*, vol. 52, no. 4, p. 203, 1979.
- [67] H. Haken, *Synergetics, an Introduction: Nonequilibrium Phase Transitions and Self-organization in Physics, Chemistry, and Biology*. Springer, New York, 1983.
- [68] M. Lundstrom, *Fundamentals of Carrier Transport*. Cambridge University Press (New York), 2000.
- [69] C. Kittel, *Introduction to Solid State Physics*. John Wiley & Sons, 1996.
- [70] H. Callebaut and Q. Hu, “Importance of Coherence for Electron Transport in Terahertz Quantum Cascade Lasers,” *J. Appl. Phys.*, vol. 98, no. 10, p. 104505, 2005.
- [71] L. V. Hove, “Quantum-mechanical Perturbations giving Rise to a Statistical Transport Equation,” *Physica*, vol. XXI, p. 517, 1955.
- [72] M. V. Fischetti, “Theory of Electron Transport in Small Semiconductor Devices using the Pauli Master Equation,” *J. Appl. Phys.*, vol. 83, no. 1, p. 270, 1998.
- [73] R. P. Zaccaria, R. C. Iotti, and F. Rossi, “Monte Carlo Simulation of Hot-carrier Phenomena in Open Quantum Devices: A Kinetic Approach,” *Appl. Phys. Lett.*, vol. 84, no. 1, p. 139, 2004.
- [74] M. V. Fischetti, “Master-equation Approach to the Study of Electronic Transport in Small Semiconductor Devices,” *Phys. Rev. B*, vol. 59, no. 7, p. 4901, 1999.
- [75] W. R. Frensley, “Boundary Conditions for Open Quantum Systems Driven far from Equilibrium,” *Rev. Mod. Phys.*, vol. 62, no. 3, p. 745, 1990.
- [76] U. Weiss, *Quantum Dissipative Systems*. World Scientific, 2008.
- [77] R. C. Iotti, E. Ciancio, and F. Rossi, “Quantum Transport Theory for Semiconductor Nanostructures: A Density-matrix Formulation,” *Phys. Rev. B*, vol. 72, no. 12, p. 125347, 2005.
- [78] R. C. Iotti and F. Rossi, “Microscopic Theory of Semiconductor-based Optoelectronic Devices,” *Rep. Prog. Phys.*, vol. 68, no. 11, p. 2533, 2005.
- [79] R. W. Hockney and J. W. Eastwood, *Computer Simulation using Particles*. Taylor & Francis, 1988.
- [80] M. Akarsu and O. Özbas, “Monte Carlo Simulation for Electron Dynamics in Semiconductor Devices,” *Math. and Comp. Appl.*, vol. 10, no. 1, p. 19, 2005.

- [81] C. Jacoboni and L. Reggiani, “The Monte Carlo Method for the Solution of Charge Transport in Semiconductors with Applications to Covalent Materials,” *Rev. Mod. Phys.*, vol. 55, no. 3, p. 645, 1983.
- [82] J. M. Ziman, *Principle of the Theory of Solids*. Cambridge University Press, 1972.
- [83] M. Hartig, S. Haacke, and B. Deveaud, “Femtosecond Luminescence Measurements of the Intersubband Scattering Rate in AlGaAs/GaAs Quantum Wells under Selective Excitation,” *Phys. Rev. B*, vol. 54, no. 20, p. R14269, 1996.
- [84] H. Fröhlich, “Theory of Electrical Breakdown in Ionic Crystal,” *Proceedings of the Royal Society*, vol. A160, p. 230, 1937.
- [85] K. Tomizawa, *Numerical Simulation of Submicron Semiconductor Devices*. Artech House, 1993.
- [86] G. Mahan, *Many-particle Physics*. Plenum, New York, 1990.
- [87] N. Bannov, V. Aristov, V. Mitin, and M. A. Stroschio, “Electron Relaxation Times due to the Deformation-potential Interaction of Electrons with Confined Acoustic Phonons in a Free-standing Quantum Well,” *Phys. Rev. B*, vol. 51, no. 15, p. 9930, 1995.
- [88] O. E. Raichev, “Phonon-assisted Γ -X Transfer in (001)-grown GaAs/AlAs Superlattices,” *Phys. Rev. B*, vol. 49, no. 8, p. 5448, 1994.
- [89] U. Penner, H. Rucker, and I. N. Yassievich, “Theory of Interface Roughness Scattering in Quantum Wells,” *Semicond. Sci. Technol.*, vol. 13, no. 7, p. 709, 1998.
- [90] H. Sakaki, T. Noda, K. Hirakawa, M. Tanaka, and T. Matsusue, “Interface Roughness Scattering in GaAs/AlAs Quantum Wells,” *Appl. Phys. Lett.*, vol. 51, no. 23, p. 1934, 1987.
- [91] S. Tsujino, A. Borak, E. Müller, M. Scheinert, C. V. Falub, H. Sigg, D. Grützmacher, M. Giovannini, and J. Faist, “Interface-roughness-induced Broadening of Intersubband Electroluminescence in p-SiGe and n-GaInAsAlInAs Quantum-cascade Structures,” *Appl. Phys. Lett.*, vol. 86, no. 6, p. 062113, 2005.
- [92] T. Unuma, M. Yoshita, T. Noda, H. Sakaki, and H. Akiyama, “Intersubband Absorption Linewidth in GaAs Quantum Wells due to Scattering by Interface Roughness, Phonons, Alloy Disorder, and Impurities,” *J. Appl. Phys.*, vol. 93, no. 3, p. 1586, 2003.
- [93] G. Bastard, *Wave Mechanics Applied to Semiconductor Heterostructures*. Le editions de Physique, Les Ulis, France, 1990.
- [94] C. Jacoboni, *Theory of Electron Transport in Semiconductors: A Pathway from Elementary Physics to Nonequilibrium Green Functions*. Springer Series in Solid-State Sciences, 2010.

BIBLIOGRAPHY

- [95] P. Harrison, “The Nature of the Electron Distribution Functions in Quantum Cascade Lasers,” *Appl. Phys. Lett.*, vol. 75, no. 18, p. 2800, 1999.
- [96] D. E. Aspnes, “GaAs Lower Conduction-band Minima: Ordering and Properties,” *Phys. Rev. B*, vol. 14, no. 12, p. 5331, 1976.
- [97] R. Tsu and L. Esaki, “Tunneling in a Finite Superlattice,” *Appl. Phys. Lett.*, vol. 22, no. 11, p. 562, 1973.
- [98] P. Panchadhyayee, R. Biswas, A. Khan, and P. K. Mahapatra, “Current Density in Generalized Fibonacci Superlattices under a Uniform Electric Field,” *J. Phys.: Condens. Matter*, vol. 20, no. 27, p. 275243, 2008.
- [99] J. Arriaga and V. R. Velasco, “Electronic Properties of GaAsAlAs Fibonacci Superlattices,” *J. Phys.: Condens. Matter*, vol. 9, no. 38, p. 8031, 1997.
- [100] M. H. Tyc and W. Salejda, “Negative Differential Resistance in Aperiodic Semiconductor Superlattices,” *Physica A*, vol. 303, no. 3-4, p. 493, 2002.
- [101] B. Mendez and F. DominguezAdame, “Numerical Study of Electron Tunneling through Heterostructures,” *Am. J. Phys.*, vol. 62, no. 2, p. 143, 1994.
- [102] B. Gelmont, V. Gorfinkel, and S. Luryi, “Theory of the Spectral Line Shape and Gain in Quantum Wells with Intersubband Transitions,” *Appl. Phys. Lett.*, vol. 68, no. 16, p. 2171, 1996.
- [103] W. S. C. Chang, *Principles of Lasers and Optics*. Cambridge University Press, 2002.
- [104] H. Willenberg, G. H. Doehler, and J. Faist, “Intersubband Gain in a Bloch Oscillator and Quantum Cascade Laser,” *Phys. Rev. B*, vol. 67, no. 8, p. 085315, 2003.
- [105] C. Y. L. Cheung, P. Rees, K. A. Shore, and I. Pierce, “Self-consistent Optical Gain and Threshold Current Calculations for Near Infrared Intersubband Semiconductor Lasers,” *J. Mod. Optics*, vol. 47, no. 11, p. 1857, 2000.
- [106] V. B. Gorfinkel, S. Luryi, and B. Gelmont, “Theory of Gain Spectra for Quantum Cascade Lasers and Temperature Dependence of their Characteristics at Low and Moderate Carrier Concentrations,” *IEEE J. Quant. Electron*, vol. 32, no. 11, p. 1995, 1996.
- [107] S. Barbieri, J. Alton, H. E. Beere, J. Fowler, E. H. Linfield, and D. A. Ritchie, “2.9THz Quantum Cascade Lasers Operating up to 70K in Continuous Wave,” *Appl. Phys. Lett.*, vol. 85, no. 10, p. 1674, 2004.
- [108] J. Kroell, J. Darmo, S. S. Dhillon, X. Marcadet, M. Calligaro, C. Sirtori, and K. Unterrainer, “Phase-resolved Measurements of Stimulated Emission in a Laser,” *Nature*, vol. 449, p. 698, 2007.

- [109] R. A. Coles, R. A. Abram, S. Brand, and M. G. Burt, "Dipole Matrix Elements and the Nature of Charge Oscillation under Coherent Interband Excitation in Quantum Wells," *Phys. Rev. B*, vol. 60, no. 19, p. 13306, 1999.
- [110] A. Benz, G. Fasching, A. M. Andrews, M. Martl, K. Unterrainer, T. Roch, W. Schrenk, S. Golka, and G. Strasser, "Influence of Doping on the Performance of Terahertz Quantum-cascade Lasers," *Appl. Phys. Lett.*, vol. 90, no. 10, p. 101107, 2007.
- [111] S. Adachi, "GaAs, AlAs, and $\text{Al}_x\text{Ga}_{1-x}\text{As}$: Material Parameters for use in Research and Device Applications," *J. Appl. Phys.*, vol. 58, no. 3, p. R1, 1985.
- [112] O. Madelung, *Semiconductors: Basic Data*. Springer-Verlag, Berlin, 1996.
- [113] G. Milovanovic and H. Kosina, "A Semiclassical Transport Model for Quantum Cascade Lasers based on the Pauli Master Equation," *Journal of Computational Electronics*, vol. 9, no. 3, p. 211, 2010.
- [114] P. K. Basu, "Effect of Interface Roughness on Excitonic Linewidth in a Quantum Well: Golden-rule and Self-consistent-Born-approximation Calculations," *Phys. Rev. B*, vol. 44, no. 16, p. 8798, 1991.
- [115] S. Rihani, H. Page, H. E. Beere, D. A. Ritchie, and M. Pepper, "Design and Simulation of a THz QCL based on Γ -X Depopulation Mechanism," *Physica E*, vol. 41, no. 7, p. 1240, 2009.
- [116] S. R. Schmidt, E. A. Zibik, A. Seilmeier, L. E. Vorobjev, A. E. Zhukov, and U. M. Ustinov, "Observation of Intersubband Real-space Transfer in GaAs/AlAs Quantum-well Structures due to Γ X Mixing," *Appl. Phys. Lett.*, vol. 78, no. 9, p. 1261, 2001.
- [117] J. J. Finley, R. J. Teissier, M. S. Skolnick, J. W. Cockburn, G. A. Roberts, R. Grey, G. Hill, M. A. Pate, and R. Planel, "Role of the X Minimum in Transport through AlAs Single-barrier Structures," *Phys. Rev. B*, vol. 58, no. 16, p. 10619, 1998.
- [118] G. Milovanovic, O. Baumgartner, and H. Kosina, "Design of a MIR QCL based on Intervalley Electron Transfer: A Monte Carlo Approach," in *Proceedings of the 10th International Conference on Mid-Infrared Optoelectronics: Materials and Devices*, p. 140, 2010.
- [119] M. Ohkubo, T. Ijichi, A. Iketani, and T. Kikuta, "Aluminium Free In-GaAs/GaAs/InGaAsP/InGaP GRINSCH SL-SQW Lasers at $0.98\ \mu\text{m}$," *Electron. Lett.*, vol. 28, no. 12, p. 1149, 1992.
- [120] S. L. Yellen, A. H. Shepard, C. M. Harding, J. A. Baumann, R. G. Waters, D. Z. Garbuzov, V. Pjataev, V. Kochergin, and P. S. Zory, "Dark-line-resistant, Aluminium-free Diode Laser at $0.8\ \mu\text{m}$," *IEEE Photonics Technol. Lett.*, vol. 4, no. 12, p. 1328, 1992.

- [121] J. Hu, X. G. Xu, J. A. H. Stotz, S. P. Watkins, A. E. Curzon, M. L. W. Thewalt, N. Matine, and C. R. Bolognesi, "Type II Photoluminescence and Conduction Band Offsets of GaAsSb/InGaAs and GaAsSb/InP Heterostructures grown by Metalorganic Vapor Phase Epitaxy," *Appl. Phys. Lett.*, vol. 73, no. 19, p. 2799, 1998.
- [122] M. Nobile, H. Detz, E. Mujagic, A. M. Andrews, P. Klang, W. Schrenk, and G. Strasser, "Midinfrared Intersubband Absorption in InGaAs/GaAsSb Multiple Quantum Wells," *Appl. Phys. Lett.*, vol. 95, no. 4, p. 041102, 2009.
- [123] P. Devlin, H. M. Heravi, and J. C. Woolley, "Electron Effective Mass Values in GaAs_xSb_{1-x} Alloys," *Can. J. Phys.*, vol. 59, no. 7, p. 939, 1981.
- [124] S. Adachi, *Properties of Semiconductor Alloys: Group-IV, III-V and II-VI Semiconductors*. Wiley, 2009.
- [125] S. Adachi, *Physical Properties of III-V Semiconductor Compounds: InP, InAs, GaAs, GaP, InGaAs, and InGaAsP*. Wiley-VCH, 2004.
- [126] S. Adachi, *Optical Constants of Crystalline and Amorphous Semiconductors: Numerical Data and Graphical Information*. Kluwer Academic Publishers, 1999.
- [127] S. Adachi, *GaAs and Related Materials: Bulk Semiconducting and Superlattice Properties*. World Scientific, 1994.
- [128] S. Adachi, *Properties of Group-IV, III-V and II-VI Semiconductors*. John Wiley & Sons, 2005.
- [129] I. Vurgaftman, J. R. Meyer, and L. R. Rahm-Mohan, "Band Parameters for III-V Compound Semiconductors and their Alloys," *J. Appl. Phys.*, vol. 89, no. 11, p. 5815, 2001.
- [130] O. Bonno, J. Thobel, and F. Dessenne, "Modeling of Electronelectron Scattering in Monte Carlo Simulation of Quantum Cascade Lasers," *J. Appl. Phys.*, vol. 97, no. 4, p. 043702, 2005.
- [131] M. G. Burt, "Direct Derivation of Effective-mass Equations for Microstructures with Atomically Abrupt Boundaries," *Phys. Rev. B*, vol. 50, no. 11, p. 7518, 1994.
- [132] P. Roblin, R. C. Potter, and A. Fathimulla, "Interface Roughness Scattering in AlAs/InGaAs Resonant Tunneling Diodes with an InAs Subwell," *J. Appl. Phys.*, vol. 79, no. 5, p. 2502, 1996.
- [133] J. Leo and A. H. MacDonald, "Disorder-assisted Tunneling through a Double-barrier Structure," *Phys. Rev. Lett.*, vol. 64, no. 8, p. 817, 1990.
- [134] P. E. Prange and T.-W. Nee, "Quantum Spectroscopy of the Low-field Oscillations in the Surface Impedance," *Phys. Rev.*, vol. 168, no. 3, p. 779, 1968.
- [135] C. Hamaguchi, *Basic Semiconductor Physics*. Springer-Verlag, Berlin, 2001.

Own Publications

- [1] G. Milovanovic, O. Baumgartner, and H. Kosina. Design of a MIR QCL based on Intervalley Electron Transfer: A Monte Carlo Approach. in *Proceedings of the 10th International Conference on Simulation on Mid-Infrared Optoelectronics: Materials and Devices*, pp. 140–141, 2010.
- [2] G. Milovanovic, and H. Kosina. A Semiclassical Transport Model for Quantum Cascade Lasers based on the Pauli Master Equation. *J. Comp. Electronics*, 9(3-4):211–217, 2010.
- [3] G. Milovanovic, O. Baumgartner, and H. Kosina. On Open Boundary Conditions for Quantum Cascade Structures. *Optical and Quantum Electronics*, 41(11-13):921–932, 2009.
- [4] G. Milovanovic, O. Baumgartner, and H. Kosina. Simulation of Quantum Cascade Lasers using Robin Boundary Conditions. in *Proceedings of the 9th International Conference on Numerical Simulation of Optoelectronic Devices*, pp. 7–8, 2009.
- [5] G. Milovanovic, and H. Kosina. Nonparabolicity Effects in Quantum Cascade Lasers. in *Proceedings of the 13th International Workshop on Computational Electronics*, pp. 189–192, 2009.
- [6] G. Milovanovic, and H. Kosina. Valence Band Deformation Potentials in Semiconductors. in *Abstracts of the 4th International SiGe Technology and Device Meeting*, pp. 215–216, 2008.

Curriculum Vitae

August 19th, 1981

Born in Tulln, Austria.

June 1999

High school graduation (*Matura*) at the Realgymnasium KREMS, specializing in Natural Sciences.

October 1999

Enrolled in Physics at Vienna University of Technology, Austria.

November 2005

Received degree of *Diplom-Ingenieur* (M.Sc.) in Physics, specializing in Theoretical Physics from the Vienna University of Technology (with distinction).

April 2007

Entered doctoral program at the Institute for Microelectronics, Vienna University of Technology, under the supervision of Prof. *Hans Kosina*.

January 24th, 2008

Birth of daughter Marie Lilia.